Drug-loaded Gold Plasmonic Nanoparticles for *In Vivo* Therapy of Multidrug Resistance in Cancer and Rheumatoid Arthritis

Hyung Joon Kim

The Graduate School

Yonsei University

Graduate Program for Nanomedical Science

Drug-loaded Gold Plasmonic Nanoparticles for *In Vivo* Therapy of Multidrug Resistance in Cancer and Rheumatoid Arthritis

A Dissertation
Submitted to the Graduate Program for Nanomedical Science
and the Graduate School of Yonsei University
in partial fulfillment of the
requirements for the degree of
Doctor of philosophy of Nanomedical Science

Hyung Joon Kim

August 2015

This certifies that the dissertation of
Hyung Joon Kim is approved.

_____
Thesis Advisor: Kyung-Hwa Yoo

_____
Thesis Committee Member : Dug Young Kim

_____
Thesis Committee Member : Yong-Beom Park

_____
Thesis Committee Member : Jeon-Soo Shin

_____
Thesis Committee Member : In-Hong Choi

The Graduate School
Yonsei University
August 2015

감사의 글

많이 부족한 저를 학문과 연구에 몰두할 수 있도록 지도해 주시고, 학문과 연구뿐 만 아니라 인생 지도도 함께 해주신 유경화 교수님께 진심으로 감사드립니다. 또한, 논문 심사를 해주신 의과대학 류마티스 내과의 박용범 교수님, 의과대학 미생물학교실의 신전수 교수님, 최인홍 교수님, 그리고 물리학과의 김덕영 교수님께 깊은 감사를 드립니다.

유경화 교수님 연구실에서 석사과정을 마치고 박사과정에 들어왔을 때, 약물 전달 시스템과 나노입자 연구에 관한 많은 노하우를 알려주시고 지금의 논문을 쓸 수 있게 해 주신 이선미 박사님과 박사졸업 후 의학전문대학원에 다니시는 미래의 의사선생님 희열형에게 진심으로 감사의 마음을 전합니다. 또한, 지금은 다른 연구실에 계시지만, 항상 저를 챙겨주시는 최향희 박사님과 카본나노튜브 연구의 기본을 마련해 주신 황성식 박사님께도 감사 말씀 드립니다. 그리고, 현재 연구실 졸업 후 산-학-연 각지에서 대한민국 발전을 위해 열심히 일하고 계시는 자랑스런 영욱형, 제승형, 성인형, 정도형, 민수형, 봉근형, 지헌형, 희열형, 리미누나, 승환형, 재학형, 형섭형, 운진형, 창섭형, 승호형 선배님과 정기, 준호, 여안이 모두 학위 기간 동안 같이 연구실 생활을 할 수 있어서 영광이었습니다.

물리학의 내공이 엄청나시고 저와 함께 석,박사 과정을 보내고 같이 졸업하는 마음이 따뜻하신 주형형, 아침형 인간 생활을 하루도 거르지 않고 생활하시면서 연구하시는 대단한 민지누나, 제 유일한 대학원 동기이자 옆자리인 열심히 연구하는 날애, 주변 사람을 기분 좋게 해주고 앞으로 연구실을 이끌어 나갈 SK hynix 섬균이, 옷과 신발을 좋아하는 연구실 멋쟁이 상정이, 손재주가 좋고 다양한 실험 아이디어를 제안하는 명욱이, 처음 연구실에 온 날부터 납땜을 하고 열심히 실험한 봉준이, 시험 보면 항상 top에 있는 연대 물리학과 수석 졸업인 충만이, 맘 편하게 대화할 수 있는 착한 성진이, 앞으로 최소 7년 동안 연구

실 생활을 하면서 훌륭한 연구를 할 미래 전문연구요원들인 성현이와 준호, 물리학과 생물을 복수전공하면서 연구도 같이 하는 대단한 학부생 서원이, 사무원 예지 모두 감사의 마음을 전합니다. 또한 같이 연구를 진행하면서 많은 도움을 주신 의과대학 류마티스 내과의 박규형 선생님, 문진희 선생님, 임지희 선생님, 신용대 선생님과 미생물학 교실의 김솔 박사님, 김숙영 선생님, 그리고 서진원 선생님께도 감사 말씀 드립니다.

큰 어려움과 문제없이 대학원 생활을 할 수 있게 도와주신 하나님께 감사드리고, 변함없이 무한한 사랑으로 저를 돌봐주신 부모님께 감사 드립니다. 제 인생의 롤모델이신 아버지와 항상 저를 걱정해 주시고 응원 해주신 어머니, 정말 감사드려요! 그리고, 선택한 길은 후회 없이 가라고 큰 조언을 준 미국에서 조카 준우와 행복한 시간을 보내고 있는 누나에게 감사의 마음을 전합니다. 또한, 오랜 세월 동안 함께한 제 친구들에게도 고마움을 전합니다.

7년이라는 기간 동안 정말 많은 것을 배웠고, 앞으로 연구하는데 있어서 큰 기반이 될 것이라고 확신합니다. 비단 연구뿐 만 아니라 앞으로 살아가면서 어떤 어려움이 있어도 지혜롭게 극복해 나갈 수 있는 능력을 배웠다고 생각합니다. 많은 도움을 주셨던 사람들을 항상 잊지 않고, 앞으로 연구 생활을 하는데 있어 최선을 다하도록 하겠습니다. 끝으로, 하나님과 가족들, 곧 저의 아내가 될 영주에게 다시 한번 감사하고 사랑한다는 말을 전합니다.

2015년 6월

김형준 드림

CONTENTS

Chapter 2.

In vivo chemo-photothermal therapy and imaging of multidrug resistance in cancer.....30

Chapter 3.

***In vivo* chemo-photothermal therapy and imaging of rheumatoid arthritis.....71**

Chapter 4.

Multi walled carbon nanotubes electrodes : application in discrimination of lipid region in *ex vivo* atherosclerosis using capacitance imaging.....129

LIST OF FIGURES

Figure 8. Various kinds of Au plasmonic nanoparticles used for cancer photothermal therapy and optical imaging. (a) Thermal and NIR laser-triggered release of ssDNA from AuNSs. a) Schematic diagram of dsDNA-modified AuNSs. b) Scanning electron microscope (SEM) image of the AuNSs. c) Extinction spectra of i) gold nanorods (AuNRs) and ii) AuNSs. (b) Docetaxel (DOC) as an anti-cancer drug and transferring (Tf) as a targeting moiety were incorporated into the SN (silica nanorattle)@AuNSs for the cancer thermo-chemotherapy and imaging. a) Schematic diagram of AuNSs with a core of silica nanorattle and with shells modified targeting ligand. b) Photo and infrared thermal image of tumor-bearing nude mouse after NIR light irradiation. c) Extinction spectrum of poly(ethylene glycol) (PEG)-modified gold nanoshells on silica nanorattles (pGSNs) and pGSNs-Tf, the inset is the TEM image of pGSNs-Tf. d) *In vivo* antitumor efficacy using pGSNs-Tf with NIR irradiation. (c) Au@SiO2 as a multifunctional theragnostic platform. a) The photothermal effect on lysosomal membrane integrity of A549 cells. b) Intracellular localization image of DOX (red) and Au@SiO2 (blue) in A549 cells stained with Lyso-Tracker (green) using two-photon confocal microscope. c) Controlled DOX release within A549 cells after NIR irradiation (live and dead cells were stained). (d) Targeted NIR-responsive AuNRs which are self-assembled with DNA for cancer thermo-chemotherapy. a) The schematic diagram of DNA assembled AuNRs. b) Antitumor effects of tumor-bearing mouse after different treatments. (e) HAuNS-loaded microspheres (HAuNS-MSs) for phtothermal-chemotherapy. a) Schematic diagram of PTX-HAuNS-MSs. b) Antitumor effects of U87 human gliomas grown in nude mice after different

LIST OF TABLES

ABSTRACT

Drug-loaded Gold Plasmonic Nanoparticles for *In Vivo* Therapy of Multidrug Resistance in Cancer and Rheumatoid Arthritis

Hyung Joon Kim

Graduate Program for Nanomedical Science

The Graduate school

Yonsei university

Gold (Au) plasmonic nanoparticles (NPs) containing doxorubicin (DOX) for the treatment of multidrug resistance (MDR) in cancer were developed. To investigate the possibility of treating multidrug-resistant tumors with targeted chemo-photothermal treatment, *in vitro* and *in vivo* studies were conducted using a doxorubicin (DOX)-resistant DLD-1 cell line (DLD-1/DOX) and nude mice with

human xenograft tumors, respectively. The chemo-photothermal treatment consisted of DOX-loaded-poly(lactic-*co*-glycolic acid, PLGA)-Au half-shell nanoparticles with targeting moieties of anti-death receptor-4 monoclonal antibody conjugated to the Au surface. The cells or xenografted tumors treated with nanoparticles were exposed to near infrared light for 10 min, which caused an increase in temperature to 45 °C. Chemo-photothermal treatment resulted in a large reduction in the rate of tumor xenograft growth on DLD-1/DOX tumor-bearing mice with a much smaller dose of DOX than conventional DOX chemotherapy. These results demonstrate that targeted chemo-photothermal treatment can provide high therapeutic efficacy and low toxicity in the treatment of multidrug-resistant tumors.

RGD-attached gold (Au) plasmonic nanoparticles (NPs) containing methotrexate (MTX) for the treatment of rheumatoid arthritis (RA) were also developed. The MTX is the most widely used disease modifying anti-rheumatic drug (DMARD) for the treatment of RA, and RGD peptide (arginine-glycine-aspartic acid) is a targeting moiety for inflammation. Upon near-infrared (NIR) irradiation, heat is locally generated due to Au half shells, and the drug release rate is enhanced, delivering heat and drug to the inflamed joints simultaneously. RA is a chronic inflammatory disease characterized by synovial inflammation in multiple joints within the penetration depth of NIR light. When combined with NIR irradiation, these nanoparticles containing a much smaller dosage of MTX (1/930 of MTX solution) showed greater therapeutic effects than that of a conventional

treatment with MTX solution in collagen-induced arthritic (CIA) mice. This novel drug delivery system is a good way to maximize therapeutic efficacy and minimize dosage-related MTX side effects in the treatment of RA. Furthermore, these multifunctional nanoparticles could be applied to other DMARDs for RA or other inflammatory diseases.

Similar results were obtained using MTX-loaded PLGA gold (Au)/iron (Fe)/gold (Au) half-shell nanoparticles conjugated with RGD, which can be applied for magnetic targeted chemo-photothermal treatment, and *in vivo* multimodal imaging of RA. The Fe half-shell layer embedded between the Au half-shell layers enables *in vivo* T_2-magnetic resonance (MR) imaging in addition to NIR absorbance imaging. Furthermore, the delivery of the nanoparticles to the inflammation region in CIA mice, and their retention can be enhanced under external magnetic field. When combined with consecutive NIR irradiation and external magnetic field application, these nanoparticles provide enhanced therapeutic effects with an MTX dosages of only 0.05% dosage compared to free MTX therapy for the treatment of RA.

Keywords: Drug-loaded Au plasmonic nanoparticles, Drug-loaded Au/Fe/Au plasmonic nanoparticles, chemo-photothermal treatment, photothermally controlled drug delivery, multidrug resistance in cancer, rheumatoid arthritis

Chapter 1.

Introduction

1.1. Overview of multifunctional nanoparticles

1.1.1. Multifunctional nanoparticles

Nanoparticles are particles with 1 ~ 100 nm in size. These nanoparticles have shown size dependent physical and chemical properties such as optical, catalytic, magnetic, electrochemical, and thermodynamic, which are different from the same composition of bulk materials. A variety of nanoparticles made of different materials such as gold nanoparticles, magnetic nanoparticles, quantum dots, upconversion nanoparticles, carbon nanotubes, and polymeric particles have been fabricated and used in many scientific fields including physics, chemistry, material sciences, and medicine [1]. Especially, the application of nanoparticles to medicine, known as nanomedicine, uses the precisely engineered nanoparticles to develop novel therapeutic and diagnostic of several diseases. Exploring these unique

properties of nanoparticles can overcome some hurdles found in conventional therapeutic agents and diagnostic tools.

• Physical properties and applications of various nanoparticles

1) Gold nanoparticles

The most common type of gold nanoparticles is gold nanospheres, and their unique optical properties is localized surface plasmon resonance (LSPR), in which conduction band electrons in gold nanospheres oscillate coherently with incident light at specific frequency [2]. Part of the absorbed energy is emitted in the form of scattered light, which then application the optical imaging and the rest of the energy is converted into heat. Gold nanospheres cannot apply to *in vivo* applications, because gold nanospheres have absorption peak at around 520 nm wavelength. For *in vivo* applications, the absorption peak should match within the biological optical window of human tissues (650 ~ 900 nm), in which minimal optical absorption by intrinsic chromophores, such as hemoglobin (< 650 nm) and water (> 900 nm), resulting in maximal penetration of light into biological tissues [3]. The absorption spectrum of gold nanoparticles can be tuned through geometry modification. For example, gold nanorods, LSPR occurs in two directions; along the short- and the long-axes [4]. Other gold nanostructures such as gold nanoshells and gold nanocages have tunable surface plasmon resonance peak with changing their sizes and thickness of walls (Figure 1a). Aggregated gold nanospheres also

exhibit NIR absorption due to the coupled plasmon resonance. This property can be applied to photothermal therapy in various diseases.

Scattered light at LSPR frequency of gold nanoparticles uses to optical imaging. In addition, gold nanoparticles enhance local electromagnetic fields due to the LSPR. Therefore, the signals of SERS (surface-enhanced Raman scattering) or fluorophore reporters bound to a gold surface can be dramatically increased [5]. In *in vivo* applications, gold nanoparticles are good contrast agents for optical coherence tomography (OCT), computed tomography (CT), photoacoustic (PA) imaging, and near-infrared (NIR) optical imaging as well as photothermal therapy agents at the NIR region [6].

2) Magnetic nanoparticles

Magnetic nanoparticles are mainly consisted of iron oxides (magnetite or maghemite). When the size of magnetic particles is smaller than the magnetic domain wall width (usually less than 100 nm), the particles will contain only a single magnetic domain with the magnetic moment from all unpaired electrons coupled in one direction [7]. Thermal fluctuation leads to flip of the coupled magnetic moment among several crystal axes of the nanoparticle. The flipping rate increases until no net magnetization can be observed as the particle size decreases. These magnetic nanoparticles which have limited size are called superparamagnetic nanoparticles. Usually, the size of superparamagnetic iron oxide nanoparticles is between 20 and 25 nm at room temperature [7]. Upon an external

magnetic field is applied, the magnetic moment of the superparamagnetic nanoparticles will align along the magnetic field and reach saturation at relatively low magnetic field strength. In biomedical application, magnetite and maghemite nanoparticles are the most well known magnetic nanoparticles due to their excellent biocompatibility. Nanoparticles of materials that have higher saturation magnetization have also been fabricated (Figure 1b).

Superparamagnetic iron oxide nanoparticles (SPIOs) were used as a T_1 or T_2 contrast agents for MRI, and exhibited clinical tumor detection application [8]. Magnetic nanoparticles also show hyperthermia induction and magnetic targeting. Magnetic nanoparticles can generate heat under an oscillating magnetic field (100 kHz to 1 MHz), which enables the hyperthermia for cancer therapy [9]. Magnetic targeting has been used in *in vitro* such as cell separation, gene transfection as well as controlled delivery of therapeutic agents in *in vivo* system [10].

3) Quantum dots

Quantum dots (QDs) is fluorescence-emitting semiconductor nanoparticles, which usually used in optical imaging. Most QDs are consisted of binary alloys such as CdSe or InP semiconductor materials. Owing to quantum confinement of valence electrons at nanometer scales, QDs have shown fluorescence emission at various size and composition (Figure 1c) [11]. As shown in Figure 1c, the emission peak is red-shifts as the size of QDs increases. QDs have a narrow emission peak and an absorption peak from UV to visible wavelengths range as compared to

organic fluorophores. So, multicolor fluorescence imaging can be achieved in *in vitro* and *in vivo* systems and the toxicity of QDs was also investigated [12].

4) Upconversion nanoparticles

An upconversion nanoparticles (~ 10 nm) has been studied after advances in rare-earth nanoparticle synthesis [13]. The upconversion nanoparticles have unique optical properties because they can absorb infrared radiation and emit photons at visible region. This upconversion process is achieved through continuous excitation of valence electrons of lanthanide ions by photon absorption or energy transfer from nearby excited lanthanide ions [14]. These upconversion nanoparticles are composed of a host material doped with lanthanide ions which act as sensitizers (Yb^{3+}) and activators (Er^{3+}, Tm^{3+}, and Ho^{3+}). Similar to QDs, upconversion nanoparticles have an narrow emission spectrum that can be tuned by changing host materials, doping density, and sensitizer ions (Figure 1d) [15].

Upconversion nanoparticles are excited at 980 nm using a InGaAs diode laser system and the low-power NIR excitation makes upconversion nanoparticles useful for *in vivo* optical imaging. Coupling upconversion nanoparticles with photosensitizers showed the ability to photodynamic therapy of cancer [16].

5) Other inorganic nanoparticles

There are various inorganic nanoparticles, including silica nanoparticles [17], calcium phosphate nanoparticles [18], hafnium oxide nanoparticles [19], and carbon nanotubes. Silica and calcium phosphate nanoparticles do not exhibit unique quantum mechanical properties. However, these nanoparticles have biocompatibility, convenient size tuning, various conjugation chemistry, and versatile cargo loading strategy as well as used for carriers of drug molecules, genes, and imaging contrast agents [20-22]. Silica nanoparticles with organic dyes and radioactive iodide, known as Cornell dots or C dots, have also been approved for clinical trials.

Carbon nanotubes are formed from coaxial graphite sheets (< 100 nm) rolled up into cylinders and have two types; single- or multi-walled nanotubes. They have excellent strength and electrical properties, and can be water soluble by surface modification. Single-walled carbon natubes can be used as photothermal therapy agent, optical imaging agents, and drug carriers [23].

6) Polymeric particles

Polymeric particles have several advantages, such as (a) encapsulation of various drugs and release them over prolonged periods or shot periods, (b) modification of surfaces with targeting ligands or antibody, and (c) excellent stability in both *in vitro* and *in vivo* system. Biodegradable polymers such as

poly(glycolic acid), poly(lactic acid) (PLA), and their copolymers have been used for various drug delivery applications [24]. Copolymers of hydrophobic polymers and hydrophilic polymers such as poly(ethylene glycol) (PEG), PEO, and poly(propylene oxide) (PPO) are explored to synthesize self-assembled therapeutic carriers [25]. Responsive polymers, which respond to an external stimulus such as pH, temperature, and electromagnetic radiation are also studied for drug delivery [26-27].

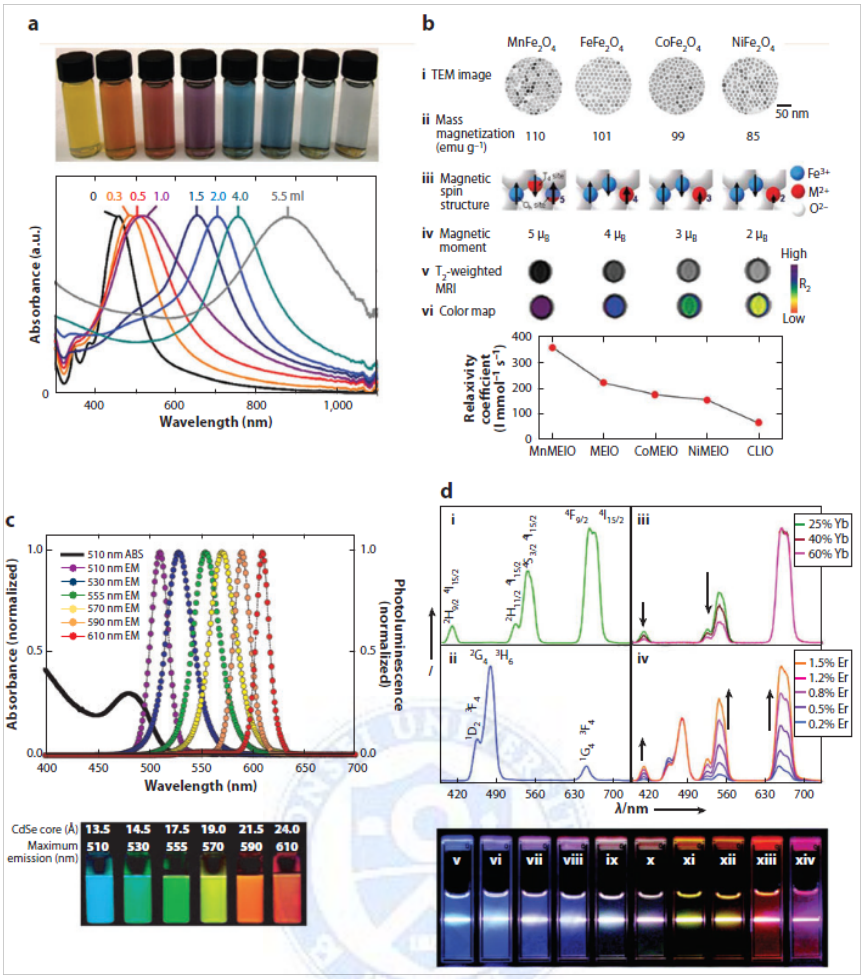

Figure 1. Physical properties of various nanoparticles [28]. (a) Gold nanocage exhibits tunable surface plasmon resonance peak. (b) Magnetic nanoparticles fabricated by doping iron oxide with various magnetic ions. (c) Quantum dots exhibits size-tunable fluorescence emission. (d) Emission spectra of upconversion nanoparticles with different sensitizer and activator ions. Abbreviations: CLIO, cross-linked iron oxide; MEIO, magnetism-engineered iron oxide; MRI, magnetic resonance imaging; TEM, transmission electron microscopy; ABS, absorption spectrum; EM, emission.

Multifunctional nanoparticles (MFNPs) composed of inorganic materials such as metal, semiconductor, silica and rare earth minerals shows unique optical, electric, magnetic, and plasmonic properties due to the quantum mechanical effects originated from nanometer scale [29]. Inorganic nanoparticles have multifunction in nature. For example, gold nanoparticles used as a contrast agents for optical imaging, photoacoustic (PA) imaging, and computed tomography (CT) [30]. Also, gold nanoshells and nanocages can be applied for photothermal therapy upon near-infrared (NIR) laser irradiation as well as NIR optical imaging [31-32]. MFNPs can achieve combined effects which cannot obtain in mono functional nanoparticles; for example, a quantum dot can show high fluorescence but it cannot show magnetic property [33].

The schemes of MFNPs are combining two or more imaging functions for multimodal imaging, integrating drug delivery with imaging for image-guided drug delivery, and combining drug delivery with thermal treatments for synergistic effects [28].

For realization of combined effects of MFNPs, it is important to explore surface chemistry and surface modification techniques. Small molecules, such as therapeutic agents, dyes, antibody, and targeting ligand can be bound to the nanoparticles surface via well-established surface chemistry. Liposome or micelle encapsulation and mesoporous silica coating, and layer-by-layer assembly of biopolymers methods can apply to decorate nanoparticles, results in multifunctions. Therefore, various MFNPs can be fabricated by combining nanoparticles and small molecules (Figure 2).

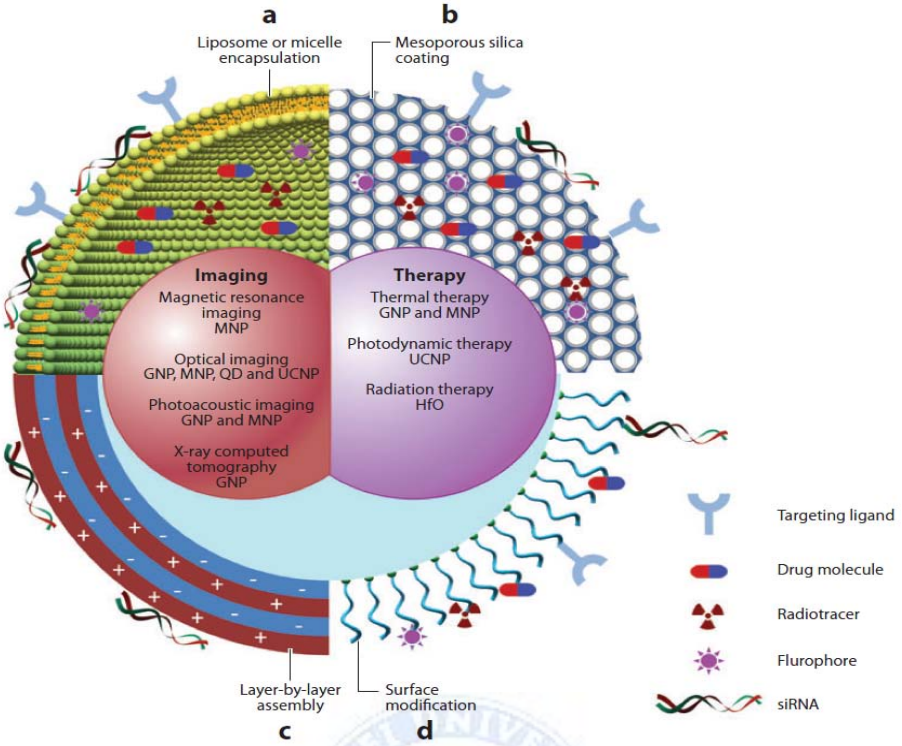

Figure 2. Schematic diagram of multifunctional nanoparticles [28]. Four typical coatings explored for nanoparticles are (a) liposome or micelle encapsulation, (b) mesoporous silica coating, (c) layer-bylayer assembly, and (d) surface modification. Abbreviations: GNP, gold nanoparticles; HfO, hafnium oxide nanoparticles; MNP, magnetic nanoparticles; QD, quantum dot; UCNP, upconversion nanoparticles.

The synthesis of most inorganic MFNPs involves two steps; nucleation and crystal growth by deposition of atoms on the crystal surface. Iron oxide nanoparticles, QDs, and upconversion nanoparticles can be synthesized using coprecipitation or thermal decomposition of precursor compounds with capping molecules and solvents [13, 34-36]. The common synthetic methods for integration of different nanoparticles or the combination of nanoparticles with small molecules are shown in Table 1.

Table 1. Synthesis methods for MFNPs [28].

Synthesis method	Nanoparticles
Nanoparticle-nanoparticle combination	
■ Seed-mediated growth	$NaGdF_4$@$NaGdF_4$:Yb^{3+}/Er^{3+}, gold shell@SPIO
■ Metal coordination/chelation	Gold shell/silica (gold seeds are first absorbed onto silica surface through gold-amine coordination), gold nanosphere@SPIO
■ Biological/chemical bond	Gold nanosphere and SPIO linked via biotin-streptavidin interaction. SPIO linked to silica via chemical bonds
■ Hydrophobic/electric interaction	QD and SPIO in phospholipid-PEG, QD with negative charges in PEG-PEI
■ Physical entrapment	Various nanoparticles entrapped in mesoporous silica or liposomes
Nanoparticle–small molecule combination	
■ Chemical conjugation	TRITC, Cy5, and ^{124}I conjugated to C dots, Cy5.5 and ^{64}Cu-DOTA conjugated to SPIO
■ Electrostatic interaction	Plasmid DNA complexed with silica nanoparticles or mesoporous silica
■ Hydrophobic interaction	Doxorubicin in phospholipid-PEG micelle, cholestane and phenanthrene in mesoporous silica

Abbreviations: PEG, poly(ethylene glycol); PEI, poly(ethyl enimine); QD, quantum dot; SPIO, superparamagnetic iron oxide nanoparticle; TRITC, tetramethylrhodamine isothiocyanate.

1.1.2. Applications in nanomedicine

An important application of multifunctional nanoparticles (MFNPs) is medicine. MFNPs have various functions in medicine applications such as (a) contrast agents for multimodality imaging, (b) image-guided drug delivery, (c) magnetic drug targeting, and (d) drug delivery in combination with thermal therapy.

(a) Contrast agents for multimodality imaging

Usually, imaging technique is effective only for examining one specific disease due to the limitations in resolution, specificity, sensitivity, time and cost. However, multimodality imaging which merging various imaging techniques into one platform have ability to overcome these hurdles and can provide better disease management. The nanoparticles designed for MRI, NIR optical imaging, and PA imaging can be easily conjugated with small-molecule imaging moieties, including SERS reporters, MRI contrast agents (Gd^{3+} or Mn^{2+}), fluorophores and radiotracers. These multimodality imaging nanoprobes can provide local as well as high-resolution images than that of just one imaging probe. For example, gold nanospheres were functionalized with both a Raman molecular tag, trans-1,2-bis(4-pyridyl)-ethylene, and an MRI T_1 agent, DOTA-Gd^{3+}. This fabricated multimodality imaging nanoprobes enable MRI, PA imaging, and Raman imaging (Figure 3) [37].

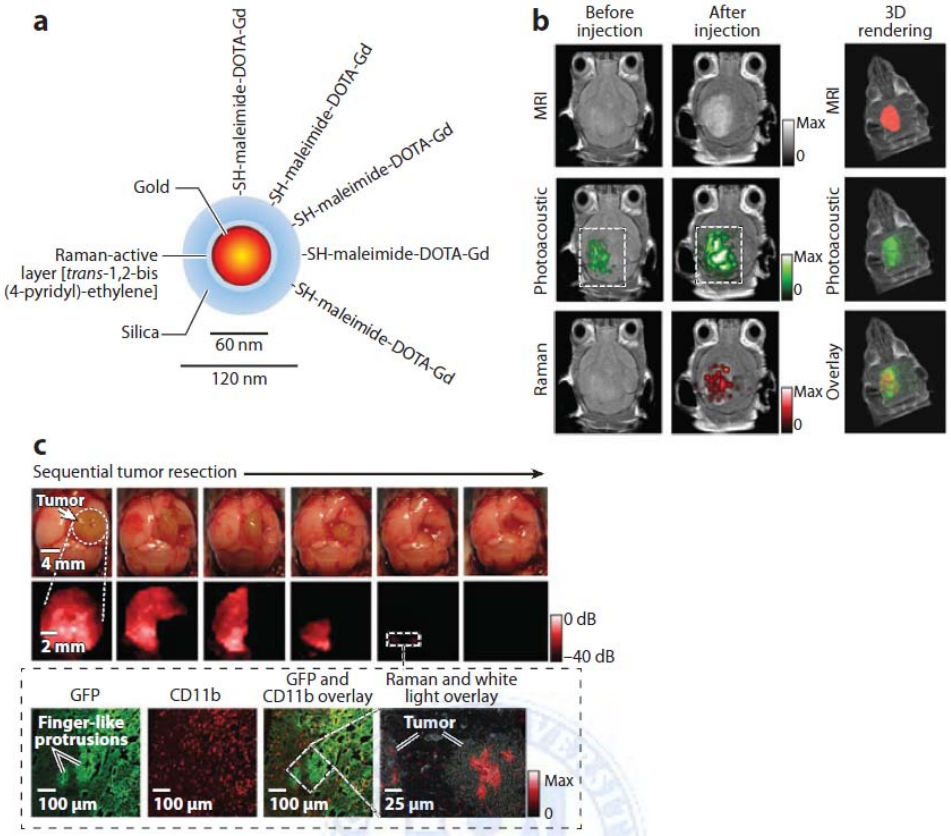

Figure 3. MFNPs for multimodality imaging [37]. (a) Schematic diagram of trimodality nanoparticle for brain tumor imaging. (b) Trimodality detection of brain tumors in living mice. (c) Raman-guided intraoperative surgery. Abbreviations: CD11b, cluster of differentiation molecule 11b; GFP, green fluorescent protein.

(b) Image-guided drug delivery

It is important to deliver drug into the entire tumor at concentrations above a therapeutic threshold to success the cancer chemotherapy. A standard

chemotherapy would be effective only during a narrow therapeutic window in some patients. However, image-guided drug delivery simultaneously enables guiding disease interventions and effective drug delivery to the disease site. For example, siRNA conjugated to dextran-coated SPIOs as well as attachment of NIR dye, Cy 5.5 have been used to image *in vivo* siRNA delivery (Figure 4) [38]. The accumulation of siRNA at the tumor region was visualized with both *in vivo* NIR optical imaging and MRI imaging.

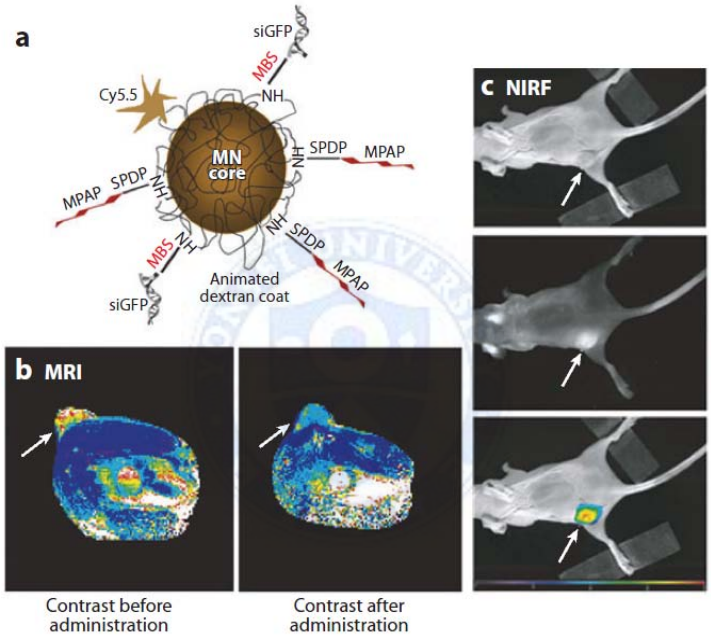

Figure 4. Image-guided siRNA delivery [38]. (a) Schematic diagram of the siRNA carrier with MRI/NIR modalities (MN-NIRF-siRNA). MN (magnetic nanoparticles) core and Cy5.5 can be detected with MRI and NIRF imaging, respectively. (b) *In vivo* MRI of mice bearing subcutaneous LS174T human colorectal adenocarcinoma (arrows). (c) NIRF imaging of the mouse after injection of MN-NIRF-siRNA (top: white light, middle: NIRF, bottom: color-coded overlay).

(c) Magnetic drug targeting

The ability to actively deliver drugs in *in vivo* system has been achieved by magnetic targeting property of MFNPs. Therapeutic agents attached to magnetic nanoparticles can be accumulated to local disease region under magnetic guidance after proper design of the externally applied magnetic field [39-40]. In the 1978, magnetic targeting in *in vivo* system was first demonstrated using magnetic albumin microspheres (clusters of albumins with 10 ~ 20 nm in diameter of magnetic particles) [41]. Selective targeting of magnetic albumin microspheres containing doxorubicin to Yoshida sarcoma-bearing rat were also demonstrated in 1983 [42].

Recent advances in nanotechnology have accelerated the development of magnetic nanoparticles. Magnetic nanoparticles have advantages than microspheres such as deep tumor penetration, better biocompatibility, and optimum biodistribution. Several types of magnetic nanoparticles, including micelles-, liposomes-, and mesoporous silica-coated SPIOs, have been shown magnetic targeting of drugs in *in vivo* system [43]. Magnetic targeting could be explored using an implanted magnetic stent after injection of paclitaxel-loaded magnetic nanoparticles [44]. Electrostatic interaction of positively charged magnetic lipid nanoparticle with negatively charged siRNA could also be applied to magnetically guided gene therapy [10].

In another study, magnetically targeted SPIOs/lentiviral vectors were used to deliver enhanced green fluorescent protein (eGFP) plasmid to mouse aorta *ex vivo*

and SPIOs/lentiviral vectors-trasnsduced endothelial cells could be also located in injured carotid artery by external magnetic field (Figure 5) [45].

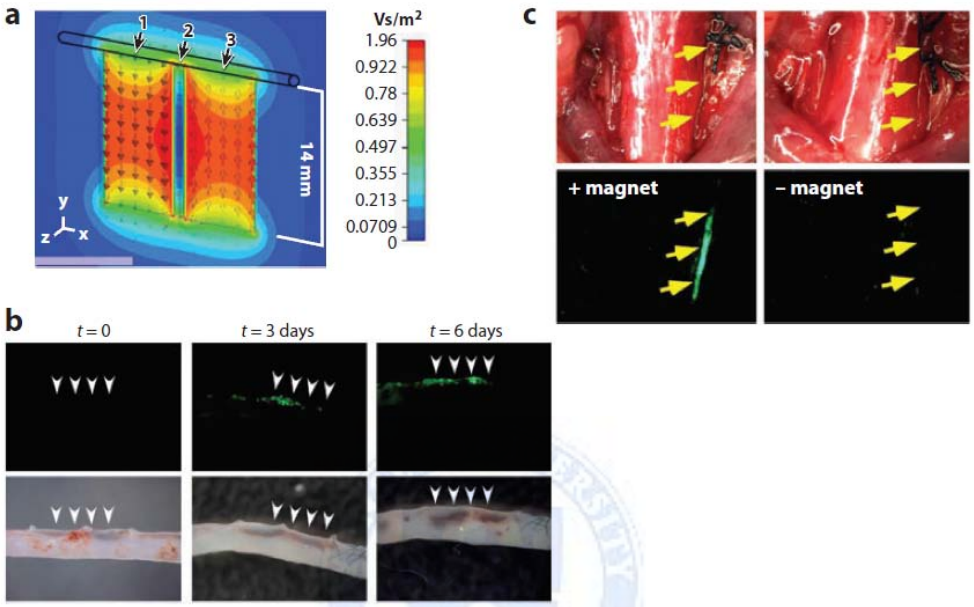

Figure 5. Magnetic targeting of lentiviral vectors and positioning of transduced cells under external magnetic field [45]. (a) The magnetic flux density of magnets placed beside a vessel. (b) Magnetic targeting of SPIOs/lentiviral vectors to aorta during *ex vivo* perfusion. (c) *In vivo* location of SPIOs/lentiviral vectors – transduced HUVECs (human umbilical vein endothelial cells) at injured carotid artery by external magnetic field.

(d) Drug delivery in combination with thermal therapy

Hyperthermia (thermotherapy) has been widely used to cancer therapy and local heat generation can enhance the extravasation of drug-loaded nanoparticles from tumor vessels [46]. Conventional chemotherapy can be combined with thermal therapy, leading to synergistic effect than the sum of independent therapy. Therefore, drug-loaded gold nanoparticles or magnetic nanoparticles provide effective combined thermal and chemotherapy of cancer.

A controlled drug release can be enabled by combination therapy. High concentration of drug in target region can be achieved by local heat-induced burst drug release. For example, heat generation under oscillating AC (alternating current) magnetic field would destroy the magnetite shell of drug-loaded magnetite shell/silica cores nanoparticles, resulting in release of drug stored in the silica matrix [47]. In another study, mesoporous silica sealed with thermosensitive nanovalves which encapsulated in zinc-doped iron oxide nanocrystals and doxorubicin (DOX) was fabricated. Heating of zinc-doped iron oxide nanocrystals after oscillating AC magnetic field led to rapid DOX release (Figure 6) [48].

Gene delivery has also been realized by local heat generation. Heat is applied to dextran-coated SPIOs conjugated with double-strand DNA (dsDNA). Increasing temperature induces releasing single-strand DNA oligo from dsDNA [49]. Similarly, endolysosomal escape of siRNA from a hollow gold nanoshell conjugated with thiolated siRNA after NIR laser irradiation could also studied.

Further study shows that p65 siRNA photothermal transfection and irinotecan treatment exhibit tumor suppression in *in vivo* [50].

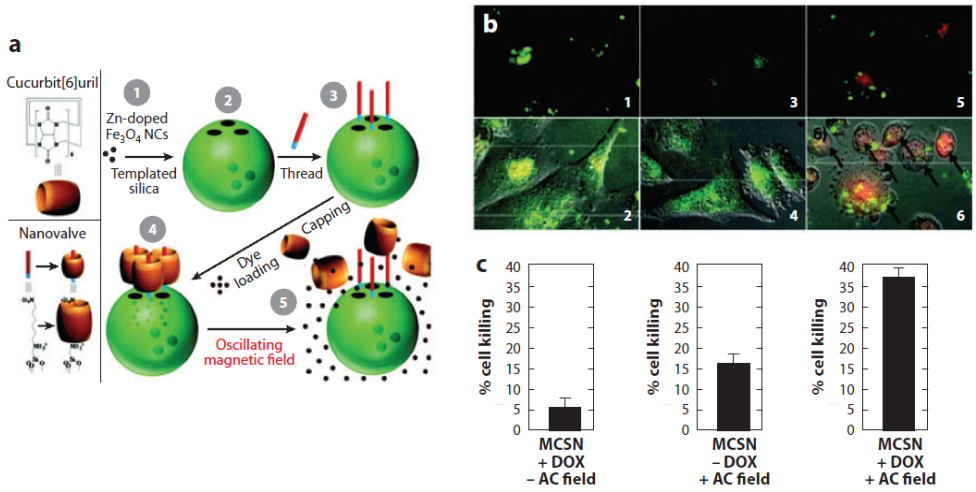

Figure 6. Combined thermal and chemotherapy system [48].

(a) Schematic diagram of magnetic-core silica nanoparticles (MCSN) for magnetically triggered drug release system. MCSN are synthesized by coating zinc-doped iron oxide nanocrystals (1) with mesoporous silica (2). The base of the molecular machine is inserted to the template silica (3). The drug (DOX) is then loaded into the template silica and capped with thermosensitive nanovalves (4) to complete the magnetically triggered drug release system. DOX release can be realized by heat generation under oscillating AC magnetic field (5). (b) Fluorescence microscope images (1, 3, and 5) and differential interference contrast (DIC) overlaid images (2, 4, and 6). Images 5 and 6 show DOX release after a 5 min oscillating AC magnetic field application (Color : green, fluorescently labeled MCSN; red, DOX; yellow, merged green and red). (c) Quantification of cell death after various treatments shown in b.

1.2. Gold (Au) plasmonic nanoparticles for cancer photothermal therapy and optical imaging

When Au plasmonic nanoparticles (NPs) absorb light, the oscillating electromagnetic field of the light generates polarization of the conduction band electrons on the surface of the nanoparticles, and the polarized electrons move through coherent oscillations with respect to the positive ions in the metal. These oscillations are called as surface plasmon resonance (SPR) (Figure 7a) [4, 51]. The excited surface plasmon electrons relax in two ways; 1) scattering : emit the light which has the same energy of incident light, 2) absorption : transfer the absorbed energy to the form of thermal energy.

Au plasmonic NPs that have significant absorption in the tissue optical window (650 ~ 900 nm), which is also known as NIR window, are promising NIR imaging or agent. In the NIR window region, light absorption was minimized by hemoglobin (< 650 nm) and water (> 900 nm) (Figure 7b) [3]. Therefore, NIR imaging can enable using Au plasmonic NPs due to the combined NIR light scattering and NIR window.

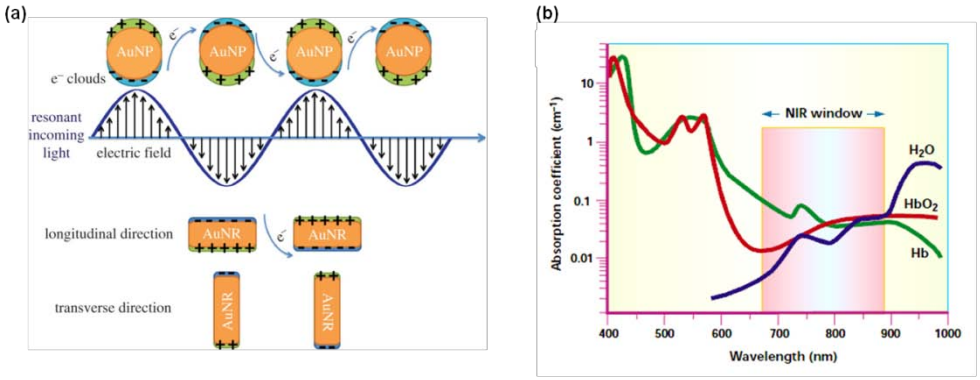

Figure 7. (a) Surface plasmon resonance (SPR) of spherical gold nanoparticles (AuNPs) and gold nanorods (AuNRs) [4,51]. (b) NIR optical window (650 ~ 900 nm) [3].

Near infrared (NIR) resonant nanomaterials, including Au nanoshell particles, Au nanorods, Au nanocages, and carbon nanotubes, were studied recently for cancer treatment because they strongly absorb NIR light and produce localized cytotoxic heat upon NIR irradiation [52]. Among these NIR resonant nanomaterials, Au plasmonic NPs show unique size and shape dependent optical and photothermal properties originated from localized surface plasmon resonance (LSPR), an electromagnetic mode related with the collective oscillation of free electrons in conduction bands of Au plasmonic NPs [2]. After excitation of LSPR by NIR laser, electron–electron and photon–electron interactions generate heat, which can be used to photothermal treatment, or to release drug in thermosensitive drug-delivery systems. When this photothermal treatment is combined with targeted delivery and chemotherapy, therapeutic efficacy is enhanced significantly [53-58]. The synthesis

of Au plasmonic NPs with controlled size and morphology led to the fabrication of various Au plasmonic nanostructures such as gold nanoshells (AuNSs), gold nanorods (AuNRs), hollow gold nanospheres (HAuNSs), and gold nanocages (AuNCs). These Au plasmonic nanostructures exhibit well-defined SPR absorption properties from visible to the NIR region [52].

1) Gold nanoshells (AuNSs)

Double stranded DNA (dsDNA) was attached to classical solid silica-cored AuNSs through an Au–thiol bond. A small molecule (fluorescent molecule) bound reversibly to dsDNA. After NIR irradiation, SPR band of AuNS dehybridized the DNA lead to release of single strand DNA (ssDNA). The released ssDNA diffused into the nucleus of cell (Figure 8a).

AuNSs composed of a mesoporous silica nanorattle core and a thin outer gold shell (SN@AuNSs) was also investigated. Docetaxel (DOC) as an anti-cancer drug and transferring (Tf) as a targeting moiety were incorporated into the SN@AuNSs, which exhibited cancer thermo-chemotherapy and imaging (Figure 8b).

2) Gold nanorods (AuNRs)

AuNRs usually have two LSPR peaks (transverse mode and longitudinal mode) from visible to NIR region [59]. To enhance drug contents of AuNRs, mesoporous silica-coated AuNRs ($Au@SiO_2$) was fabricated for hyperthermia therapy and imaging in cancer-cell (Figure 8c).

In addition, anti-cancer drug (doxorubicin, DOX) was intercalated into the DNA duplex strands which bound to the AuNRs surface, provide a DNA-targeting drug. After NIR laser illumination, DOX was released at the *in vivo* tumor site (Figure 8d).

3) Hollow gold nanospheres (HAuNSs)

HAuNSs as the photothermal agnet was incorporated into the PLGA microsphere which containing paclitaxel (PTX) as an anti-cancer drug. Drug release was enhanced upon NIR laser illumination lead to inhibition of tumor in *in vitro* and *in vivo* systems (Figure 8e). Further thermo-chemotherapy of tumor was performed by targeting moiety-conjugated to DOX@HAuNSs (Figure 8f).

4) Gold nanocages (AuNCs)

AuNCs are hollow cubic gold nanostructures, which have ultrathin, porous walls, and truncated corners. The LSPR peaks of AuNCs can be adjusted by

controlling the wall thickness and the size of AuNCs. AuNC-based drug-delivery system was fabricated by coating the surface of AuNCs with thermosensitive polymers [poly-(N-isopropylacrylamide), pNIPAAm]. This pNIPAAm conformation was changed after temperature increase up to the certain threshold and the drug was release from the AuNC (Figure 8g). AuNC-based drug-delivery system combined magnetic targeting for cancer therapy was also studied (Figure 8h).

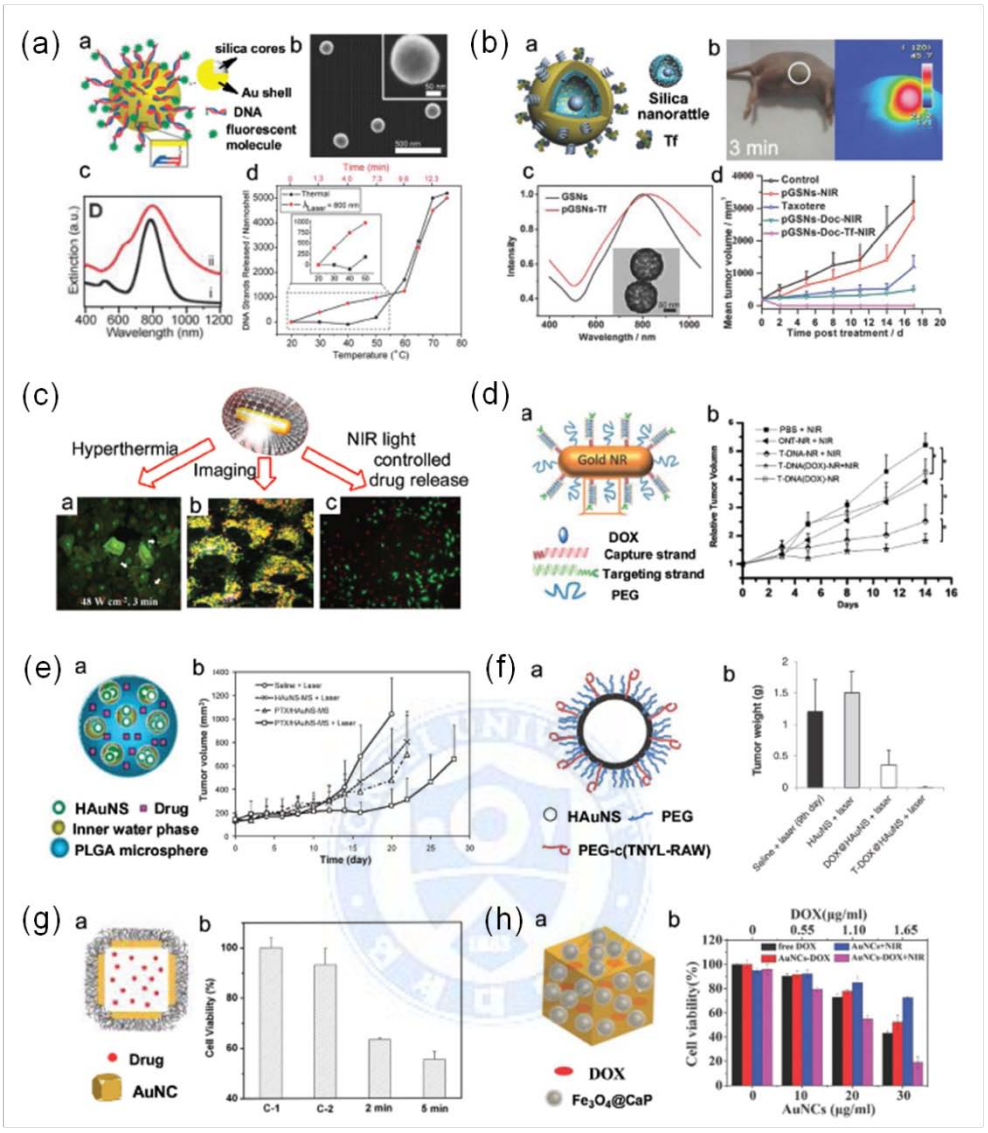

Figure 8. Various kinds of Au plasmonic nanoparticles used for cancer photothermal therapy and optical imaging [52].

(a) Thermal and NIR laser-triggered release of ssDNA from AuNSs. a) Schematic diagram of dsDNA-modified AuNSs. b) Scanning electron microscope (SEM)

image of the AuNSs. c) Extinction spectra of i) gold nanorods (AuNRs) and ii) AuNSs.

(b) Docetaxel (DOC) as an anti-cancer drug and transferring (Tf) as a targeting moiety were incorporated into the SN (silica nanorattle)@AuNSs for the cancer thermo-chemotherapy and imaging. a) Schematic diagram of AuNSs with a core of silica nanorattle and with shells modified targeting ligand. b) Photo and infrared thermal image of tumor-bearing nude mouse after NIR light irradiation. c) Extinction spectrum of poly(ethylene glycol) (PEG)-modified gold nanoshells on silica nanorattles (pGSNs) and pGSNs-Tf, the inset is the TEM image of pGSNs-Tf. d) *In vivo* antitumor efficacy using pGSNs-Tf with NIR irradiation.

(c) Au@SiO2 as a multifunctional theragnostic platform. a) The photothermal effect on lysosomal membrane integrity of A549 cells. b) Intracellular localization image of DOX (red) and Au@SiO2 (blue) in A549 cells stained with Lyso-Tracker (green) using two-photon confocal microscope. c) Controlled DOX release within A549 cells after NIR irradiation (live and dead cells were stained).

(d) Targeted NIR-responsive AuNRs which are self-assembled with DNA for cancer thermo-chemotherapy. a) The schematic diagram of DNA assembled AuNRs. b) Antitumor effects of tumor-bearing mouse after different treatments.

(e) HAuNS-loaded microspheres (HAuNS-MSs) for phtothermal-chemotherapy. a) Schematic diagram of PTX-HAuNS-MSs. b) Antitumor effects of U87 human gliomas grown in nude mice after different treatments.

(f) Targeted photothermal-chemotherapy of DOX-loaded HAuNSs. a) Schematic diagram of SH-PEG-c(TNYL-RAW) conjugated to HAuNSs. b) Antitumor effects of tumor-bearing mouse after different treatment.

(g) AuNCs for controlled durg release with NIR laser irradiation. a) Schematic representation of polymer-coated AuNCs for drug delivery. b) Cell viability after different treatments.

(h) Magnetic- and NIR- responsive drug release from AuNCs. a) Schematic diagram of Fe_3O_4@CaP-capped AuNCs. b) Cell viabilities after different concentrations of AuNCs.

1.3. Motivation of drug-loaded Au plasmonic nanoparticles

• Chemo-photothermal therapy and imaging of multidrug resistance in cancer

The nanoparticles (NPs)-based photothermal treatment generates heat intracellularly, whereas conventional hyperthermia provides heat extracellularly. Thus, heat is delivered to cells more effectively with photothermal treatment than with hyperthermal treatment, and heat generated intracellularly is expected to facilitate the ability to overcome MDR tumors. A hypothesis is that, the intracellularly generated heat which is originated from NPs may enhance the uptake of doxorubicin (DOX) and suppress the export of DOX (Figure 9). To test this hypothesis, DOX-loaded-poly(lactic-co-glycolic acid)-Au half-shell nanoparticles (DOX-PLGA-Au H-S NPs) with targeting moieties (anti-DR4 antibody) conjugated on the Au surface (DR4-DOX-PLGA-Au H-S NPs) were developed; DR4-DOX-PLGA-Au H-S NPs were NIR resonant due to the Au half shells. The *in vitro* and *in vivo* therapeutic effects of the chemo-photothermal treatment using these NPs and NIR irradiation were investigated.

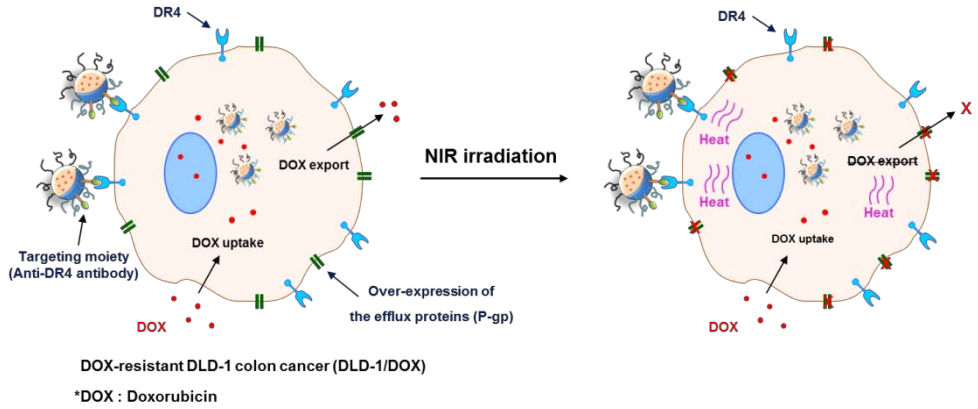

Figure 9. Motivation of chemo-photothermal therapy and imaging of multidrug resistance in cancer using drug-loaded Au plasmonic nanoparticles.

• Chemo-photothermal therapy and imaging of rheumatoid arthritis

The nanoparticles (NPs)-based photothermal treatment have been mainly focused on cancer treatments [52]. However, a limited penetration depth of NIR light hinders their practical application in the cancer treatments.

There are five motivations in therapy and imaging of rheumatoid arthritis; 1) Synovial inflammation in multiple joints within the penetration depth of NIR light (Figure 10), 2) Synovial proliferation of RA resembles solid tumors in many ways, including the leaky nature of the associated blood capillaries (similar w/ “enhanced permeability and retention (EPR) effect” in tumor) [60-61], 3) The NPs injected into the collagen induced arthritic (CIA) mice were effectively delivered to the

inflamed joint using RGD peptides (targeting moiety for inflammation), 4) The high retention of NPs (Fe-contained) at inflammation region under external magnetic field, 5) Adverse effects of drug (MTX) could be minimized by using carrier-NPs.

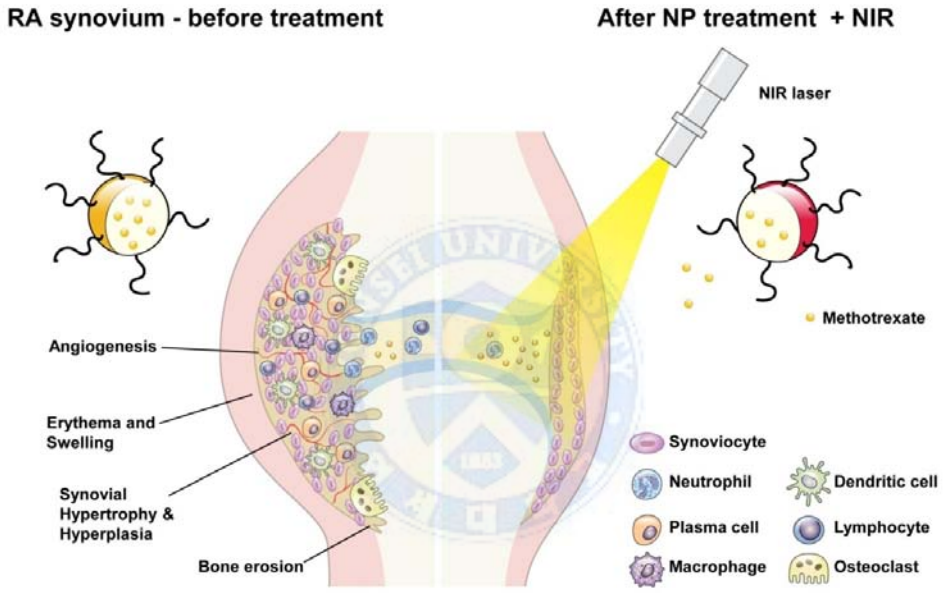

Figure 10. Chemo-photothermal therapy of rheumatoid arthritis using drug-loaded Au plasmonic nanoparticles.

Chapter 2.

In vivo chemo-photothermal therapy and imaging of multidrug resistance in cancer

2.1. Introduction

2.1.1. Multidrug resistance (MDR) in cancer

Chemotherapy is one of the major approaches for treating cancer. Other major approaches include surgery, radiotherapy, hyperthermia, and immunotherapy. However, conventional cancer chemotherapy is limited by multidrug resistance (MDR) in at least 50% of patients [62-64]. As shown in Figure 11, cellular mechanisms of drug resistance have been deeply studied, and three different mechanisms were suggested [63].

First, expression of ATP-dependent efflux pumps results in hydrophobic drug resistance (sometimes known as classical multidrug resistance). Intracellular drug

accumulation decreased because of efflux pumps expressed on cell surface. There are some kinds of drugs which are affected by efflux pumps, such as vinblastine, vincristine, doxorubicin, daunorubicin, and paclitaxel. Increased efflux pumps also related to decreased influx of drug into the cell. So, drugs that are entered via endocytosis did not work effectively. Examples drugs include methotrexate, 5-fluorouracil, and cisplatin.

Second, MDR is related to activation of detoxifying systems, such as DNA repair and the cytochrome P450 (a group of enzymes that are involved in drug metabolism and detoxification) mixed-function oxidases.

Finally, MDR can result from blocked apoptosis pathways originated from malignant transformation of cancer, including cancer with mutant or non-functional p53 [65]. Alternatively, cells decrease ceramide levels or change cell-cycle machinery during exposure to chemotherapy, resulting in prevention of apoptosis of cancer.

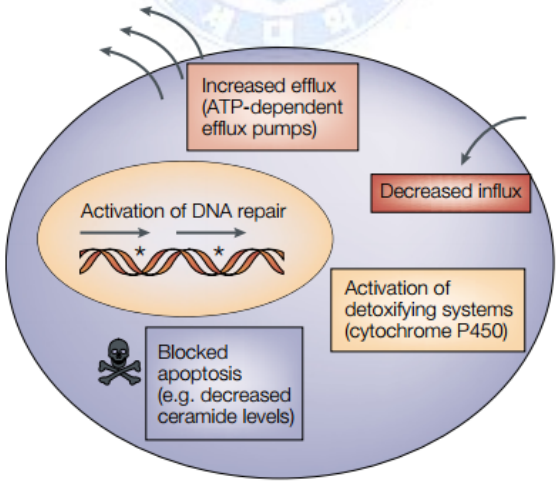

Figure 11. Cellular mechanisms of multidrug resistance (MDR) [63].

One well-studied mechanism of MDR involves over-expression of membrane transporters, particularly ABC transporter P-glycoprotein (P-gp; known as MDR1, encodes by ABCB1) [66-68]. P-gp is a multidrug efflux pump which has twelve transmembrane regions and two ATP-binding sites (Figure 12). Stimulation of the ATPase activity of P-gp was performed after binding hydrophobic drugs to the transmembrane regions, leading to release of hydrophobic drugs to either outer of the membrane or the extracellular space and prevent intracellular accumulation [69].

To overcome MDR, many MDR transporter inhibitors have been developed; some are in clinical trials, including verapamil (calcium channel blocker) and cyclosporin A (immunosuppressant) but none are currently in clinical use [63].

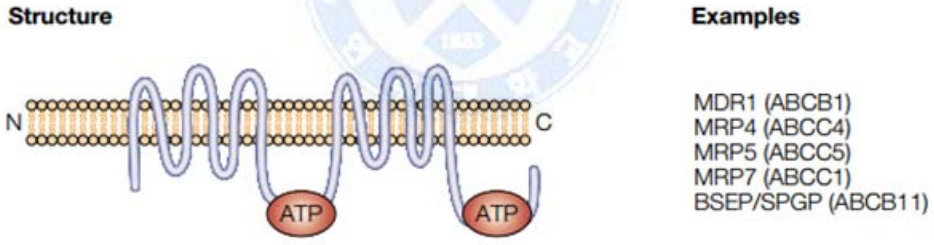

Figure 12. Structure and examples of ABC transporter P-glycoprotein (P-gp) [63].

2.1.2. Naomaterials as therapeutic agents for MDR in cancer

A variety of nanomaterials, including polymeric nanoparticles, lipid nanocapsules, micelles, and mesoporous silica particles that can carry chemotherapeutic agents, siRNA, photosensitizers, or a combination of multiple therapeutic agents have been developed. While these nanomaterials have been shown to reverse the actions of MDR transporters and altered apoptosis pathways to defeat MDR in cancer, clinical trials have been limited due to low efficacy and/or high toxicity [70]. To overcome these problems, combinatorial nanoparticles containing multiple cytotoxic drugs have been developed (Table 2) [70]. Among them, dual-drug liposomes (CPX-351 or CPX-1) with specific molar ratio of drugs showed superior therapy than traditional combination therapy and used for clinical trials (phase II).

Table 2. Combination strategies of nanoparticle formulations against clinical cancer drug resistance [70].

Nanocarrier platform	Drug combinations	Indication	Significance	Status
Liposome (CPX-351)	5:1 cytarabine and daunorubicin	Acute myeloid leukemia	Ratiometric drug loading with synergistic ratio maintained *in vivo*	Phase II
Liposome (CPX-1)	1:1 irinotecan and floxuridine	Colorectal cancer	Ratiometric drug loading with synergistic ratio maintained *in vivo*	Phase II
PLGA-PEG nanoparticle (aptamer-conjugated)	Cisplatin and docetaxel	Prostate cancer	Hydrophobic and hydrophilic drugs are co-encapsulated with differential drug release	*In vitro*
PLGA-PEG nanoparticle (aptamer-conjugated)	Doxorubicin and docetaxel	Prostate cancer	Hydrophobic and hydrophilic drugs are co-encapsulated	*In vitro*
Lipid-polymer hybrid nanoparticle	Doxorubicin and camptothecin	Pancreatic cancer	Adjustable ratiometric drug loading	*In vitro*
Lipid-coated PLGA nanocell	Combretastatin and doxorubicin	Lung carcinoma and melanoma	Temporally sequenced drug release achieves higher efficacy	*In vivo*
PLGA-PEG nanoparticle	Combretaastatin and paclitaxel	Lung carcinoma and melanoma	Temporally sequenced drug release achieves higher efficacy	*In vivo*
HPMA-Gem-Dox	Gemcitabine and doxorubicin	Prostate cancer and various cancer types	Enzyme-labile drug linkers enables differential drug release	*In vivo*

2.2. Experimental details

2.2.1. Fabrication of DR4-DOX-PLGA-Au plasmonic NPs

First, DOX-PLGA (Poly(lactic-*co*-glycolic acid) (PLGA; L:G molar ratio=50:50; MW=20,000)) NPs were synthesized using the solvent evaporation method [53-58]. Briefly, PLGA (200 mg) and DOX (6 mg) were dissolved in dichloroethane (20 ml), and this organic solution (oil phase) was added slowly drop-wise with distilled water (200 ml) containing Pluronic F-127 (200 mg) as a stabilizer under magnetic stirring. After mixing the oil and water phase, the mixture was emulsified by ultrasonication for 1 hr (400 W), followed by evaporation of organic solvent (dichloroethane) with stirring for 1 day. Then, the DOX-PLGA NPs were collected by centrifugation, and re-dispersed in 5 ml PBS by sonication. Next, the DOX-PLGA-Au H-S NPs were obtained by depositing 15-nm thick Au layers onto a monolayer of DOX-PLGA NPs, which were prepared by spin-casting aqueous suspensions of NPs on a silicon substrate. After depositing the Au film, DOX-PLGA-Au H-S NPs were released from the substrate into 1 wt% SH-PEG-COOH solution by sonication and collected by centrifugation. For targeted delivery to DLD-1 or DLD-1/DOX cells over-expressing DR4 receptors, anti-DR4 antibodies were conjugated on the surface of Au half-shells with protein G as a linker. To determine the amount of DOX loaded in NPs, 5 mg of dried NPs was dissolved in 1 ml of methylene chloride and the DOX extracted by adding 10 ml of

phosphate-buffered saline (PBS, pH 7.4). The amount of DOX was measured using an ultraviolet-visible spectrometer at 480 nm.

2.2.2. Preparation and culture of DLD-1/DOX cells

The DLD-1 colon cancer cell line was purchased from ATCC (American Type Culture Collection). DLD-1 cells were treated with DOX at the LD50 (50% lethal dose) for more than 4 months and established as the DOX-resistant DLD-1 cell line (DLD-1/DOX).

2.2.3. Human tumor xenografts

Female BALB/c nude mice (8 weeks old, ~20 g) were supplied by Orient Bio INC. (Seongnam, Korea). All animal experiments were performed in accordance with the Korean Food and Drug Administration (KFDA) guidelines. Protocols were reviewed and approved by the Institutional Animal Care and Use Committee (IACUC) of the Yonsei Laboratory Animal Research Center (YLARC) (Permit #: 2011-0069). All mice were maintained in a specific pathogen-free facility at the YLARC. The animals had access to food and water ad libitum. For tumor induction, cells were harvested after trypsinization and 5×10^6 viable cells injected subcutaneously into the flanks of mice. Nude mice that underwent NIR

irradiation were anesthetized with Zoletil50/Rompum (v/v = 3) prior to NP injection.

2.3. Results and discussion

2.3.1. Characterization of DR4-DOX-PLGA-Au plasmonic NPs

The DR4-DOX-PLGA-Au H-S NPs were prepared as shown in Figure 13a. The Au half-shell structure was clearly seen in the TEM image of these NPs (Figure 13b). The sizes and zeta-potentials of NPs in aqueous medium measured at 25 °C by dynamic light scattering (DLS, Zetasizer Nano ZS, Malvern Instruments Ltd.) are summarized in Table 3. The average diameter of DR4-DOX-PLGA-Au H-S NPs was ~144 nm, and the SEM image of NPs revealed relatively uniform sizes (Figure 14a). The ultraviolet-visible/NIR absorption spectra of DOX-PLGA-Au H-S and DR4-DOX-PLGA-Au H-S NPs exhibited a pronounced peak at approximately 820 nm due to Au half-shells (Figure 13c), suggesting that both nanoparticles can be used for photothermal treatment and *in vivo* NIR absorbance imaging.

The DOX loading content (the ratio of DOX mass loaded into NPs relative to the total NP mass) was estimated to be ~3.9%. For targeted delivery to DLD-1 or DLD-1/DOX cells that over-express DR4 receptors (Figure 15), anti-DR4

antibodies were conjugated on the Au surface and their conjugation confirmed by western blot for anti-DR4 antibody (Figure 14b). The ratio of the mass of anti-DR4 antibody relative to the total mass of DR4-DOX-PLGA-Au H-S NPs was estimated to be ~4.8% based on the Bradford method using the Bio-Rad protein assay. I also tested the stability of NPs in serum by measuring the absorbance of the NP solution at 820 nm as a function of time (Figure 13d and Figure 14c). The absorbance was nearly unchanged within 24 h in 10% serum (Figure 13d), indicating that the NPs were stable in serum.

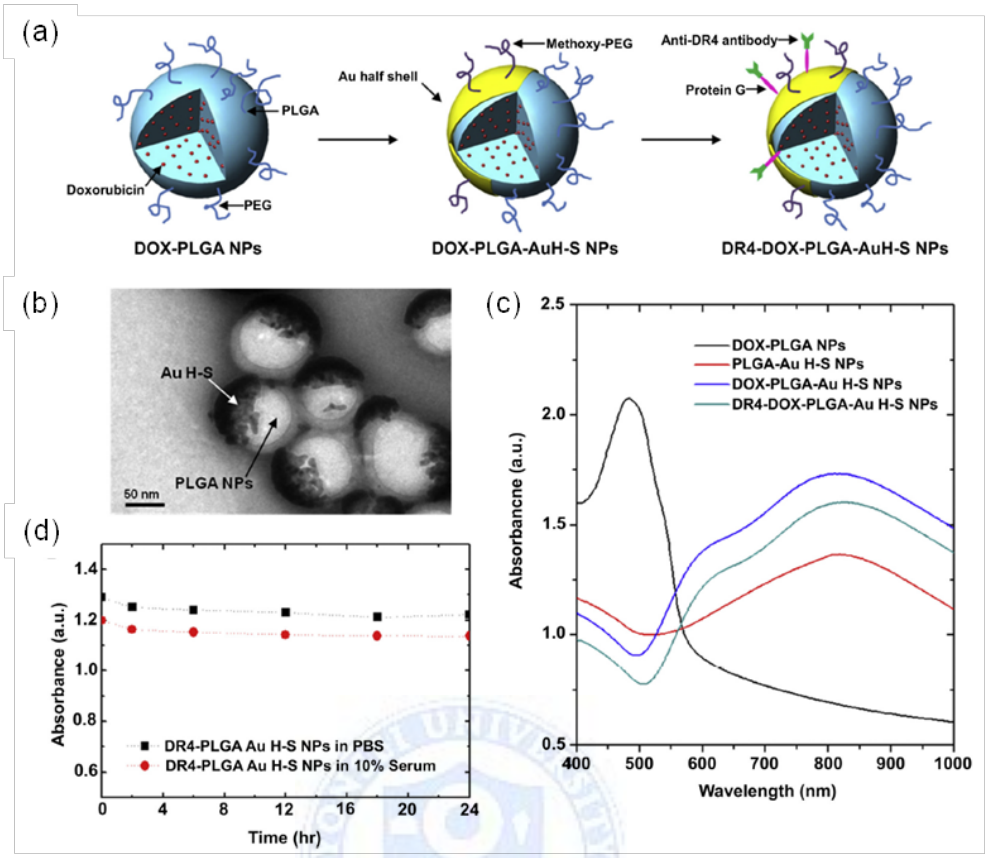

Figure 13. (a) Schematic diagrams showing the construction of DR4-DOX-PLGA-Au H-S NPs. (b) TEM image of DR4-DOX-PLGA-Au H-S NPs. (c) Visible/NIR absorption spectra of DOX-PLGA NPs, PLGA-Au H-S NPs, DOX-PLGA-Au H-S NPs, and DR4-DOX-PLGA-Au H-S NPs. (d) Stability of DR4-DOX-PLGA-Au H-S NPs. DR4-DOX-PLGA-Au H-S NPs were dispersed in 10% serum and their optical absorbance measured over a period of 24 h (red). Control PBS solution containing DR4-DOX-PLGA-Au H-S NPs (black).

Table 3. Characterization of prepared nanoparticles.

Nanoparticles	Size (nm) [a]	PDI[b]	Zeta-potential (mV)[c]
DOX-PLGA-Au H-S NPs	125 ± 2.529	0.143±0.029	-18.20±4.157
Protein G-DOX-PLGA-Au H-S NPs	134 ± 3.117	0.209±0.015	-6.470±1.109
DR4-Protein G-DOX-PLGA-Au H-S NPs	144 ± 3.394	0.206±0.019	-9.444±2.816
DR4-Protein G-DOX-PLGA-Au H-S NPs (after NIR irradiation for 10 min)	143 ± 2.040	0.181 ± 0.029	-9.444±2.816

[a,b,c]The size, polydispersiy index (PDI) and zeta-potential of the nanoparticles were measured by dynamic light scattering (DLS, Zetasizer Nano ZS, Malvern Instruments Ltd) at a concentration of approximately 1 mg of nanoparticles/1 ml of distilled water.

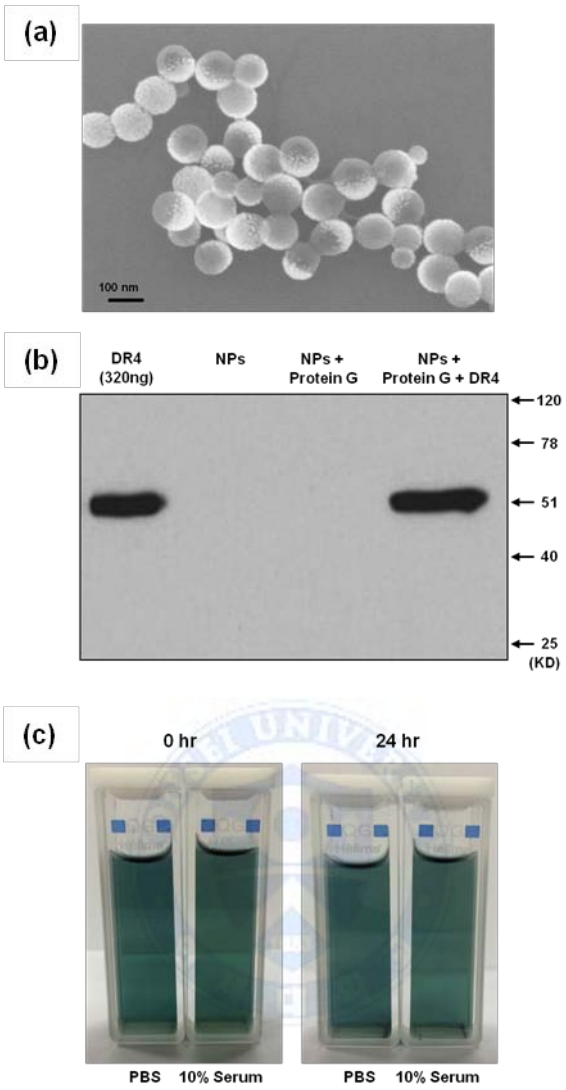

Figure 14. (a) SEM image of DR4-DOX-PLGA-Au H-S NPs. (b) Western blot for DR4 antibody in DR4-DOX-PLGA-Au H-S NPs. (c) Stability of DR4-DOX-PLGA-Au H-S NPs in 10% serum.

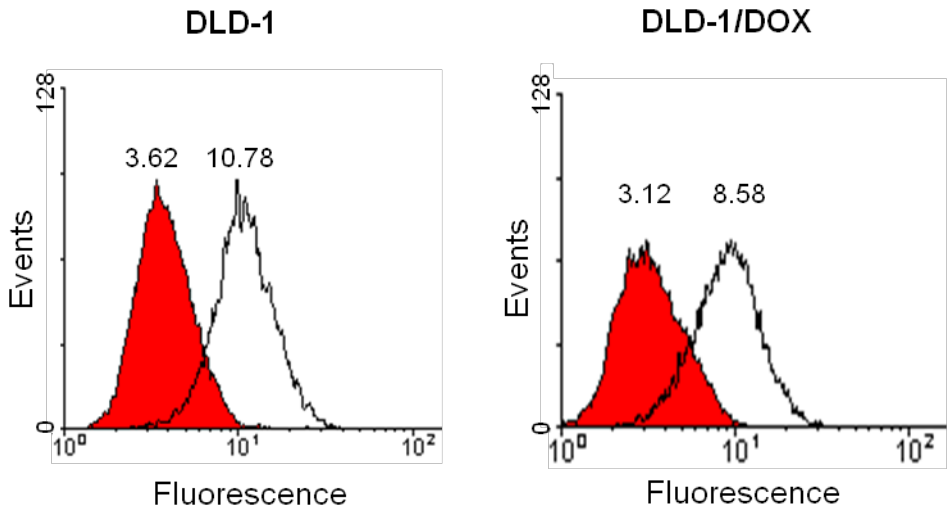

Figure 15. Flow cytometry analysis of DR4 expression in DLD-1 and DLD-1/DOX cell lines (Red: isotype control, black: anti-DR4 Ab).

To investigate the effects of NIR photothermal treatment combined with chemotherapy on DLD-1 and DLD-1/DOX cells, cell viability was measured using CCK-8 (Figure 16). DLD-1 and DLD-1/DOX cells (1×10^4 cells/ml) were seeded onto 24-well plates and incubated in RPMI 1640 medium at 37 °C for 1 day. After each treatment, the cell viability, based on a CCK-8 assay, was determined by measuring the absorbance at 450 nm using a Multilabel Plate Reader (Victor X5, Perkin Elmer). All of the measurements were performed in triplicate.

After treatment with DOX (100 μg/ml) for 3 days, cell viability was reduced to ~ 59% in DLD-1 cells and 90% in DLD-1/DOX cells. Next, DLD-1 or DLD-1/DOX cells were pre-treated with PLGA-Au H-S NPs (30 μg/ml) containing no

DOX for 24 h and then exposed to NIR light (0.7 W/cm^2) using a laser diode (λ = 808 nm) for 10 min, followed by further incubation at 37 °C for 3 days. Upon NIR irradiation, the temperature increased to approximately 45 °C, which is comparable to the temperature of conventional hyperthermal treatments (Figure 17). In this case, the cell viability was reduced to ~ 80% for DLD-1 cells and ~ 68% for DLD-1/DOX cells. Finally, DLD-1 or DLD-1/DOX cells were pre-treated with PLGA-Au H-s NPs (30 μg/ml) for 24 h, and then treated with DOX (100 μg /ml) and exposed to NIR light (0.7 W/cm^2) for 10 min. Cell viability was reduced to approximately 18% and 41% for DLD-1 and DLD-1/DOX cells, respectively. These values were lower than expected for the additive effects of DOX and photothermal treatment on cell viability. These results suggest that MDR tumors may be defeated with this chemo-photothermal treatment.

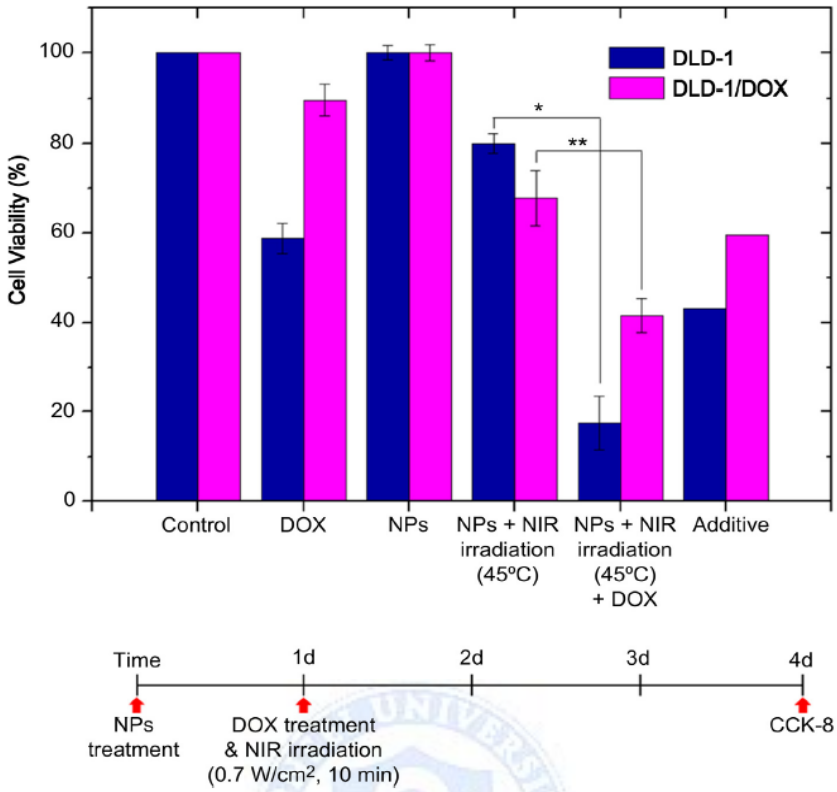

Figure 16. Viability of DLD-1 and DLD-1/DOX cells with chemo-photothermal therapy. DLD-1 and DLD-1/DOX cells were treated with DOX only (DOX), NPs without (NPs) or with NIR (NPs + NIR irradiation), or NPs with NIR and DOX treatment (NPs + NIR irradiation + DOX). The additive therapeutic efficacies of chemo and photothermal treatments were estimated using the relationship $T_{\text{additive}} = 100 - (f_{\text{chemo}} \times f_{\text{photothermal}}) \times 100$, where f is the fraction of surviving cells after each treatment. Data represent mean ± SD (n = 3). When the chemo-photothermal therapy is compared to photothermal therapy and the additive value using the t test, p-value ≤ 0.005 (*p = 0.003, **p = 0.0017).

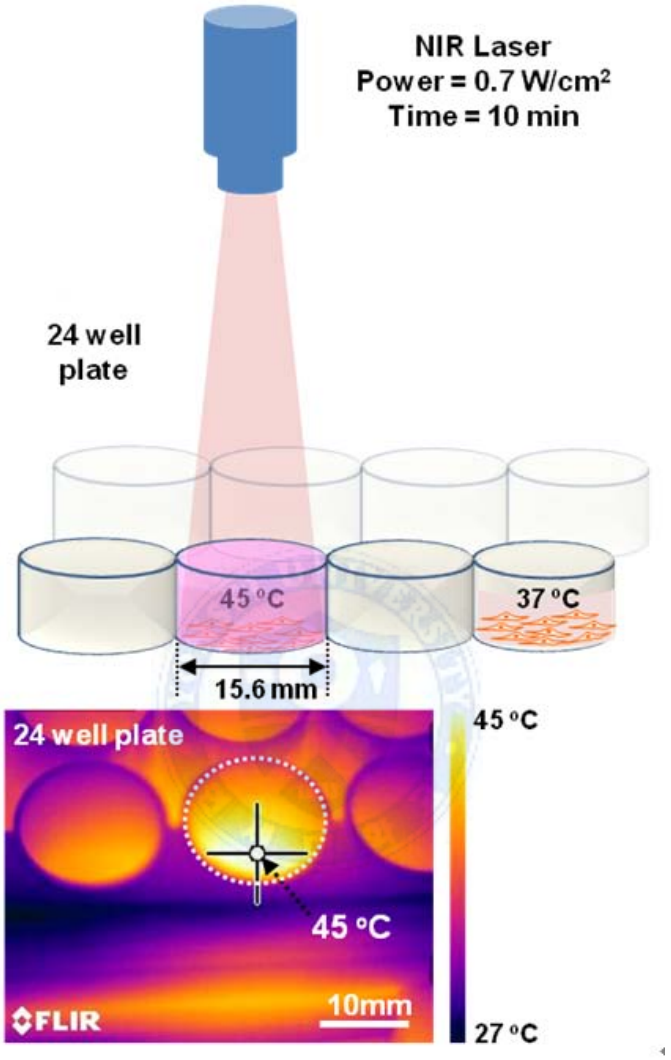

Figure 17. The schematic diagram of a 24 well plate containing cells under NIR irradiation of 0.7 W/cm^2 for 10 min (top) and its thermal image (bottom).

2.3.2. DOX uptake in DLD-1/DOX cells

To investigate the origin of the synergistic effects of chemo-photothermal treatment on DLD-1 and DLD-1/DOX cells, the influence of photothermal treatment on DOX uptake in DLD-1 and DLD-1/DOX cells was investigated. Human colon cancer (DLD-1) and DOX-resistant DLD-1 (DLD-1/DOX) cell lines were treated with a DOX solution (20 μg/ml), and fluorescence images were acquired before and after incubation at 45 °C. For the photothermal treatments, DLD-1 and DLD-1/DOX cells were first incubated with PLGA-Au H-S NPs (30 μg/ml, without DOX) for 24 h. The cells were then treated with DOX and exposed to NIR light delivered at 0.7 W/cm^2 by a laser diode (λ = 808 nm) for 10 min. The cellular uptake of DOX was also measured by a flow cytometry (BD Biosciences). As a control, DLD-1 and DLD-1/DOX cells were treated with DOX (20 μg/ml) at 37 °C for 4 h, followed by the measurement of intracellular DOX retention with flow cytometry after incubating for 1, 2, 3, and 6 h. To test the photothermal treatment, DLD-1 or DLD-1/DOX cells were treated with DOX (20 μg/ml) in the presence of PLGA-Au H-S NPs (30 μg/ml, without DOX) for 4 h, exposed to NIR light (0.7 W/cm^2) for 10 min, and washed with PBS. Uptake was measured in DOX-treated DLD-1 and DLD-1/DOX cells exposed or not exposed to NIR light. Approximately 10,000 events were acquired per sample, and the data were analyzed using FACS Comp™ software. Forward and side light scatter gates were set to exclude dead cells, debris, and cell aggregates.

As a control, DLD-1 and DLD-1/DOX cells were incubated at 37 °C and treated with 20 μg/ml DOX solution, suboptimal dose of one-fifth of LD50. At 37°C, red fluorescence was observed in DLD-1 cells due to internalized DOX (Figure 18a). In contrast, red fluorescence was not detected in DLD-1/DOX cells at 37 °C (Figure 18b), indicating that the DLD-1/DOX cells were pumping DOX out of the cells.

For photothermal treatments, DLD-1 and DLD-1/DOX cells were incubated with PLGA-Au H-S NPs (30 μg/ml, without DOX) for 24 h. Next, the cells were treated with 20 μg/ml DOX solution and exposed to NIR light (0.7 W/cm^2) for 10 min. Unlike incubation at 37°C, the photothermal treatment resulted in enhanced uptake of DOX in both DLD-1 and DLD-1/DOX cells (Figure 18c and d). These results suggest that the internalized DOX was not immediately pumped out from the DLD-1/DOX cells after the photothermal treatment, which led to increased intracellular accumulation of DOX. For a comparison, the effects of hyperthermal treatments by warming cancer cells to 45 °C for 10 min, which was the same temperature increase caused by NIR irradiation were also investigated. Compared to the control, no significant change in DOX accumulation was observed at 45 °C for the two cell types (Figure 18e and f).

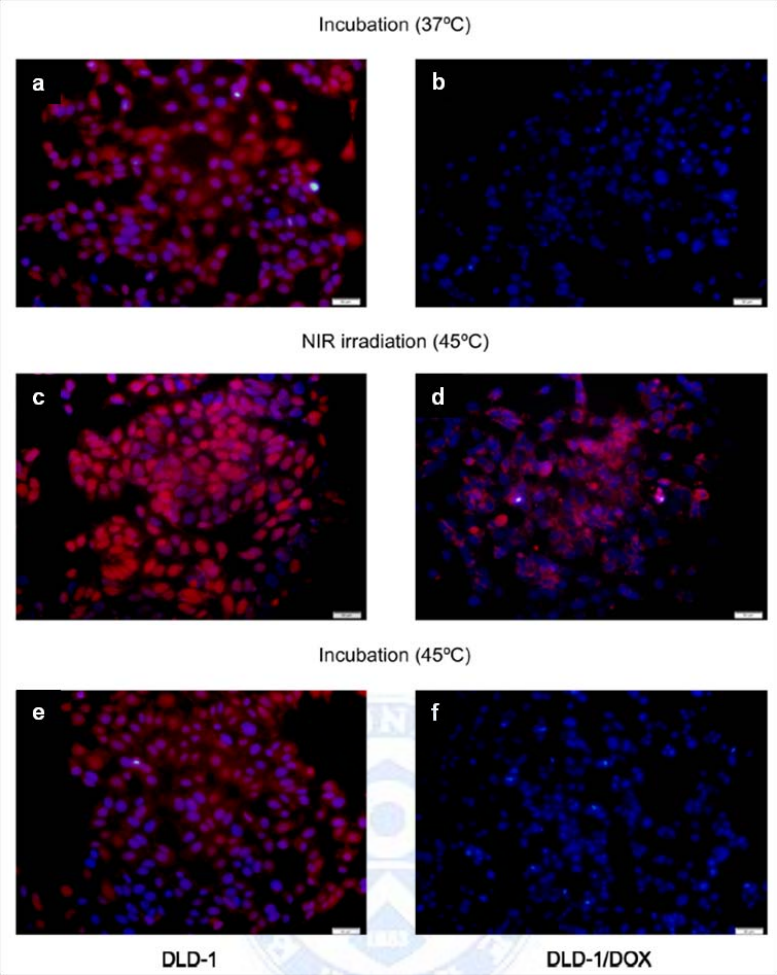

Figure 18. Thermal and photothermal effects on DOX uptake in a multidrug-resistant cancer cell line. Fluorescence images show DOX retention in cancer cells sensitive (DLD-1) or resistant (DLD-1/DOX) to DOX. Thermal effects are shown in cells treated with 20 μg/ml of DOX and incubated at 37 °C (a and b) or 45 °C for 10 min (e and f). Photothermal effects are shown in cells pre-treated with PLGA-Au H-S NPs for 24 h followed by 20 μg/ml DOX, and exposed to NIR light (0.7 W/cm^2, 10 min) (c and d). NIR irradiation elevated the temperature to 45 °C. Scale bar = 50 μm. (red : DOX, blue : cell nucleus).

To quantify the accumulation of drug in DLD-1 and DLD-1/DOX cells after the photothermal treatment, flow cytometric analysis of DOX fluorescence in DLD-1 and DLD-1/DOX cells exposed to NIR light was performed. For the control, DLD-1 and DLD-1/DOX cells were treated with DOX (20 μg/ml) at 37 °C for 4 h and intracellular DOX retention measured by flow cytometry 1, 2, 3, and 6 h later. We found that DOX was absorbed well in DLD-1 cells but then actively pumped out to maintain baseline intracellular levels after 6 h. To test the photothermal treatment, DLD-1 or DLD-1/DOX cells were treated with DOX (20 μg/ml) in the presence of PLGA-Au H-S NPs (30 μg/ml) for 4 h and then exposed to NIR light (0.7 W/cm^2) for 10 min, followed by washing with PBS. An increased fluorescence intensities for both DLD-1 and DLD-1/DOX cells exposed to NIR light were observed (Figure 19). These observations support the accumulation of DOX in DLD-1/DOX cells being enhanced by photothermally generated heat.

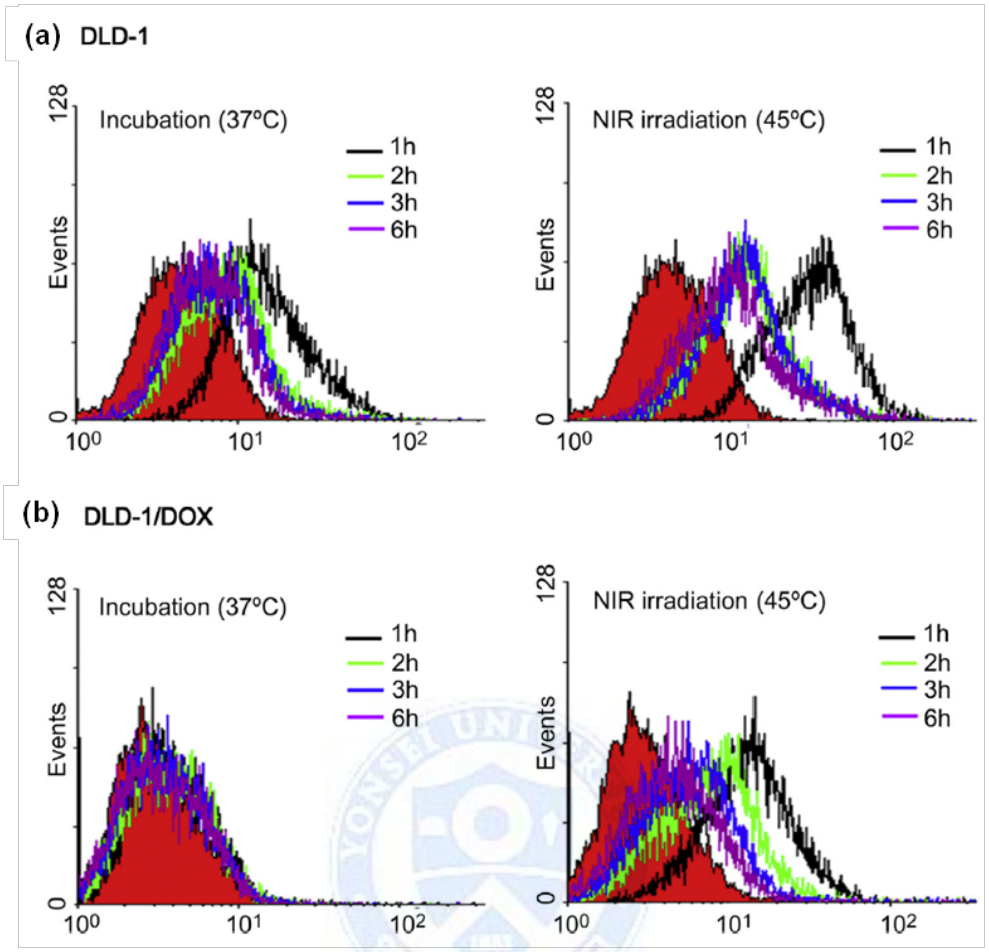

Figure 19. Thermal and photothermal effects on DOX retention in a multidrug resistance cancer cell line. (a) Flow cytometric analysis of DOX-treated DLD-1 and (b) DLD-1/DOX cells.

2.3.3. P-gp expression and activity in cells after photothermal treatment

The efflux of DOX is related to the level of P-gp expression [71-72]. Therefore, P-gp expression in DLD-1/DOX cells with or without photothermal treatment was measured. P-gp expression level was measured by a flow cytometry (BD Biosciences). Briefly, DLD-1 and DLD-1/DOX cells were incubated with PLGA-Au H-S NPs in complete RPMI 1640 medium at 37 °C for 24 h. After each treatment, the cells were blocked by 2% BSA in PBS at 4 °C for 30 min, followed by diluted anti-P-gp antibody (BD) in PBS with 1% BSA at 4 °C for 1 h. Cells were washed twice with PBS and incubated with Alexa 488-congugated IgG in PBS with 1% BSA. Approximately 10,000 events were acquired per sample and the data analyzed using FACS Comp™ software (BD). Forward and side light scatter gates were set to exclude dead cells, debris, and cell aggregates.

Regardless of whether cells underwent photothermal treatment, P-gp expression did not change (Figure 20). However, Figure 18 and Figure 19 show that DOX efflux was suppressed in photothermally treated DLD-1/DOX cells.

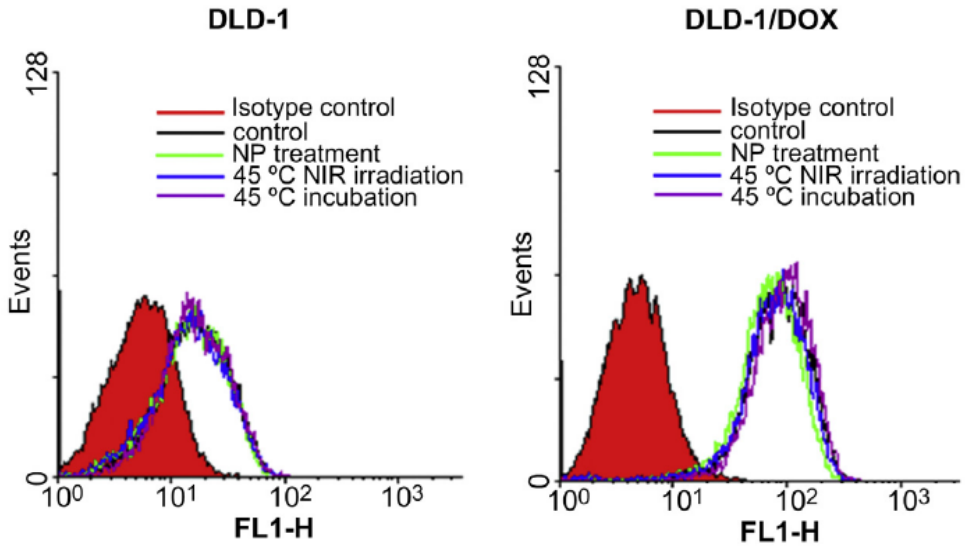

Figure 20. P-glycoprotein expression measured by flow cytometry for DLD-1 and DLD-1/DOX cells after treatment with NIR irradiation or incubation at 45 °C.

Based on these results, I conjectured that intracellularly-generated heat may reduce the activity of P-gp without changing protein levels. To test this idea, both DLD-1 and DLD-1/DOX cells were treated with PLGA-Au H-S NPs (30 μg/ml) and NIR, followed by the measurement of ATPase activity. P-gp is an ATP-binding cassette (ABC) transporter. In the ATPase assay, inorganic phosphate generated by ATP hydrolysis, which is linked with transporters, was determined by colorimetry as described previously [73]. After NIR irradiation, the ATPase activity of DLD-1 and DLD-1/DOX cells was measured using the Quantichrom ATPase/GTPase assay kit (Bioassay Systems) according to the manufacturer's instructions.

As shown in Figure 21, photothermal treatment with NIR decreased the ATPase activity. In contrast, warming the cells by incubation at 45 °C for 10 min resulted in no change in ATPase activity.

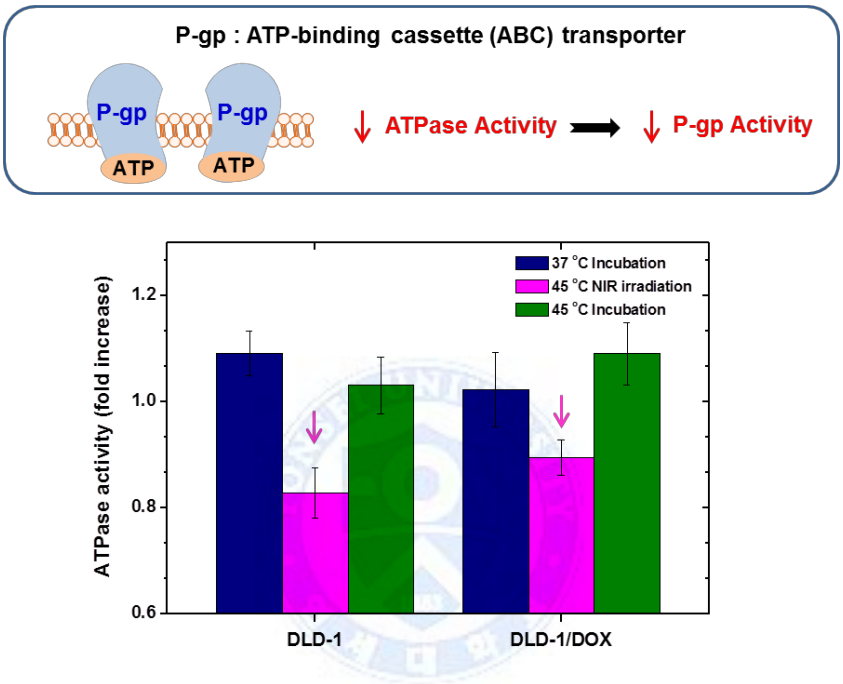

Figure 21. ATPase activities of DLD-1/DOX cells after treatment with NIR irradiation or incubation at 45 °C.

The fluorescence images of DLD-1 and DLD-1/DOX cells treated with DOX, NPs, and NIR are shown in Figure 22. Fluorescence intensity increased in DLD-1/DOX cells at 1 h, and then significantly decreased at 2 h, after NIR irradiation.

These results suggest that NIR irradiation enhanced the intracellular accumulation of DOX in DLD-1/DOX cells by NIR; however, the DOX retention time was short, so DOX was cleared out at 2 h. Next, we exposed DLD-1/DOX cells to NIR light again at 3 h. Interestingly, the fluorescence intensity increased again, indicating that intracellular accumulation of DOX was enhanced. These results support our idea that P-gp activity is affected by NP-based photothermal treatment.

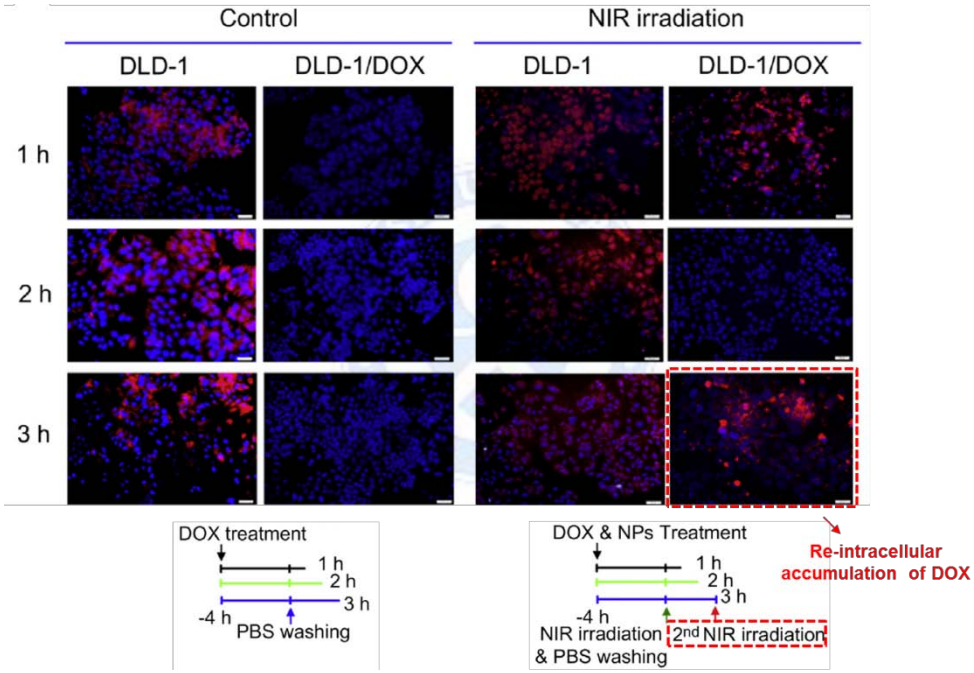

Figure 22. Fluorescence images of DLD-1 and DLD-1/DOX cells after different treatments. After one or twice exposures to NIR, the cells were washed with PBS and incubated in DOX-free media for the indicated times. Scale bar = 50 μm.
(red : DOX, blue : cell nucleus).

To confirm the uptake of NPs into cells, TEM study was also performed. DLD-1 and DLD-1/DOX cells (5×10^5 cells/ml) seeded onto 6-well plates were incubated with PLGA-Au H-S NPs (30 μg/ml, without DOX) in 3 ml RPMI 1640 medium at 37 °C for 24 h. The NP-treated cells were rinsed three times with PBS, dissociated using trypsin-EDTA, centrifuged, and the cell pellet collected. Ultra-thin (80 nm) sections of the cell pellet were prepared using a standard method and examined by TEM (JEM-1011, JEOL, Japan).

TEM images of NP-treated DLD-1/DOX cells are presented in Figure 23. Before NIR irradiation, DLD-1/DOX cells incubated with PLGA-Au H-S NPs (30 μg/ml, without DOX) at 37 °C for 24 h had internalized NPs by endocytosis, and the NPs were located primarily inside vesicles (Figure 23a) . After NIR irradiation for 10 min, apparent morphological changes were not noted and the NPs were observed inside vesicles (Figure 23b and c).

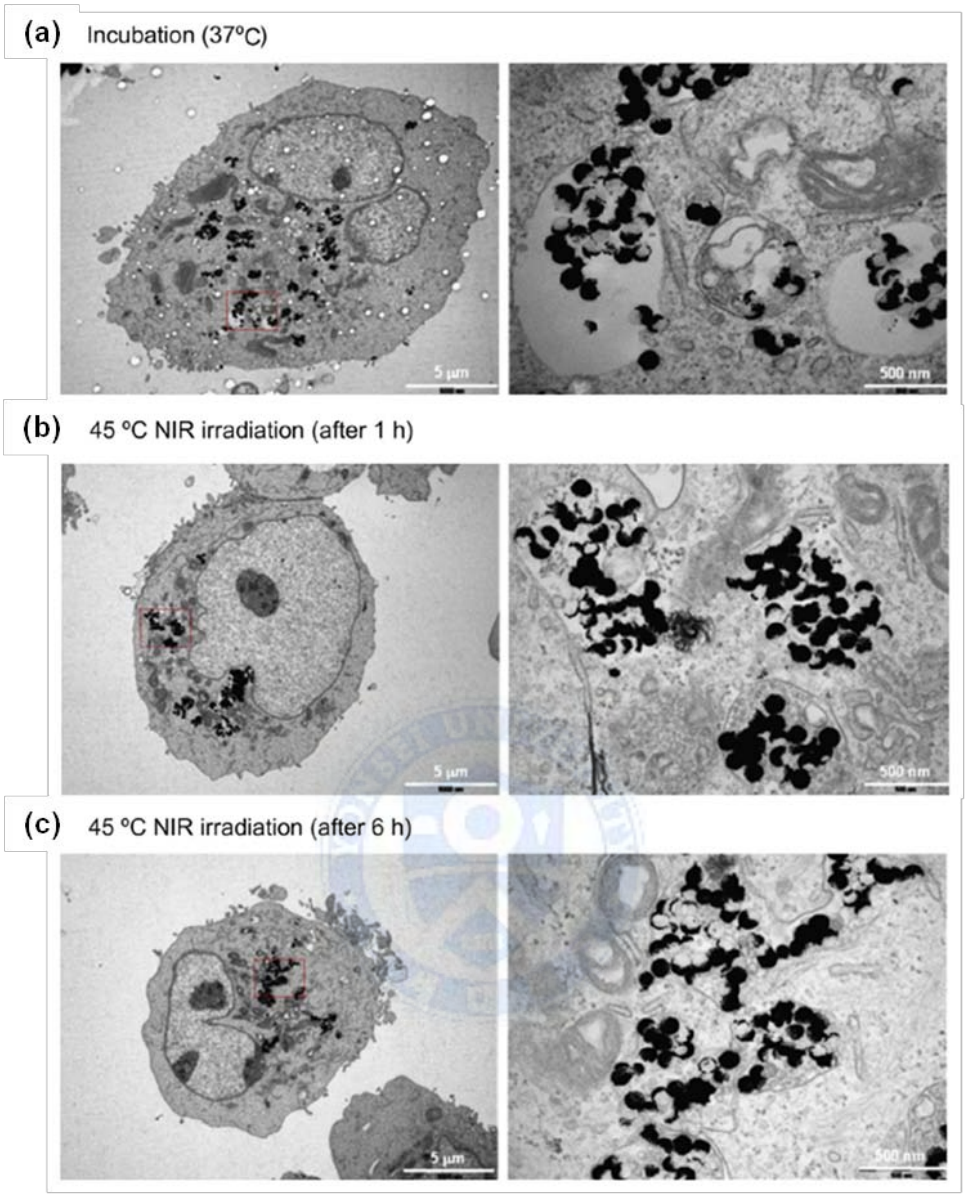

Figure 23. (a) TEM images of DLD-1/DOX cells incubated for 24 h with PLGA-Au H-S NPs at 37 °C. (b, c) TEM images of DLD-1/DOX cells incubated with PLGA-Au H-S NPs and then exposed to NIR light (0.7 W/cm^2 for 10 min). The TEM images were taken at 1 h (b) and 6 h (c) after NIR irradiation.

Figure 24 shows the optical image and fluorescence image of DLD-1/DOX cells incubated with DOX-PLGA-Au H-S NPs (30 μg/ml, DOX loaded in PLGA) obtained 6 h after NIR irradiation and PBS washing. Internalized NPs were still observed in DLD-1/DOX cells. As almost all DOX was pumped out at 6 h from the cells treated with DOX solution (Figure 14), these results imply that the NPs were much more slowly pumped out from DLD-1/DOX cells compared to DOX solution.

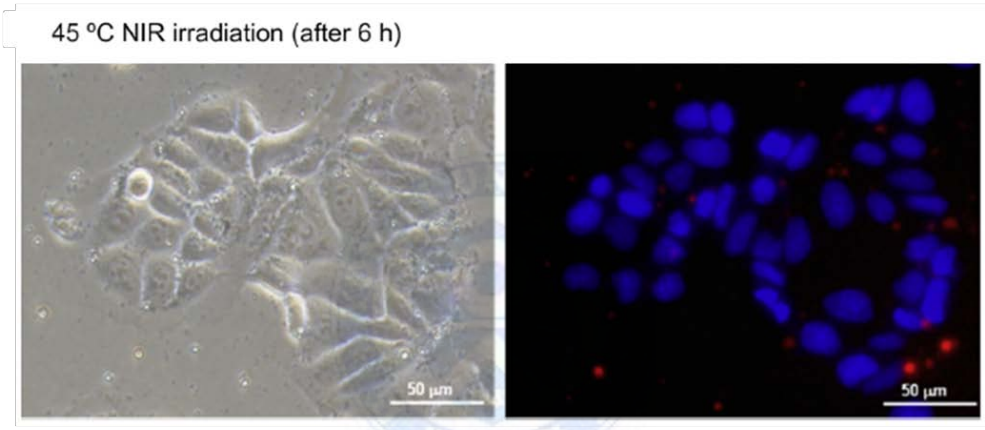

Figure 24. Optical image and fluorescence image of DOX-PLGA-Au H-S NPs (DOX loaded in PLGA) in DLD-1/DOX cells 6 h after NIR irradiation (0.7 W/cm^2, 10 min). (red : DOX which is loaded in PLGA-Au H-S NPs, blue : cell nucleus).

2.3.4. *In vivo* targeting efficacy

To evaluate the *in vivo* targeting efficacy of NPs, DR4-DOX-PLGA-Au H-S NP solution (200 μl of 1 mg/ml mixture dispersed in PBS) was intravenously injected into the tail vein of DLD-1 or DLD-1/DOX tumor-bearing mice. The injected DR4-DOX-PLGA-Au H-S NPs were monitored 24 h after injection by acquiring *in vivo* NIR absorbance images using the eXplore Optix System (Advanced Research Technologies Inc., Montreal, Canada). The mice were anesthetized with Zoletil50/Rompum (v/v = 3) during acquiring images.

Increased absorbance intensity was observed in the tumor regions in both DLD-1 and DLD-1/DOX tumor-bearing mice, indicating that DR4-PLGA-Au H-S NPs were effectively delivered to the tumor site, where they accumulated (Figure 25).

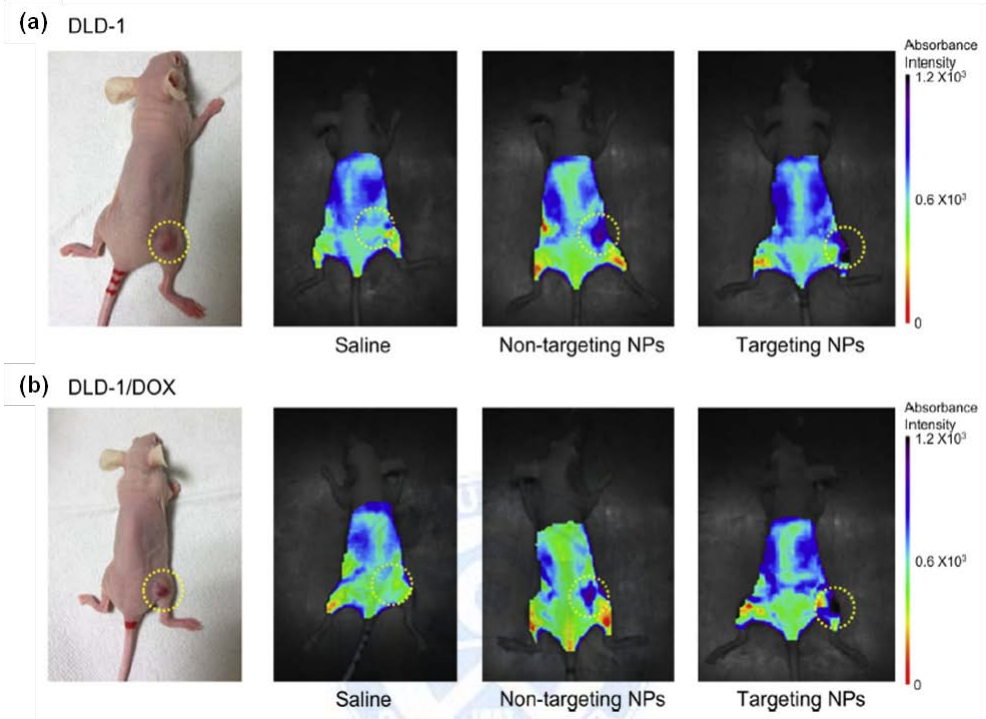

Figure 25. *In vivo* NIR absorbance images of (a) DLD-1 and (b) DLD-1/DOX tumor-bearing mice measured 24 h after intravenous injection of DR4-PLGA-Au H-S NP solution. The dotted circle is the tumor-containing region.

To determine whether drug efflux could also be suppressed by photothermal treatment in MDR tumor-bearing mice, I used technetium-99m methoxyisobutylisonitrile (^{99m}Tc-MIBI), a lipophilic cationic radiopharmaceutical transport substance that, like DOX, can be pumped out by P-gp, thus, it is often used for imaging MDR tumors [74]. ^{99m}Tc-methoxisobutylisonitrile (^{99m}Tc-MIBI) was prepared using the Mallinckrodt® kit (Mallinckrodt Medical, Petten, the Netherlands) according to the manufacturer's instructions. The radiochemical purity was greater than 95%. DLD-1/DOX tumor-bearing mice were anesthetized with Zoletil50/Rompum (v/v = 3) and 18.5 MBq of ^{99m}Tc-MIBI injected intravenously. Early and delayed ^{99m}Tc-MIBI images were acquired at 10 min, 3 h, and 4 h after injection of the radiotracer. Images were acquired for 10 min using a single head ARGUS gamma camera (Philips Medical Systems, Cleveland, OH, USA) with a matrix size of 512 × 512 × 16 with a pinhole collimator.

I acquired ^{99m}Tc-MIBI in DLD-1/DOX mice carrying tumors on both the left and right flank. The DR4-DOX-PLGA-Au H-S NP solution (200 μl) was injected intravenously. Twenty-four hours after injection, only the right tumor was irradiated with NIR light (1.82 W/cm^2) for 10 min. The temperature of the exposed tumor increased to approximately 45 °C, but the region that was not exposed to NIR light was 36.5 °C (Figure 26).

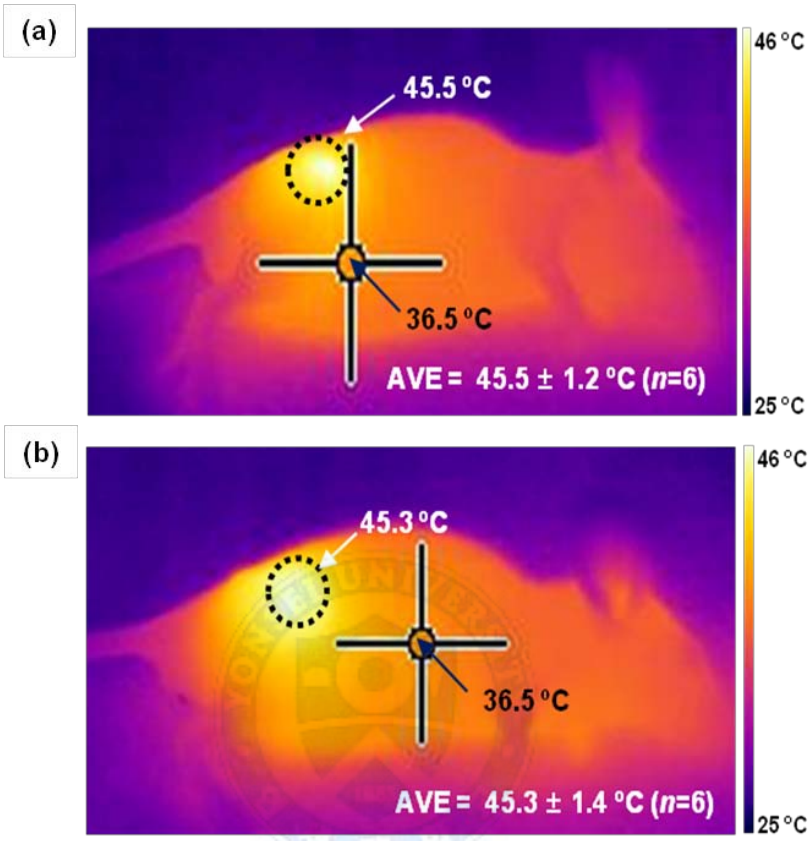

Figure 26. Thermal images of the (a) DLD-1 and (b) DLD-1/DOX tumor-bearing mice. DR4-PLGA Au H-S NPs solution was intravenously injected into the mice and NIR light of 1.82 W/cm^2 was irradiated only to the tumor region with a diameter of ~ 0.9 cm for 10 min.

As shown in Figure 27, almost no uptake was detected in either the left or right tumor 10 min after NIR irradiation. However, at 180 and 240 min, ^{99m}Tc MIBI uptake was increased in only the right tumor, which had been exposed to NIR light; in contrast, the intensity of ^{99m}Tc-MIBI was nearly unchanged for the non-irradiated, left tumor. Consequently, the ratios of ^{99m}Tc-MIBI accumulation in the right and left tumors were approximately 1.0, 2.5 and 3.0 at 10, 180 and 240 min, respectively. These ^{99m}Tc-MIBI images suggest that the NIR photothermal treatment inhibited P-gp activity, which suppressed drug efflux and enhanced drug accumulation.

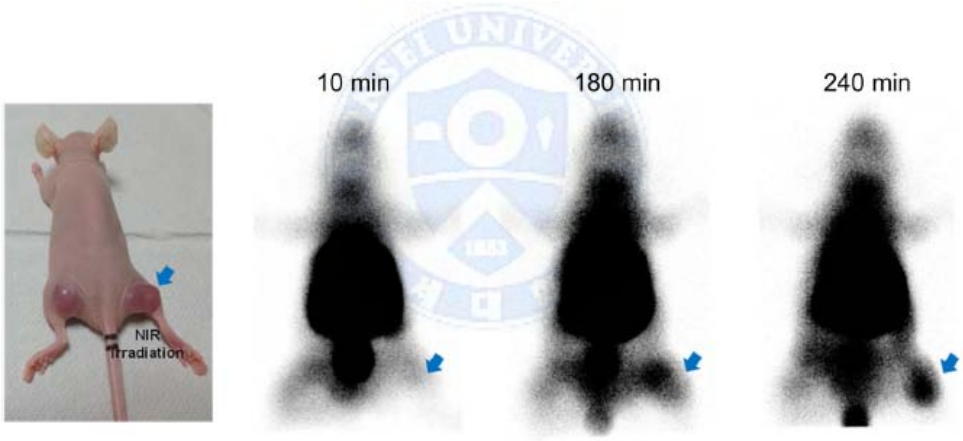

Figure 27. ^{99m}Tc-MIBI scintigraphy imaged at different times for an NP-treated DLD-1/DOX tumor-bearing mouse with tumors on both the left and right thighs. Only the right tumor (arrow) was irradiated with NIR light of 1.82 W/cm^2 for 10 min just before ^{99m}Tc-MIBI injection, and images were taken 10, 180, and 240 min after NIR irradiation.

2.3.5. *In vivo* therapeutic effects

To assess the therapeutic efficacy of targeted chemo-photothermal treatment on MDR tumors, treatments in DLD-1/DOX tumor-bearing mice and DLD-1 tumor-bearing mice were compared (Figure 28). Both groups of mice were divided into five test groups (n = 3 mice per group) that received saline (control) or DOX with or without NPs, and with or without NIR exposure (Table 4). When tumors developed to approximately 100 mm^3 in diameter, treatment was administered via intravenous tail injection (200 μl). The tumor volumes were measured in each group and plotted as a function of time, with the relative tumor volume (%) defined as $(V\text{-}V_0)\times 100/V_0$, where V_0 was the initial tumor volume.

DOX chemotherapy was delivered intravenously using either 10 mg/kg DOX solution or a 0.18 mg/kg solution of DOX inside DR4-DOX-PLGA-Au H-S NPs. In DLD-1 tumor-bearing mice, 10 mg/kg DOX significantly reduced the tumor volume compared to saline controls (Figure 28a). In contrast, the tumor volume increased more rapidly with DR4-DOX-PLGA-Au H-S NPs without NIR exposure than with DOX treatment alone. This difference was attributed to a slow release of DOX from PLGA NPs and the low concentration of DOX inside the NPs. On the other hand, when mice were treated with empty DR4-PLGA-Au H-S NPs (containing no DOX) and exposed to NIR light, the tumor growth was reduced to a rate similar to that of the group treated with the high-dose DOX solution. Finally, when DLD-1 tumor-bearing mice were treated with DR4-DOX-PLGA-Au H-S

NPs (0.18 mg/kg DOX) and NIR light, the tumor volume increased much more slowly than in the DOX injection group (Figure 28), demonstrating a synergistic effect of DOX combined with NIR exposure.

In DLD-1/DOX tumor-bearing mice, the tumor growth rate after DOX injection was similar to that of the saline injection, as expected, due to the drug resistance of DLD-1/DOX cells. However, when these mice were treated with DR4-DOX-PLGA-Au H-S NPs and exposed to NIR light, the tumor growth rate was considerably slower than that of DOX-treated mice (Figure 28b). This finding was in agreement with the *in vitro* cell viability test (Figure 16).

In fact, in DLD-1/DOX tumor-bearing mice (saline control), the tumor volume increased more slowly than in DLD-1 tumor-bearing mice (saline control). Therefore, I normalized the change in tumor volume with respect to the change observed in the control group ($\Delta V/\Delta V_{control}$), and the relative change was plotted as a function of time (Figure 29). When DLD-1/DOX tumor-bearing mice were treated with DR4-DOX-PLGA-Au H-S NPs and exposed to NIR light (1.82 W/cm^2) for 10 min at 24 h after NP injection, $\Delta V/\Delta V_{control}$ was much smaller than that of the groups treated with DOX only or DR4-PLGA-Au H-S NPs and NIR irradiation These findings suggest that the growth of DLD-1/DOX tumor cells was inhibited by targeted chemo-photothermal treatment, which was attributed to the prolonged retention of DOX in DLD-1/DOX cells. Moreover, the DR4-DOX-PLGA-Au H-S NPs used in the chemo-photothermal treatment contained only 0.18 mg/kg, which corresponds to 1.8% of the concentration used in DOX treatment; alone this low DOX treatment did not affect tumor growth rates, which were similar to those of

control-treated DLD-1/DOX tumor-bearing mice. These results suggest that the targeted chemo-photothermal treatment kills MDR tumors with minimal side effects.

Table 4. Summary of treatments in the therapeutic efficacy of MDR in cancer.

Group	Treatment[a]	DOX (mg/kg)	NIR light (W/cm^2)[b]
1	Saline	-	-
2	DOX solution	10	-
3	DR4-DOX-PLGA Au H-S NPs	0.18	-
4	DR4-PLGA Au H-S NPs	-	1.82
5	DR4-DOX-PLGA Au H-S NPs	0.18	1.82

[a]Administrated content was injected intravenously by tail vein in a volume 200 μl with a nanoparticle concentration of 1 mg/ml. [b]The tumor was exposed to NIR light (1.82 W/cm^2) for 10 min with a laser diode (λ = 808 nm) at 24 h post-injection.

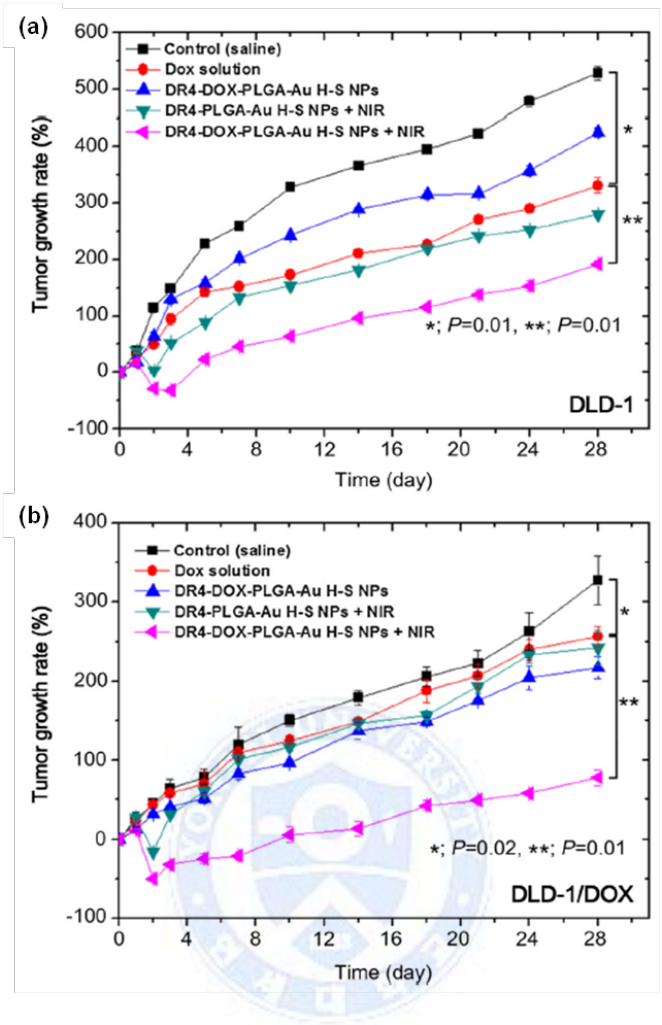

Figure 28. Relative change in tumor volume over time in (A) DLD-1 and (B) DLD-1/DOX tumor-bearing mice treated with saline (■), DOX solution (●), DR4-DOX-PLGA-Au H-S NPs (▲), DR4-PLGA-Au H-S NPs and NIR exposure (▼), or DR4-DOX-PLGA-Au H-S NPs and NIR exposure (◀). The tumor growth rate (%) was $(V\text{-}V_0) \times 100/V_0$, where V_0 is the initial tumor volume. Data represent mean ± SD (n = 3).

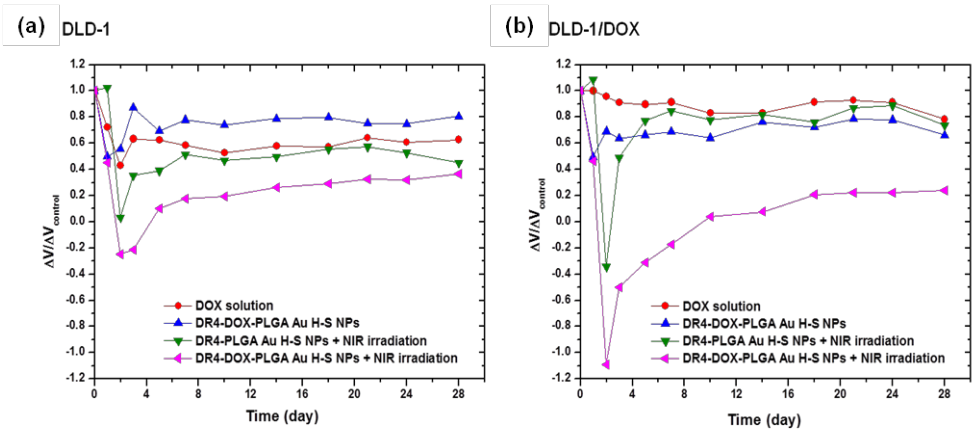

Figure 29. $\Delta V/\Delta V_0$ versus time for DLD-1 and DLD-1/DOX tumor-bearing mice treated differently. DOX solution (●), DR4-DOX-PLGA Au H-S NPs (▲). DR4-PLGA Au H-S NPs and NIR exposure (▼), or DR4-DOX-PLGA Au H-S NPs and NIR exposure (◀). ΔV_0 is the tumor volume change of the control group.

2.3.6. *In vivo* toxicity

DR4-DOX-PLGA Au H-S NPs were designed to target DR4-expressing cells. I histologically examined major organs from DLD-1/DOX tumor-bearing mice to determine whether any morphological changes occurred due to toxicity. The organs were collected 28 days after chemo-photothermal treatment. Tissues were fixed in 10 % buffered formalin-saline at 4 ^{o}C overnight. Then, tissues were embedded in paraffin blocks. Paraffin sections (5 μm thick) were mounted on glass slides for hematoxylin and eosin (H&E) staining.

No apparent tissue damage was observed as shown in Figure 30. I also measured body weight during the treatments (Figure 31). The DLD-1/DOX tumor-bearing mice treated with DOX solution lost weight over 28 days. However, the DLD-1/DOX tumor-bearing mice that received chemo-photothermal treatment did not exhibit weight loss. These results indicate that the targeted chemo-photothermal treatment did not result in significant toxicity.

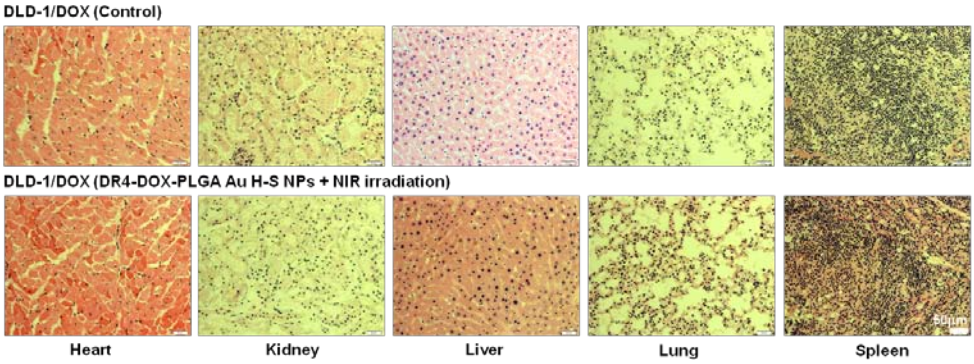

Figure 30. Histology of major organs (heart, kidney, liver, lung and spleen) obtained from DLD-1/DOX tumor-bearing mice. The tissues were collected at 28 days after intravenous injection of saline (upper panel) or DR4-DOX-PLGA-Au H-S NPs (lower panel) followed by NIR irradiation.

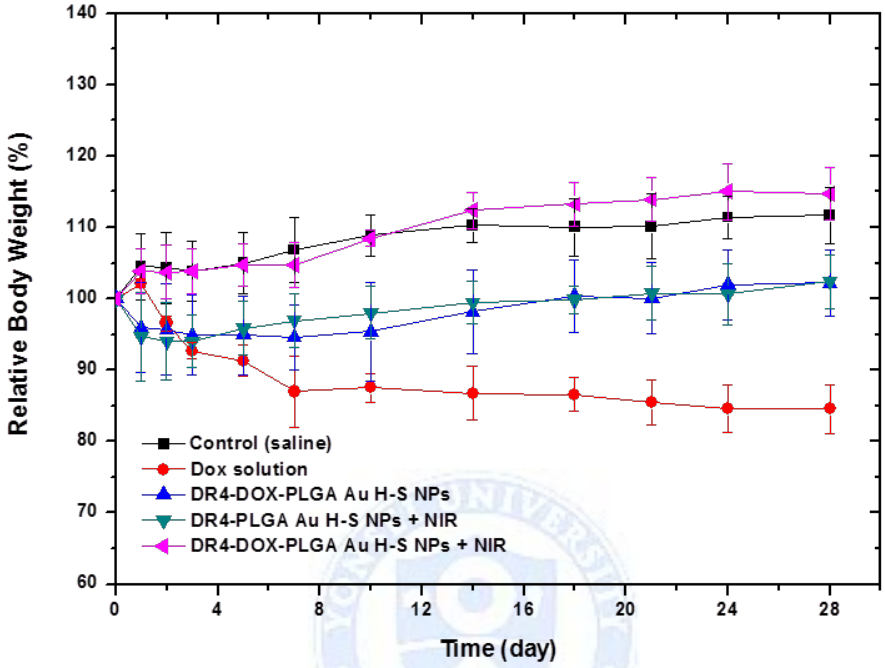

Figure 31. Relative body weight change versus time for DLD-1/DOX tumor-bearing mice treated with saline (■), DOX solution (●), DR4-DOX-PLGA Au H-S NPs (▲). DR4-PLGA Au H-S NPs and NIR exposure (▼), or DR4-DOX-PLGA Au H-S NPs and NIR exposure (◀).

2.4. Summary

I investigated the therapeutic effects of a targeted chemo-photothermal treatment with DR4-DOX-PLGA-Au H-S NPs and NIR irradiation in a DOX-resistant DLD-1 (DLD-1/DOX) cell line and DLD-1/DOX tumor-bearing mouse model. The targeted chemo-photothermal treatment decreased the tumor growth rate in the presence of even a small amount of DOX in DLD-1/DOX tumor bearing mice, likely due to the photothermally generated heat, reducing drug efflux from DLD-1/DOX cells and increasing intracellular drug accumulation.

The decrease in P-gp activity might be attributed to the decrease in ATPase activity caused by intracellularly-generated heat, although further studies are necessary to investigate how the chemo-photothermal treatment influences the activity of P-gp. These results demonstrate that this targeted chemo-photothermal treatment can achieve high therapeutic efficacy against MDR tumors with low toxicity.

Chapter 3.

In vivo chemo-photothermal therapy and imaging of rheumatoid arthritis

3.1. Introduction

3.1.1. Rheumatoid arthritis (RA)

Rheumatoid arthritis (RA) is progressive and disabling autoimmune disease which is characterized by bony erosion and synovial hyperplasia that affects the small diarthrodial joints of the hands and feet, leading to disability [75-78]. Three phases of progression of RA were known as; 1) initiation phase, due to non-specific inflammation, 2) amplification phase, owing to T cell activation, 3) chronic inflammatory phase with tissue injury, induced by cytokines, such as interleukin-1 (IL-1), interleukin-6 (IL-6), and tumor-necrosis factor (TNF)-α. In addition to an inflammation in the synovium, B cells, $CD4^+$ T cells, and macrophages infiltrate the synovium. Also, significant increase in fibroblast-like

and macrophage-like synoviocytes results in hyperplasia of the intimal lining. Degradative enzymes, such as serine proteases, aggrecanases, and metalloproteinases digest the extracellular matrix and eventually destroy the articular structures (Figure 32). RA incidence of the adult population worldwide is 0.5 ~ 1.0%.

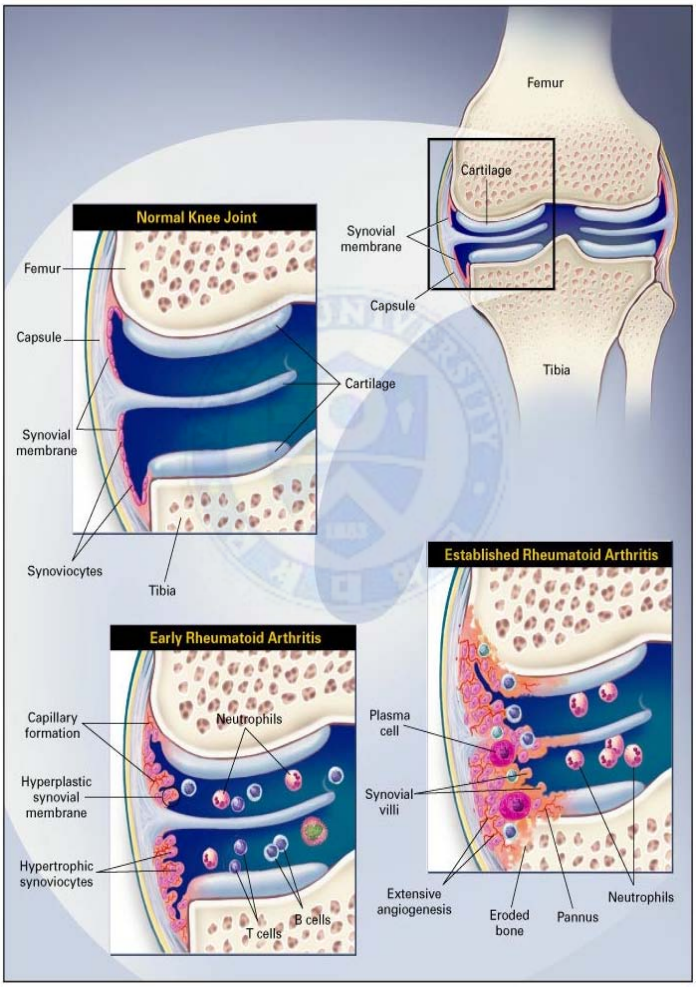

Figure 32. Illustration of progression in rheumatoid arthritis.

The cause of RA was not completely understood but cytokine networks were known as relation with pathogenesis of RA [76]. New molecular techniques were developed by the late 1980s, and cytokines in RA synovium and synovial fluid were measured. Rheumatoid synovium produces fibroblast and macrophage cytokines, such as TNF-α, IL-1, IL-6, IL-15, IL-18, granulocyte–macrophage colony-stimulating factor (GM-CSF), various chemokines, and many others. The role of cytokine networks in RA is that fibroblasts and macrophages produce cytokines each other to initiate RA (Figure 33). To treat RA, biological agents, such as anti-TNF-α antibody, were used to interrupt cytokine networks. The anti-TNF-α antibody can slow or prevent the progression of cartilage damage of RA owing to suppression of osteoclasts in joint [79].

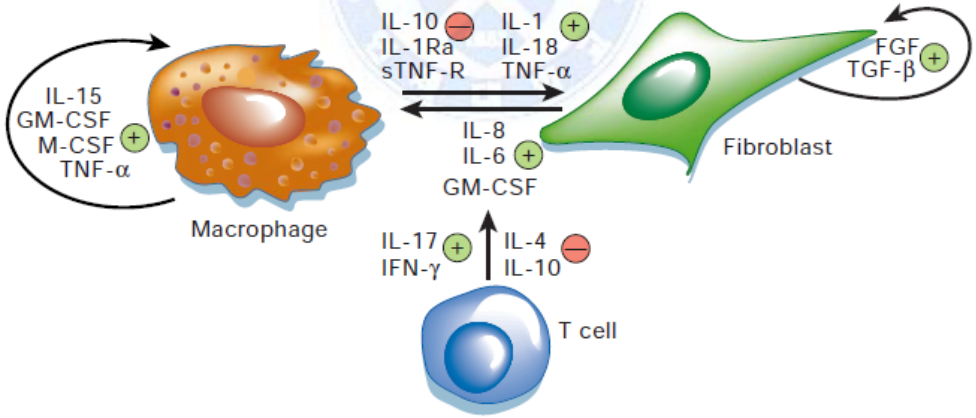

Figure 33. Cytokine networks in rheumatoid arthritis [76]. Proinflammatory cytokines (+) and anti-inflammatory proteins (–) are indicated.

A RANKL, the RANK (receptor activator of nuclear factor (NF)-κB) ligand, which is expressed by T cells and synoviocytes is most importantly related to bone erosions in RA [76]. The role of RANKL in RA has been studied in *in vivo* systems. For example, the RANKL which is activated by T cells, increase osteoclasts and deteriorate bone loss in rat adjuvant arthritis [80]. High levels of osteoprotegerin (OPG) and soluble-RANKL in RA are decreased after treatment of TNF inhibitors [81]. Moreover, bone erosion was diminished in RANKL-knockout mice [82].

Understanding the mechanisms of cytokine gene expression is important to treatment of RA. The RANKL regulates genes which contribute to inflammation in RA. These genes encompass IL-6, IL-8, TNF-α, cyclooxygenase-2 (COX-2), and inducible nitric oxidase synthase (iNOS). A mitogen-activated protein (MAP) kinases are also important regulators of cytokine and could be targeted in RA. These kinases, including p38 mitogen-activated protein kinase, extracellular signal-regulated kinase (ERK), and c-Jun N-terminal kinase (JNK) are expressed in synovial tissue of RA [83]. Pre-clinical studies have shown that inhibitor of p38 mitogen-activated protein kinase was used as therapeutic agents of RA in animal model [84].

3.1.2. Disease-modifying anti-rheumatic drugs (DMARDs)

Disease-modifying anti-rheumatic drugs (DMARDs) are the main strategy for the treatment of RA, and methotrexate (MTX) is the most widely used DMARD for the treatment of RA (Figure 34) [85]. MTX has a structural analogue of folic acid which can competitively inhibit the binding of dihydrofolic acid to the enzyme dihydrofolate reductase, eventually inhibits DNA formation and cell proliferation. MTX can be prescribed alone or with other DMARDs or biologic agents for combination therapy. However, despite its good therapeutic efficacy, the long-term administration of MTX may induce serious systemic complications, including infection, hepatitis, and bone marrow suppression [86-87].

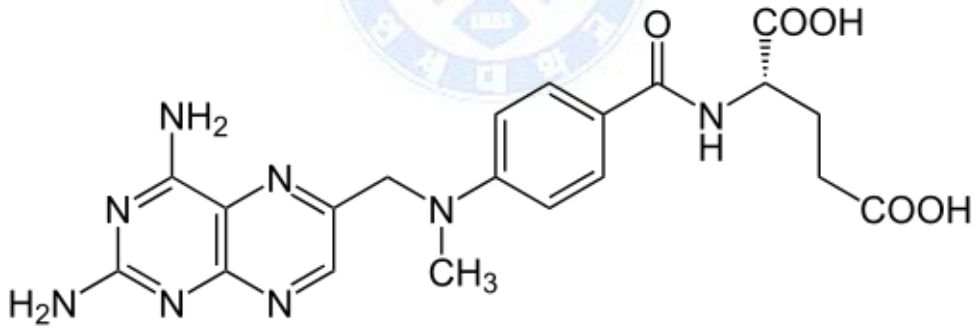

Figure 34. Chemical structure of methotrexate (MTX).

From a clinical point of view, increasing the dose of MTX in RA patients, who have several refractory joints or MTX dose-related side effects, or continuiting MTX in patients who have systemic disease, such as interstitial lung disease, viral hepatitis, or bone marrow dysfunction, may provoke more unwanted adverse effects. Therefore, the novel delivery systems to maintain a high concentration of MTX within the joint spaces, which is the main area of inflammation, by administration of small dosage of drugs and to reduce side effects in accordance with systemic administration of MTX would be an attractive and effective tool for RA treatment.

3.2. Experimental details

3.2.1. Fabrication of RGD-MTX Au plasmonic NPs and MTX-Au/Fe/Au plasmonic NPs

MTX-PLGA (Poly(lactic-*co*-glycolic acid) (PLGA; L:G molar ratio=50:50; MW=20,000)) NPs were synthesized using the solvent evaporation method [53-58]. Briefly, PLGA (200 mg) and MTX (6 mg) were dissolved in dichloroethane (20 ml), and this organic solution (oil phase) was added slowly drop-wise with distilled water (200 ml) containing Pluronic F-127 (200 mg) as a stabilizer under magnetic stirring. After mixing the oil and water phase, the mixture was emulsified by ultrasonication for 1 hr (400 W), followed by evaporation of organic solvent (dichloroethane) with stirring for 1 day. Then, the MTX-PLGA NPs were collected by centrifugation, and re-dispersed in 5 ml PBS by sonication. After that, 15-nm-thick Au film was deposited onto an MTX-PLGA nanoparticle monolayer prepared on a Si substrate using a thermal evaporator. After depositing the Au film, Au-deposited MTX-PLGA nanoparticles were released into 1 wt% SH-PEG-COOH solution from the substrate by sonication and collected by centrifugation. The collected carboxylic acid-terminated MTX-PLGA-Au nanoparticles (74.6 μM) and EDC (746.7 μM) were dissolved in 25 ml of 0.2 M phosphate buffer (pH 6.0) and stirred at room temperature. After 30 min, cyclic RGD (74.6 μM) in 3 ml of

distilled water was added and the pH value of the reaction mixture adjusted to 8.0 by adding 0.5 M NaOH. The reaction mixture was then left at room temperature for the RGD peptides to bind covalently to the COOH group of the SH-PEG-COOH chains immobilized on the surface of the Au half-shells. After 12 h, RGD-MTX-PLGA-Au nanoparticles were collected by centrifugation for 30 min at 100,000 rpm; the supernatant containing un-reacted cyclic RGD was discarded. The resulting RGD-MTX-PLGA-Au nanoparticles were characterized using an ^{1}H-NMR spectrometer (300 MHz, DMSO-d_6, 25 ^{o}C, TMS, Varian Gemini-300 spectrometer) with δ values of 8.1 ~ 8.6 (-NH(NH_2)=NH of cyclic RGD), 5.2 (m, CH of PLGA), 3.6 (s, CH_2 of PEG), and 1.5 (d, CH_3 of PLGA).

In the case of MTX-Au/Fe/Au plasmonic NPs, the electron-beam evaporator was used to deposit the films of 10-nm-thick Au/ 5-nm-thick Fe/ 10-nm-thick Au onto MTX-PLGA NPs monolayer, which was prepared by spin-coating aqueous suspension of MTX-PLGA NPs on a Si substrate. The Si substrate was immersed in SH-PEG-COOH (1 wt%) solution followed by sonication. After that, the COOH-terminated MTX-Au/Fe/Au plasmonic NPs were obtained by centrifugation. For targeted delivery to the inflammation region, the cyRGD peptides (3 mg) were conjugated on the outer Au half-shell surface of MTX-Au/Fe/Au plasmonic NPs with conventional EDC (4 mg) /NHS (4 mg) coupling reaction in 9 ml of PBS at 4 °C for 1 day. After the reaction, MTX-Au/Fe/Au plasmonic NPs were collected by centrifugation, and were re-dispersed in 1.5 ml of PBS. These cyRGD peptides conjugated on MTX-Au/Fe/Au plasmonic NPs were analyzed using a ^{1}H-NMR spectrometer (Varian Gemini-300, DMSO-d_6) with

characteristic δ values of 1.5 (*d*, -CH_3 of PLGA), 3.6 (*s*, -CH_2- of PEG), 5.2 (*m*, ≡CH of PLGA), 8.1 - 8.6 (-NH(NH_2)=NH of cyRGD). In the FT-IR spectrum (Bruker Vertex 70), there were characteristic peaks at 1,700 cm^{-1} (C=O stretch), 3,480 cm^{-1} (-N-H stretch), and 1,650 cm^{-1} (-N-H bend). The cyRGD peptides contents in the MTX-Au/Fe/Au plasmonic NPs were quantified by high pressure liquid chromatography (HPLC) using a C_{18} column (water Noca-Pak C_{18}, 3.9 × 300 mm, 4 μm).

Schematic diagram of fabrication of RGD-MTX Au plasmonic NPs and MTX-Au/Fe/Au plasmonic NPs was shown in Figure 35.

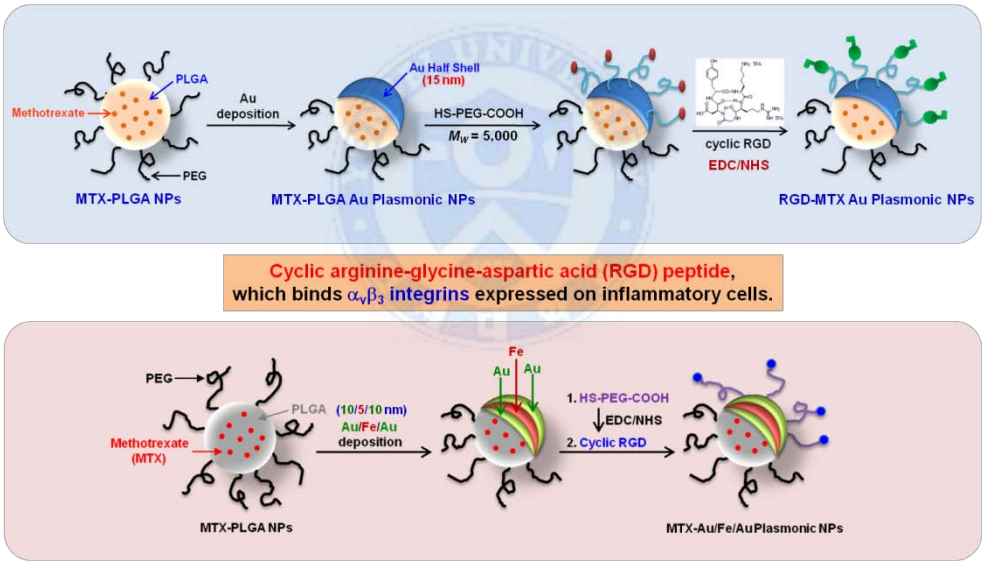

Figure 35. Preparation of RGD-MTX Au plasmonic NPs (upper panel) and MTX-Au/Fe/Au plasmonic NPs (lower panel).

3.2.2. Preparation and culture of fibroblast-like synoviocyte (FLS) cells

Synovial tissues were obtained from 3 patients with RA who underwent knee joint replacement surgery at Severance Hospital, Yonsei University College of Medicine, Seoul, Korea. All patients satisfied the 1987 revised American College of Rheumatology (ACR) classification criteria for rheumatoid arthritis. FLS cells were isolated and cultured as described previously [88]. Cells obtained from passages at 4 to 8 were used in these experiments. FLSs were seeded into 12-well plates at a density of 1.5×10^5 cells/well in Dulbecco's modified Eagle's medium (DMEM) supplemented with 10% fetal bovine serum (FBS; GibcoBRL, GrandIsland, NY), 2mM L-glutamine, 100 units/ml of penicillin, and 100 g/ml of streptomycin. TNF-α (10 ng/ml) was used to induce inflammation in FLS cells. FLS cells were incubated at 37 °C.

To quantify the apoptotic cells of cultured FLS, fluorescein isothiocyanate (FITC) Annexin V Apoptosis Detection kit (BD biosciences, San Diego, CA) was used according to the manufacturer's protocol. Cells were treated with MTX (30 μM), MTX (0.13 μM, NPs dose), and MTX-PLGA Au plasmonic NPs with NIR irradiation and incubated at 37 °C for 48 and 72 h. NIR irradiation was done 24 h after treatment with the power of 0.73 W/cm^2 for 10 minutes. After NIR irradiation, the temperature increases up to 42 °C. Treated cells were harvested by centrifugation, and washed in cold PBS. Annexin V-FITC and propidium iodide (PI) were added to a 400 μl aliquot of the cells. After 15-min incubation in the dark

at room temperature, stained cells were immediately analyzed by a flow cytometry (FACS calibur, BD). A minimum of 10,000 events were collected and analyzed using FACS Comp^{TM} software (BD). Annexin V-positive and PI-negative cells were defined as early apoptotic cells, while Annexin V-positive and PI-positive cells were defined as late apoptotic cells [89].

3.2.3. Induction and treatment of collagen induced arthritis

All procedures involving animals were performed in accordance with the Laboratory Animals Welfare Act, the Guide for the Care and Use of Laboratory Animals, and the Guidelines and Policies for Rodent Experiments provided by the Institutional Animal Care and Use Committee of Yonsei University Health System, Seoul, Korea. Male DBA/1J mice (8 weeks old; Central Lab Animal, Inc., Seoul, Korea) were injected intradermally at the tail base with 200 μg bovine type II collagen (CII; Chondrex, Redmond, WA, USA) emulsified in Freund's complete adjuvant (1:1, *v*/*v*; Chondrex) containing 200 μg *Mycobacterium tuberculosis* H37Ra (Chondrex). Two weeks later, the mice were given intradermal booster injections of 100 μg CII in incomplete Freund's adjuvant (1:1, *v*/*v*; Chondrex) [90]. Mice were monitored twice weekly for signs of arthritis onset based on paw swelling and clinical arthritis scoring on a scale of 0 – 4. The clinical index is the sum of the clinical scores for four paws (maximum scores = 16). The evaluated paws were scored from 0 to 4 according to the following scale: 0= no evidence of erythema and swelling, 1 = erythema and mild swelling, 2 = erythema and mild

swelling extending from the ankle to the tarsals, 3 = erythema and moderate swelling extending from the ankle to metatarsal joints and 4 = erythema and severe swelling encompassing the ankle, foot and digits or ankylosis of the limb (Figure 36). Each paw was graded by two independent observers and the grades were summed, yielding a maximum possible arthritis score of 16 for each animal. Upon arthritis development (arthritis score of 8 - 10), mice were randomly arranged to each treatment group (n = 3 or n = 5) at 3 weeks after the second CII booster injection.

Figure 36. Clinical score of CIA mouse [images from http://hookelabs.com].

In the RGD-MTX Au plasmonic NPs experiment, saline (group 1) and RGD-MTX-PLGA-Au nanoparticles (groups 3 and 4), and MTX-PLGA-Au nanoparticles (group 5) were intravenously administered to the mice, and groups 4 and 5 were exposed to 1.59 W/cm^2 NIR light for 10 min at 1 day after intravenous injection of nanoparticles. MTX solution (group 2) with 35 mg/kg was injected intraperitoneally once weekly till sacrifice. After that, the mice were observed twice weekly during 28 days (n = 5 mice each group, Table 5).

Table 5. Summary of treatments applied to CIA mice for comparative study of therapeutic efficacy for RGD-MTX Au plasmonic NPs experiment.

Group (n = 5)	Administered content[a]	Dosage of MTX (mg/kg)	NIR light (W/cm^2)[b]
Group 1	Saline	-	-
Group 2	MTX solution	35 × 4 times	-
Group 3	RGD-MTX-PLGA-Au nanoparticles	0.15	-
Group 4	RGD-MTX-PLGA-Au nanoparticles	0.15	1.59
Group 5	MTX-PLGA-Au nanoparticles	0.15	1.59

[a] Administrated content was injected intravenously by tail vein in a volume 150 μl with a nanoparticle concentration of 1 mg/ml.
[b] The arthritis was exposed to NIR light for 10 min with a laser diode (λ = 808 nm) at 24 h post-injection.

In the MTX-Au/Fe/Au plasmonic NPs experiment, Saline (G1) or MTX-Au/Fe/Au plasmonic NPs (from G3 to G7) were administered *via* intravenous tail injection. G4, G6, and G7 were also exposed to 1.3 W/cm^2 NIR light for 10 min at 1 day after NP injection. G7 received a second NIR exposure 7 days after the first. MTX solution (G2) with 35 mg/kg was injected intraperitoneally twice weekly till sacrifice. An external magnetic field was applied to G5, G6 and G7. After that, the mice were observed twice weekly during 31 days. (n = 3 mice each group, Table 6).

Table 6. Summary of the treatments applied to CIA mice to compare therapeutic efficacy for MTX-Au/Fe/Au plasmonic NPs experiment.

Group (n = 3)	Injected content[a]	Dosage of MTX (mg/kg)	NIR light (W/cm^2)[b]	Magnetic field (T)[c]
1	Saline	-	-	-
2	MTX solution	35 × 9 times	-	-
3	MTX-Au/Fe/Au plasmonic NPs	0.15	-	-
4	MTX-Au/Fe/Au plasmonic NPs	0.15	1.3	-
5	MTX-Au/Fe/Au plasmonic NPs	0.15	-	2.3
6	MTX-Au/Fe/Au plasmonic NPs	0.15	1.3	2.3
7	MTX-Au/Fe/Au plasmonic NPs	0.15	1.3 × 2 times	2.3

[a] Administration was performed by intravenous tail vein injection of 150 μl of 1 mg/ml nanoparticle concentration.
[b] The arthritis joint was exposed to NIR light with a laser diode (λ = 808 nm) for 10 min at 24 h post-injection. In group 7, this was repeated 7 days later.
[c] The external magnetic field was applied for up to 31 days starting immediately after injection.

3.3. Results and discussion

3.3.1. Characterization of RGD-MTX Au plasmonic NPs and MTX-Au/Fe/Au plasmonic NPs

For targeted delivery, cyclic RGD peptide, which binds $\alpha_v\beta_3$ integrins expressed on angiogenic vascular endothelial cells at sites of inflammation [91], was conjugated on the Au surface (RGD-MTX Au plasmonic NPs or MTX-Au/Fe/Au plasmonic NPs). The visible/NIR absorption spectrum of RGD-MTX Au plasmonic NPs exhibited a pronounced peak at approximately 810 nm due to Au half-shells.

In the case of MTX-Au/Fe/Au plasmonic NPs, the NPs with 10-nm Au/ 5-nm Fe/ 10-nm Au half-shell thickness exhibited the most pronounced absorption peak at ~800 nm. NPs lacking the inner or outer Au layer showed absorption peaks at a wavelength longer than the biological optical window of 664 - 934 nm. Thus, MTX-Au/Fe/Au plasmonic NPs were prepared with layers of 10-nm Au/5-nm Fe/10-nm Au. Finally, the cyRGD peptide targeting moiety was conjugated to SH-PEG-COOH modified on the outer Au surface.

The size and zeta-potential of prepared nanoparticles dispersed in an aqueous medium were measured at 25 °C by using dynamic light scattering (DLS; Zetasizer Nano ZS, Malvern Instruments Ltd.). Using dynamic light scattering, RGD-MTX Au plasmonic NPs have an average diameter of ~115 nm and the estimated MTX

loading content was about 2.6 wt%. The outer Au surface of the RGD-MTX Au plasmonic NPs was found to contain 41.8 μg immobilized RGD peptides/mg of NPs. In the case of MTX-Au/Fe/Au plasmonic NPs, similar results were obtained (average diameter : 135 nm, MTX loading content : 2.1 wt%, RGD peptides/mg of NPs : 19 μg) (Figure 37).

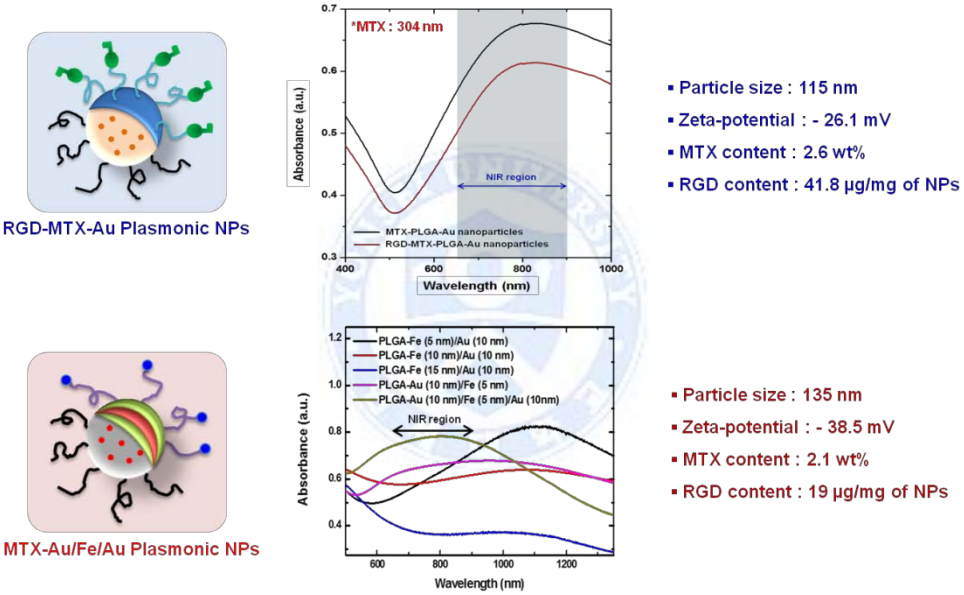

Figure 37. Visible/NIR absorption spectrum and characterization of RGD-MTX Au plasmonic NPs (top) or MTX-Au/Fe/Au plasmonic NPs (bottom).

When a 0.5 mg/ml solution of MTX-Au/Fe/Au plasmonic NPs was irradiated by NIR light (λ = 808 nm, 0.62 W/cm^2), the temperature increased to 55 °C within 10 min (Figure 38), which is comparable to the reported results for Au nanorods [92] or nanoshells [93]. These results indicated that these MTX-Au/Fe/Au plasmonic NPs can be used for photothermal treatment and *in vivo* NIR absorbance imaging.

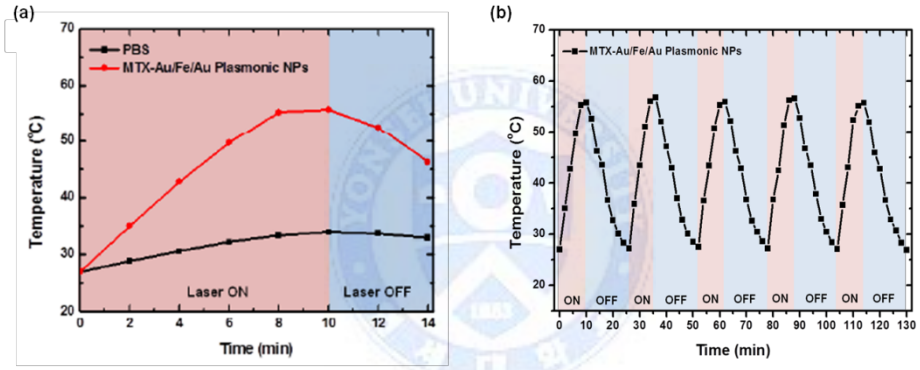

Figure 38. (a) Temperature versus time for the MTX-Au/Fe/Au plasmonic NPs and PBS with NIR light irradiation for 10 min. (b) The change of temperature increase of MTX-Au/Fe/Au plasmonic NPs for five NIR laser diode on/off cycles (λ = 808 nm, 0.62 W/cm^2, beam diameter $d \approx 3.5$ cm).

The elemental mapping of an individual MTX-Au/Fe/Au plasmonic NP using TEM was shown is Figure 39a. The magnetic properties of MTX-Au/Fe/Au plasmonic NPs were also characterized by magnetization-magnetic field curve measurement (vibrating sample magnetometer; VSM, Model 7407, Lakeshore). No hysteresis was observed, indicating that these NPs are superparamagnetic (Figure 39b). To determine whether the NPs could be used as contrast for MR imaging, the spin-spin relaxation time (T_2) and T_2-weighted spin-echo MR images were measured at 1.5 T for NP solutions of various concentrations (Figure 39c). Increasing NP concentrations were associated with increasing $1/T_2$, indicating that MTX-Au/Fe/Au plasmonic NPs can be used as MRI contrast agents as well as NIR absorbance imaging agents.

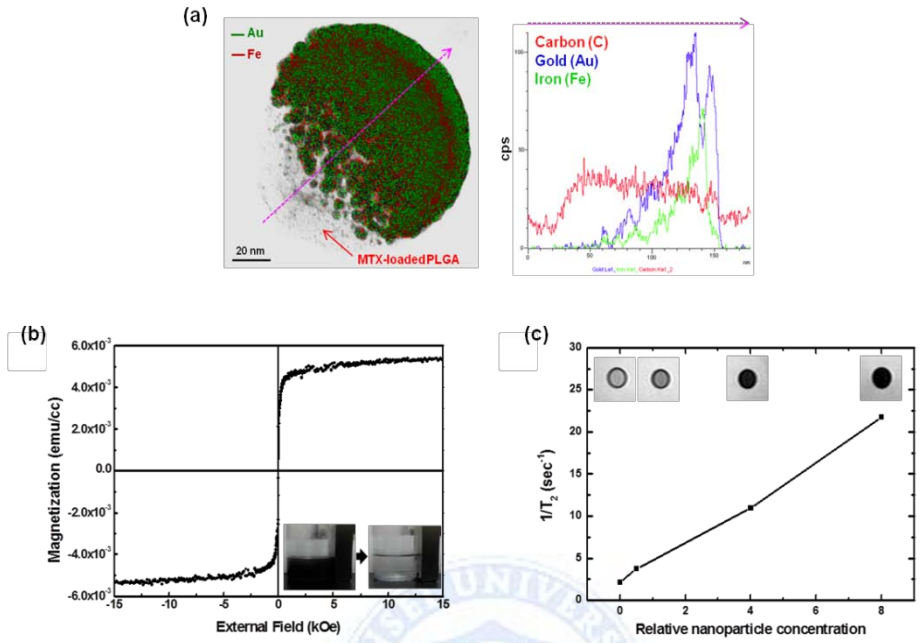

Figure 39. (a) Elemental mapping of an individual MTX-Au/Fe/Au plasmonic NP using TEM. (b) Magnetization (M–H) curves measured for MTX-Au/Fe/Au plasmonic NPs. When the external magnetic field applied, the MTX-Au/Fe/Au plasmonic NPs moved toward magnet within 15 min (inset). (c) Magnetic resonance data of $1/T_2$ versus relative NP concentration. The inset shows T_2-weighted images for different NP concentrations.

To test the stability of MTX-Au/Fe/Au plasmonic NPs in *in vitro* condition, the stability of NPs in 10% serum at 37 °C was measured by measuring the absorbance of NPs solution at 800 nm as a function of time. The absorbance was nearly unchanged during 24 h in 10% serum at 37 °C and did not exhibit any aggregation, indicating that the NPs were stable in *in vitro* condition (Figure 40).

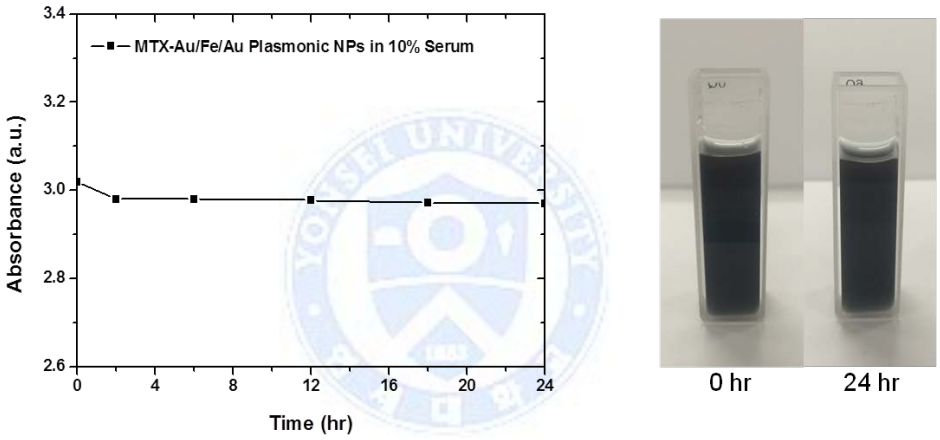

Figure 40. The stability of MTX-Au/Fe/Au plasmonic NPs in 10% serum at 37 °C.

Biodegradable PLGA nanoparticles degrade more rapidly with increasing temperature [94]. The RGD-MTX Au plasmonic NPs (10 mg) or MTX-Au/Fe/Au plasmonic NPs (10 mg) were loaded into a dialysis tube (1 kDa cut-off membrane, Tube-O-DIALYZER^{TM}, G-Biosciences, USA) followed by immersion in 10 ml PBS with mild constant shaking. During the dialysis, the solution volume was maintained constantly by replacing with fresh PBS after each sampling. The release experiments for RGD-MTX Au plasmonic NPs were performed with and without NIR irradiation (Unique mode 30 k/400/20 (808 ± 3) nm, Jenoptik Co., Germany) of 0.38 or 0.53 W/cm^2 for 10 min at the initial time of the experiment at 37 °C.

The release experiments for MTX-Au/Fe/Au plasmonic NPs were also conducted with and without two exposures to NIR light of 0.62 W/cm^2 for 10 min, and 7 days at the start of the experiment at 37 °C. The amount of released MTX from the NPs was measured by ultraviolet-visible/NIR spectrophotometer at 304 nm. The measurements were performed three times for each sample.

In order to study the effect of 10-min NIR irradiation on the MTX release rate, the release profiles at 37 °C with and without 10-min NIR irradiation were measured (Figure 41a). The release rate of MTX from nanoparticles was nearly constant without NIR irradiation, resulting in a linear release profile. However, 10 min NIR irradiation induced a burst release of MTX for 12 h, after which the release rate was reduced. These results indicate that the MTX release rate from nanoparticles can be controlled by NIR light.

After measuring MTX release, the nanoparticle morphology was examined

using a transmission electron microscope (TEM) (Figure 41b). In the absence of NIR light, PLGA nanoparticles were not degraded completely and the PLGA that was not covered with Au was partly seen. In contrast, when nanoparticles were irradiated with NIR light, PLGA nanoparticles were mostly degraded and only Au half-shell nanoparticles were clearly observed, supporting photothermally controlled drug release.

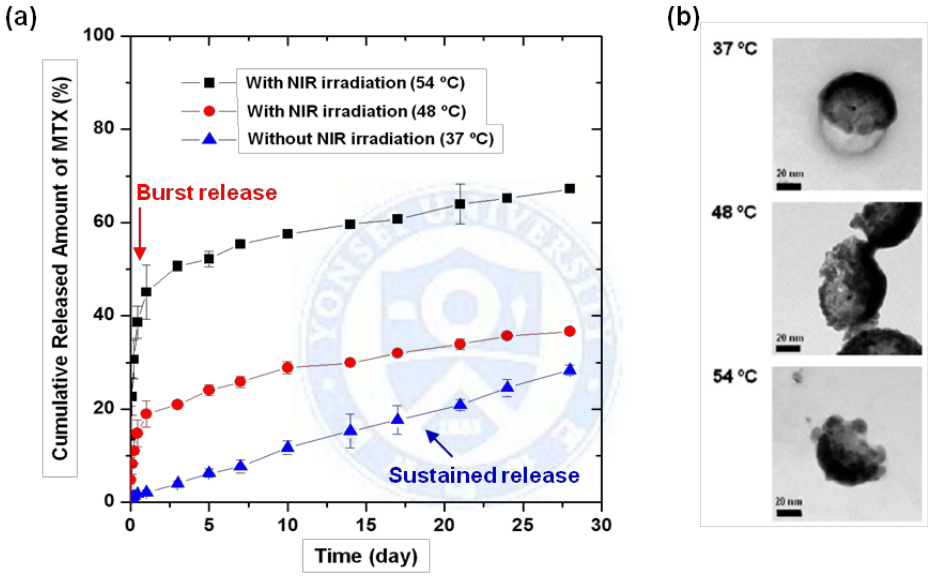

Figure 41. (a) Profiles of MTX release from RGD-MTX Au plasmonic NPs with and without NIR irradiation of 0.38 (48 °C) or 0.53 (54 °C) W/cm^2 for 10 min at the initial time. Data represent mean values for n = 3, and the error bars represent standard deviation of the means. (b) TEM images of RGD-MTX Au plasmonic NPs measured after MTX release experiments without (top), or with NIR irradiation of 0.38 (48 °C, middle) or 0.53 (54 °C, bottom) W/cm^2 for 10 min at the initial time.

Drug release profiles were also measured for the MTX-Au/Fe/Au plasmonic NP. Figure 42 shows the drug release profiles from MTX-Au/Fe/Au plasmonic NPs with two exposures to NIR light. The first 10-min NIR irradiation caused a 24-h burst release of MTX, followed by a slow release. The second NIR irradiation at 7 days induced another burst release of MTX. These results demonstrated the ability to control the MTX release from MTX-Au/Fe/Au plasmonic NPs using NIR light.

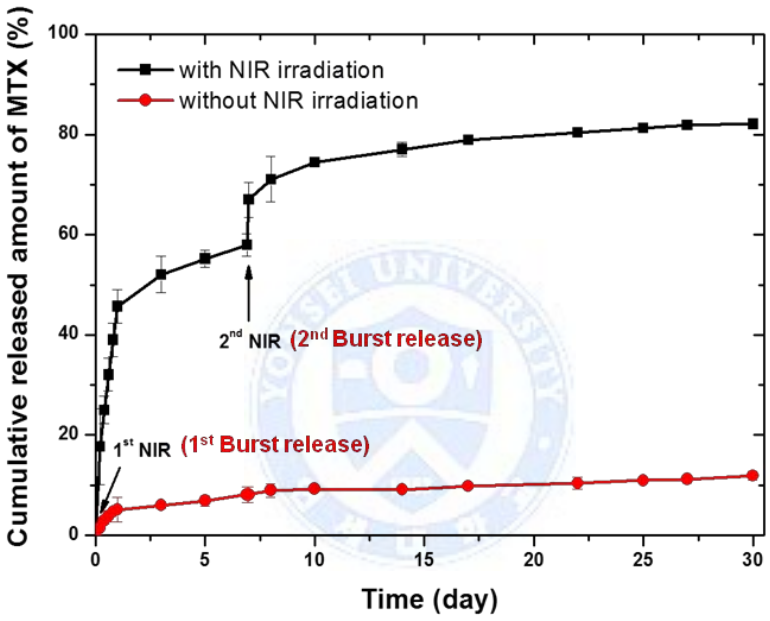

Figure 42. Profiles of MTX release from MTX-Au/Fe/Au plasmonic NPs with and without NIR irradiation of 0.62 W/cm^2 for 10 min at initial time and the second NIR was irradiated at 7 days. The temperature increased up to 45 °C after NIR irradiation. Data represent mean values for n = 3, and the error bars represent standard deviation of the means.

3.3.2. *In vitro* apoptosis analysis

To study the anti-arthritis effect of MTX-Au plasmonic NPs with NIR irradiation *in vitro*, FLS cells were cultured with various treatments and cells on apoptotic death were evaluated. The percentage of apoptotic cells from several treatments for 48 h and 72 h was evaluated using flow cytometry. After treatment of MTX solution of 30 μM, the number of apoptotic cells was significantly increased compared to control at 72 h. However, in the case of MTX solution of 0.13 μM (NPs dose; 1/230 dose of 30 uM MTX solution treatment), the percentage of apoptotic cells was decreased compared to MTX solution of 30 μM at 72 h. The photothermal treatment using MTX-Au plasmonic NPs with NIR irradiation (temperature of culture media increases up to 42 ℃), the number of apoptotic cells was similar with that of 30 μM MTX solution-treated group at 72 h (Figure 43). Therefore, the MTX-Au plasmonic NPs containing a much smaller dose of MTX (1/230 of MTX solution) combined with photothermal treatment showed similar apoptosis efficacy of FLS cells that of conventional treatment of MTX solution (30 μM), which indicated that the dose-related MTX side effects could be minimized in the treatment of RA.

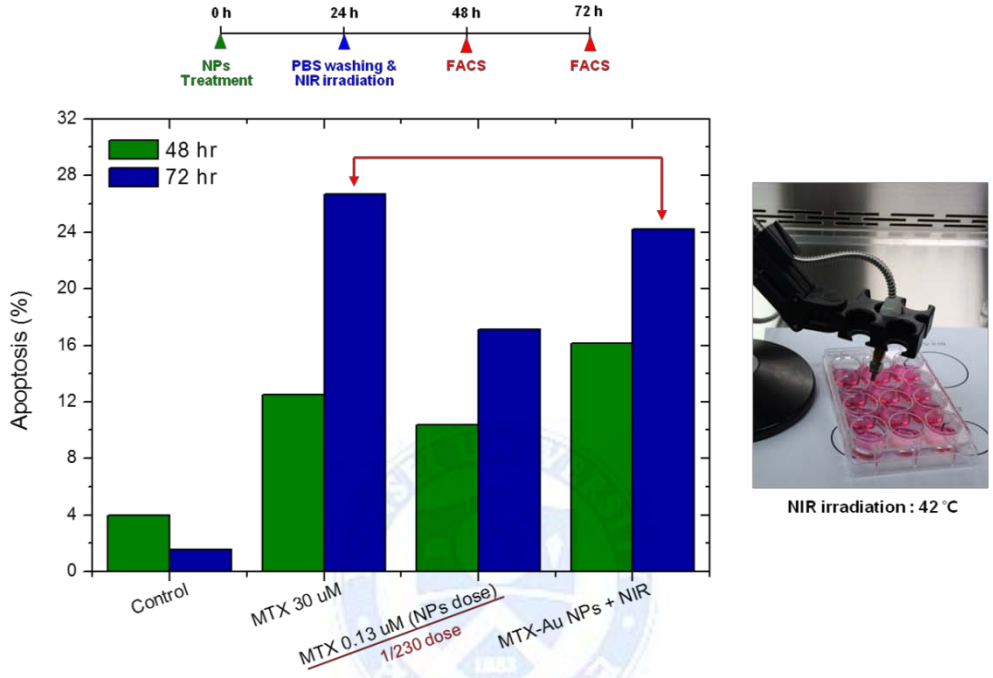

Figure 43. Apoptosis assay results of FLS cells with various treatments.

3.3.3. *In vivo targeting and retention efficacy*

To evaluate the *in vivo* targeting efficacy, Au plasmonic NPs or Au/Fe/Au plasmonic NPs (150 μl, without MTX, 1 mg/ml in PBS) were injected intravenously to the CIA mice. The CIA mice were anesthetized by intraperitoneal injection of a Zoletil50/Rompun mixture (*v/v* = 3), and anesthesia was sustained during the experiments. NIR absorbance images were obtained using the eXplore Optix System (Advanced Research Technologies Inc., Montreal, Canada). The absorbance at 710 ~ 750 nm was detected through a fast photomultiplier tube (Hammamatsu, Japan) and a time-correlated single photon counting system (Becker and Hickl GmbH, Berlin, Germany). The total NIR absorbance intensities at the region-of-interest (ROI) in the inflamed paws of CIA mice were calculated using the eXplore Optix System software.

CIA mice treated with MTX-PLGA-Au or RGD-MTX-PLGA-Au nanoparticles exhibited a change in *in vivo* absorbance intensity over time due to localization of nanoparticles in the inflamed paws (Figure 44a). The number of pixels with absorbance intensity $\geq 3.82 \times 10^3$ a.u. increased up to 24 h after intravenous administration, and then decreased, possibly due to a slow release of nanoparticles by leaky angiogenic vessels (Figure 44b) [61]. To quantify the accumulation of nanoparticles in the inflamed joints, the mass of Au in the inflamed paws 24 and 72 h post-injection was measured using an inductively coupled plasma mass spectrometer (ICP-MS) (Figure 44b). In two paws of the CIA

mice treated with RGD-MTX-PLGA-Au nanoparticles, 0.23 μg of Au was found at 24 h, corresponding to 0.9% of the injected nanoparticles, whereas 0.16 μg of Au (0.7%) was measured in the inflamed paws treated with MTX-PLGA-Au nanoparticles. These results indicate that nanoparticles were more effectively delivered to the inflamed region *via* active targeting compared to passive targeting.

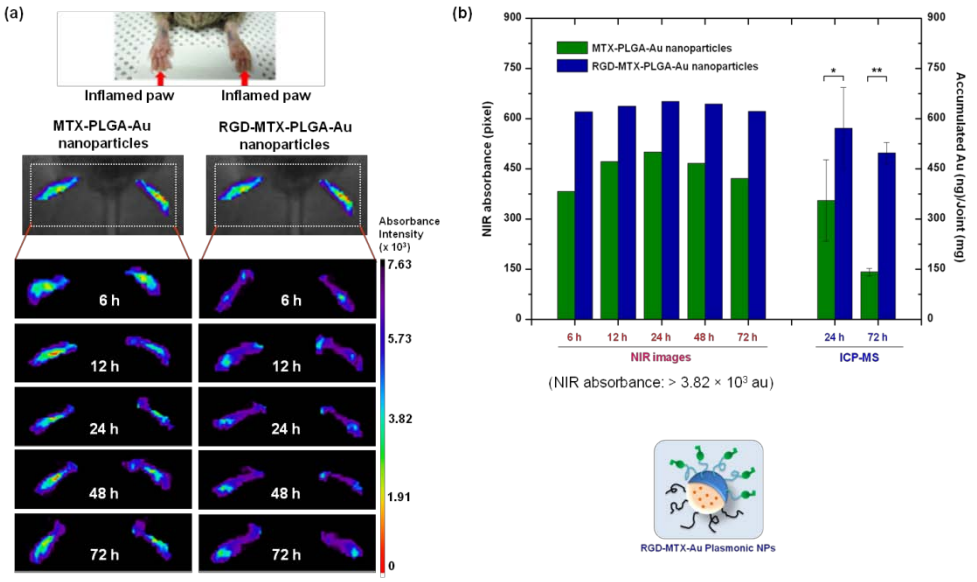

Figure 44. (a) Time-lapse *in vivo* NIR absorbance images of inflamed paws in CIA mice injected intravenously with MTX-PLGA-Au nanoparticles (150 μl, 1 mg/ml dispersed in PBS, left column) or RGD-MTX-PLGA-Au nanoparticles (150 μl, 1 mg/ml dispersed in PBS, right column). (b) The number of pixels in which the absorbance intensity was above 3.82×10^3 a.u. as a function of time for nanoparticle-treated mice (left axis), and the amount of Au accumulated in the inflamed paws extracted from the nanoparticle-treated mice 24 and 72 h after intravenous injection (right axis). The mass of Au was measured using ICP-MS. Data represent mean values for $n = 3$, and the error bars represent standard deviation of the means.

To evaluate the *in vivo* retention efficacy, these CIA mice were injected intravenously with 150 μl of Au/Fe/Au plasmonic NPs (1 mg/ml stock solution, without MTX), and then placed in a mouse cage with or without the Nd-Fe-B magnet of 2.3 T (Figure 45). The injected Au/Fe/Au plasmonic NPs were monitored by measuring time-lapse *in vivo* NIR images using an eXplore Optix System (Figure 46a). Mice in the cage without the magnet (control group) showed increased absorbance intensity in the inflamed paws after NP injection, which slowly decreased over time, indicating NP delivery to and accumulation in the inflamed paws. In contrast, mice in the cage with the magnet exhibited continuously increasing absorbance intensity for up to 7 days, probably due to magnetic targeting and enhanced retention of the NPs (Figure 46a). To quantitatively compare NP magnetic targeting and retention with and without magnetic field application, an inductively coupled plasma mass spectrometer (ICP-MS) was used to measure the Au accumulated in the inflamed joints (Figure 46b). At 7 days after NP injection, the Au mass in the inflamed joints was ~ 0.934 μg (1.7% of the injected NPs) for mice in the cage without the magnet, and ~ 1.351 μg (2.4% of the injected NPs) for mice in the cage with the magnet. These findings support that magnetic field application enhanced the magnetic targeting and retention of Au/Fe/Au plasmonic NPs.

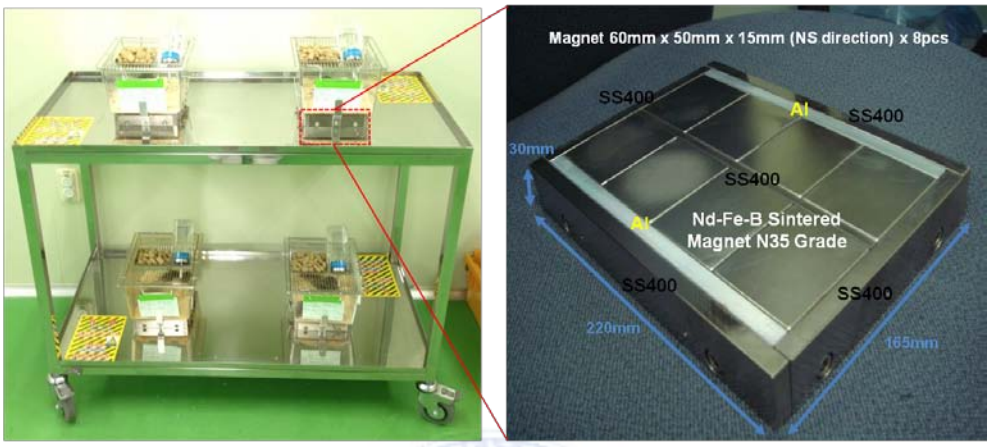

Figure 45. Photo of magnet cart of CIA mice for the application of magnetic field during experiments. The magnet was placed under CIA mice cage.

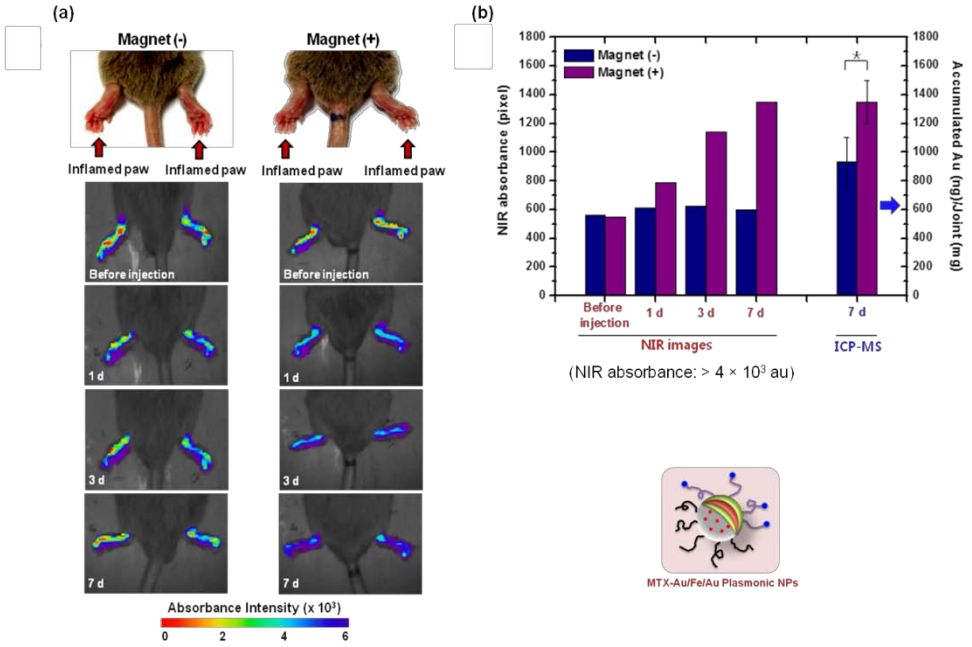

Figure 46. (a) Time-lapse *in vivo* NIR absorbance images of inflamed paws of CIA mice injected intravenously with Au/Fe/Au plasmonic NPs (150 μl, 1 mg/ml in PBS) and caged with (+) or without (-) a magnet. (b) Number of pixels in which the absorbance intensity was above 4×10^3 arbitrary unit as a function of time for Au/Fe/Au plasmonic NP-treated mice caged with (+) or without (-) a magnet (left axis). The right axis shows the amount of Au accumulated in the inflamed joints extracted from the Au/Fe/Au plasmonic NP-treated mice at 7 days after intravenous injection with (+) or without (-) a magnet. The Au mass was measured using ICP-MS. Error bars represent standard deviation ($n = 3$, $^*p < 0.05$).

I also analyzed MR images of the CIA mice treated with Au/Fe/Au plasmonic NPs and cage with or without the magnet (Figure 47). T_2-weighted MR images were collected using a 9.4-T 20-cm-bore MRI system (Bruker Biospin, Ettlingen, Germany) equipped with a rat brain surface coil (4 ch). Animal imaging was performed under inhalational anesthesia with isofluorane (3% induction and 1% maintenance with 100% O_2 at a 1,000 ml/min constant flow rate). T_2-weighted MR images were acquired at 1 day and 7 days after intravenous injection of Au/Fe/Au plasmonic NPs (150 μl, without MTX, 1 mg/ml in PBS). T_2 map and T_2 color map images were processed with the Image Sequence Analysis Tool of Bruker Paravision 5.1 (Bruker Biospin, Ettlingen, Germany).

Since $1/T_2$ increased with increasing Au/Fe/Au plasmonic NPs concentration, lower T_2 values represented more NPs. In the control group, similar amounts of NPs were accumulated in the inflamed paws at 1 and 7 days after NP injection. In contrast, the mice caged with the magnet showed larger NP amounts accumulated in the inflamed paw, and the NP amount increased over time (Figure 47a and b), as seen in the *in vivo* NIR absorbance images. These results confirmed that external magnetic fields resulted in greater Au/Fe/Au plasmonic NP delivery to the inflamed paws and enhanced NP retention.

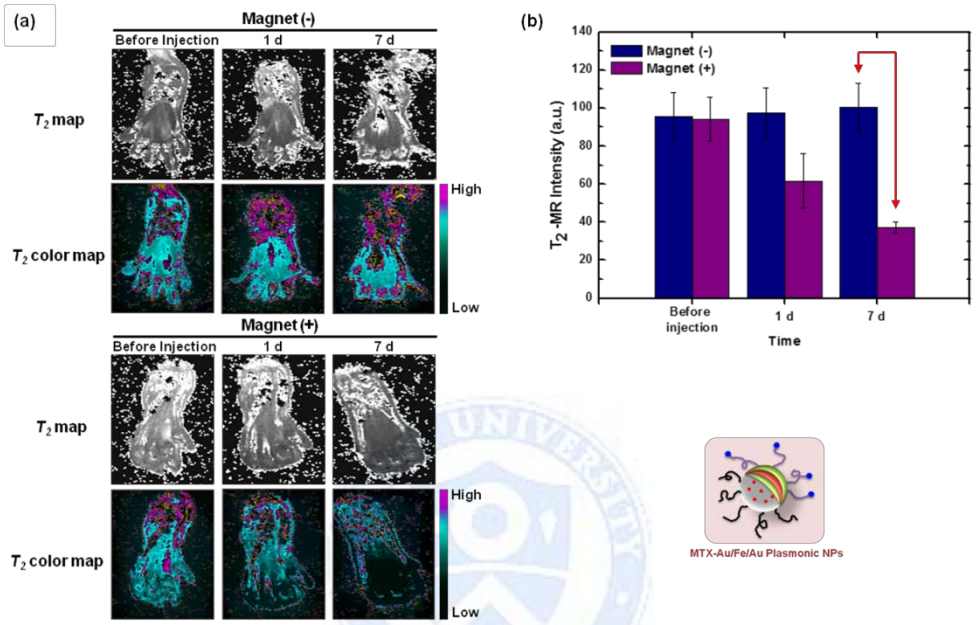

Figure 47. (a) Time-lapse *in vivo* T_2-weighted MR images of inflamed paws of CIA mice injected intravenously with Au/Fe/Au plasmonic NPs (150 μl, 1 mg/ml in PBS) with (+) or without (-) a magnet. (b) T_2-weighted MR signal as a function of time for Au/Fe/Au plasmonic NPs-treated mice with (+) or without (-) a magnet.

3.3.4. *In vivo therapeutic effects*

First, *in vivo* local heat generation by NIR irradiation was investigated prior to the study of *in vivo* therapeutic effects of NPs.

Heat is locally generated by NIR irradiation because the Au half-shells have an absorption peak in the NIR region. To determine the temperature increase upon NIR exposure, the temperature of CIA mice treated with saline, MTX-Au plasmonic NPs or RGD-MTX-Au plasmonic NPs 24 h post-injection was measured using a thermal imaging camera (FLIR-T250, FLIR, Sweden) when the right inflamed paw was exposed to 1.59 W/cm^2 NIR light for 10 min using a laser diode ($\lambda \approx 808$ nm). Before NIR exposure, the temperature was approximately 36 °C over the whole body, corresponding to the body temperature of the mouse. However, after 10 min of NIR irradiation, the temperature of the irradiated paw increased to 39, 42, and 48 °C for the mice treated with saline, MTX-PLGA-Au nanoparticles, and RGD-MTX-PLGA-Au nanoparticles, respectively (Figure 48a). In the case of MTX-Au/Fe/Au plasmonic NPs, NIR irradiation increased the temperature of the inflamed paw to ~ 45 °C (Figure 48b). These temperatures are not high enough to induce irreversible tissue damage.

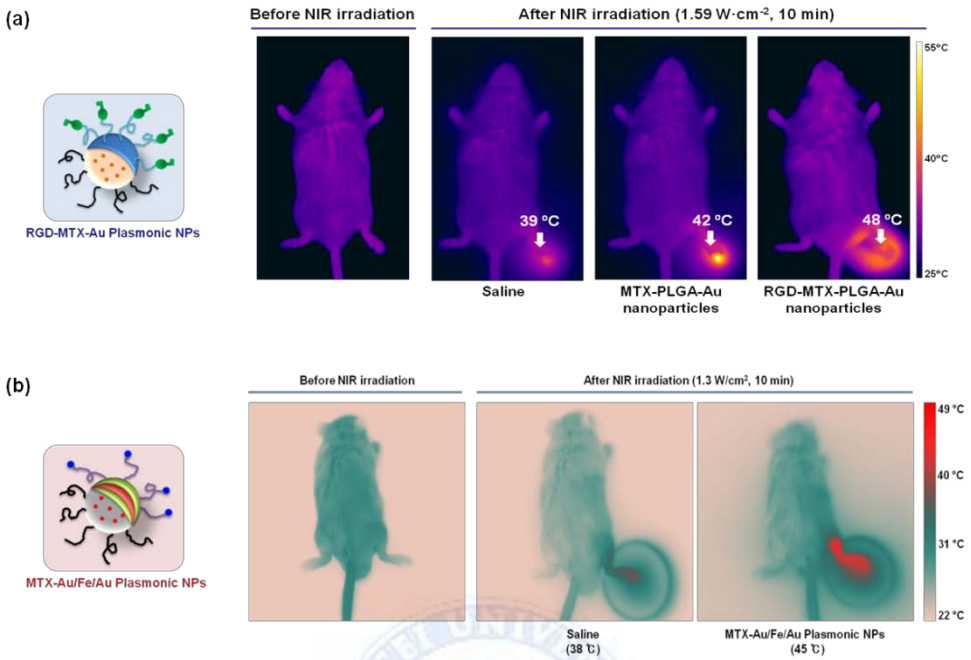

Figure 48. (a) Thermal images of CIA mice treated with saline, MTX-PLGA-Au nanoparticles (150 μl, 1 mg/ml dispersed in PBS), or RGD-MTX-PLGA-Au nanoparticles (150 μl, 1 mg/ml dispersed in PBS) before and after NIR exposure (1.59 W/cm^2, 10 min) of the right paw. (b) Thermal images of CIA mice treated with saline, MTX-Au/Fe/Au plasmonic NPs (150 μl, 1 mg/ml in PBS) before a nd after NIR irradiation (1.3 W/cm^2, 10 min) of the inflamed paws. The thermal images of MTX-Au/Fe/Au plasmonic NPs injected CIA mouse for NIR irrad iation were acquired using thermal imaging camera (FLIR-T250, FLIR, Swed en).

In addition, to examine the *in vivo* local MTX release from MTX-PLGA-Au plasmonic NPs under NIR irradiation, rhodamine loaded nanoparticles with Au half-shell (Rhodamine-PLGA Au Plasmonic NPs) were synthesized by similar procedure of MTX-PLGA Au Plasmonic NPs.

Total 50 μl of rhodamine solution (5 mg/ml Rho) was injected into hind foot pad of two CIA mice. The same volume of Rhodamine-PLGA Au Plasmonic NPs (4 μg/ml Rho) was subcutaneously injected into hind foot pad of two CIA mice, and these limbs were irradiated with NIR 1.96 W/cm^2. The amount of rhodamine per same volume in NPs is about 1/1200 of rhodamine solution. One mouse from each group was sacrificed 1 h after injections, and the other from each group was sacrificed 24 h after injection. All samples were counterstained with 4',6-diamidino-2-phenylinodole (DAPI). The paws embedded in OCT compound and horizontally sectioned. Rhodamine accumulation was surveyed for 1 h and 24 h following the injection. Since MTX could not excited by laser, a red fluorescence dye, rhodamine, was loaded into the PLGA-Au plasmonic NPs. In case of the mouse injected with rhodamine solutions, rhodamine were prominently detected after 1 hour, but not detected after 24 h because rhodamine was rapidly cleared from the body. In contrast, scanty rhodamine was detected in paw after injection of rhodamine-PLGA-Au plasmonic NPs. However, after NIR irradiation for 10 min at rhodamine-PLGA-Au plasmonic NPs injected site, the released rhodamine was detected in the injected paw at 1 h. After 24 h of NIR irradiation, rhodamine was more detected in arthritis paw (Figure 49). These results confirm that the loaded rhodamine within the rhodamine-PLGA-Au plasmonic NPs can be locally and

slowly released and sustained for a long time in the locally NIR irradiated areas in *in vivo* system.

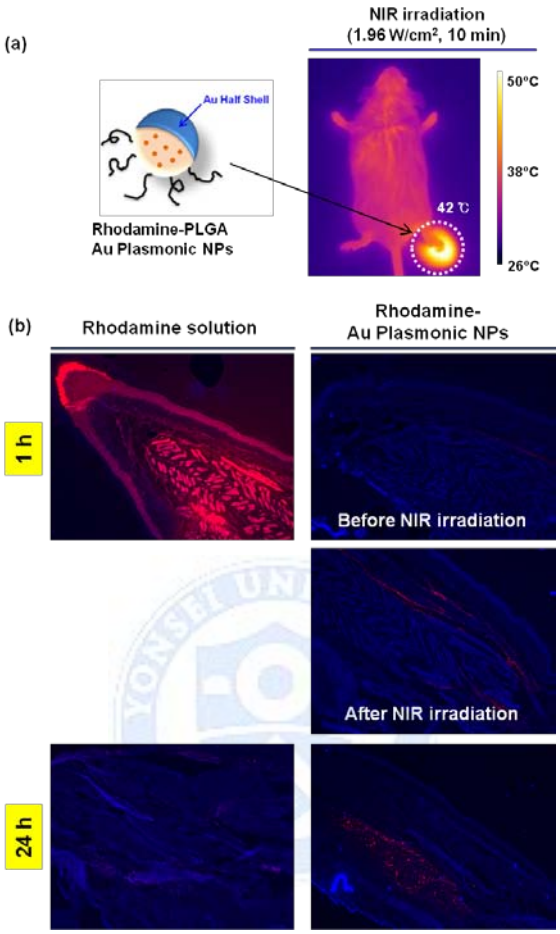

Figure 49. (a) Thermal image of CIA mice subcutaneously treated with rhodamine-PLGA Au plasmonic NPs (50 μl, 4 μg/ml Rho) after NIR irradiation at the right paw. (b) Time-lapse immunofluorescence images of arthritis hind foot pads after injected with rhodamine solution or rhodamine-PLGA Au plasmonic NPs (red : rhodamine, blue : 4',6-diamidino-2-phenylindole (DAPI)).

Next, I confirmed the *in vivo* therapeutic effects after RGD-MTX-Au plasmonic NPs or MTX-Au/Fe/Au plasmonic NPs treatment. In order to investigate the therapeutic effects of RGD-MTX-Au plasmonic NPs, comparative efficacy studies were carried out (Figure 50a). CIA mice were divided into five groups (n = 5 mice per group), and 150 μl of each treatment was administered *via* intravenous tail injection as summarized in Table 5. For MTX, 35 mg/kg was injected four times every week. In the mice treated with RGD-MTX-PLGA-Au nanoparticles (0.15 mg/kg MTX) without NIR irradiation (group 3), the clinical indices slowly decreased until about day 20 and then increased again, though they were lower than those of the saline-treated mice (group 1). However, when the mice were treated with RGD-MTX-PLGA-Au nanoparticles (0.15 mg/kg MTX) and exposed to 1.59 W/cm^2 NIR light for 10 min at 24 h after intravenous injection (group 4), the clinical indices were lower than those of the mice treated with free MTX solution four times every week (group 2), which might be due to photothermally controlled drug release. For group 3, MTX was slowly released from nanoparticles; therefore, the released dosage of MTX was probably at a sub-therapeutic level, resulting in the small therapeutic effects. In contrast, the temperature of the inflamed paw exposed to NIR light increased to 48 ^{o}C, leading to a release of more than 20% of the loaded MTX within 12 h. This dosage of MTX released locally in the inflamed paw was likely above the therapeutic dose, so high therapeutic efficacies were obtained for group 4. The nanoparticles injected into group 4 contained only 0.15 mg/kg of MTX, which was 1/930 of the dose in group 2, suggesting that the nanoparticle-based treatment would contribute to

minimizing dosage-related side effects. The effect of NIR power density on therapeutic efficacy was also investigated (Figure 50b). The lowest clinical indices were obtained with 1.59 W/cm^2 NIR irradiation for 10 min. When the inflamed paws were exposed to 1.91 W/cm^2 NIR light, the clinical index was not reduced. These findings implied that moderate heat might relieve RA, but too much heat aggravated it.

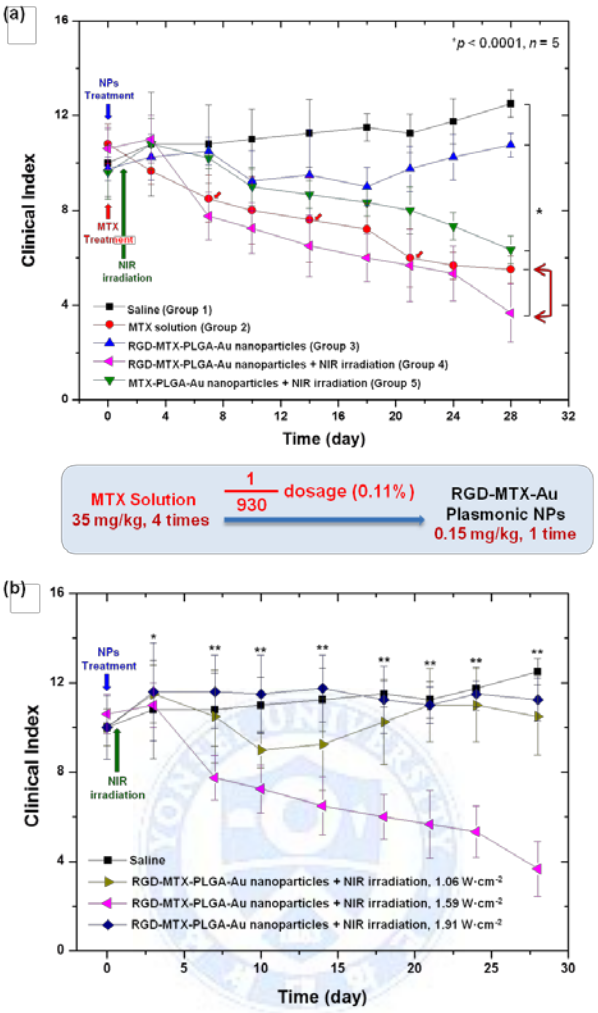

Figure 50. (a) Clinical index versus time for CIA mice injected intravenously with saline (group 1), MTX solution (35 mg/kg × 4 times, group 2), RGD-MTX-PLGA-Au nanoparticles (0.15 mg/kg of MTX, group 3), RGD-MTX-PLGA-Au nanoparticles (0.15 mg/kg of MTX) with NIR irradiation (1.59 W/cm^2, 10 min, group 4), or MTX-PLGA-Au nanoparticles (0.15 mg/kg of MTX) with NIR irradiation (1.59 W/cm^2, 10 min, group 5). Error bars represent standard deviation (n = 5). Clinical indices were significantly different among groups (*p < 0.0001).

To confirm the *in vivo* therapeutic effects after RGD-MTX-Au plasmonic NPs treatment, micro-computed tomography (CT) was also performed. Each experimental mice paws were scanned using micro-CT system (NFR Polarys-G90, Nanofocusray Int, Iksan, Korea). Images were acquired at 80 kVp, 150 mA, and 5 s/frame, with 360 views. The estimated radiation dose was approximately 6.9 mGy using image acquisition protocol. Scanned paws reconstructed into the three-dimensional structure and evaluated by NFR Polarys software (Exxim Computing Corporation, Pleasanton, USA). To confirm volumetric change of arthritis joints, 3-dimensional bone volume (BV) including phalanges and metatarsal bones was measured using Aquarius software (version 4.4.6, TeraRecon, Inc.)

Three-dimensional micro-CT was performed to assess bony changes in the paws of CIA mice (Figure 51). The paws of saline-treated CIA mice exhibited severe bone destruction. On the other hand, the bony structures were relatively well preserved in the paws of groups 2 (MTX solution) and 4 (RGD-MTX-Au plasmonic NPs with NIR irradiation). To determine the extent of bone preservation, the bone volume of the paws of CIA mice was measured. The bone volume in the treated group tended to be better preserved.

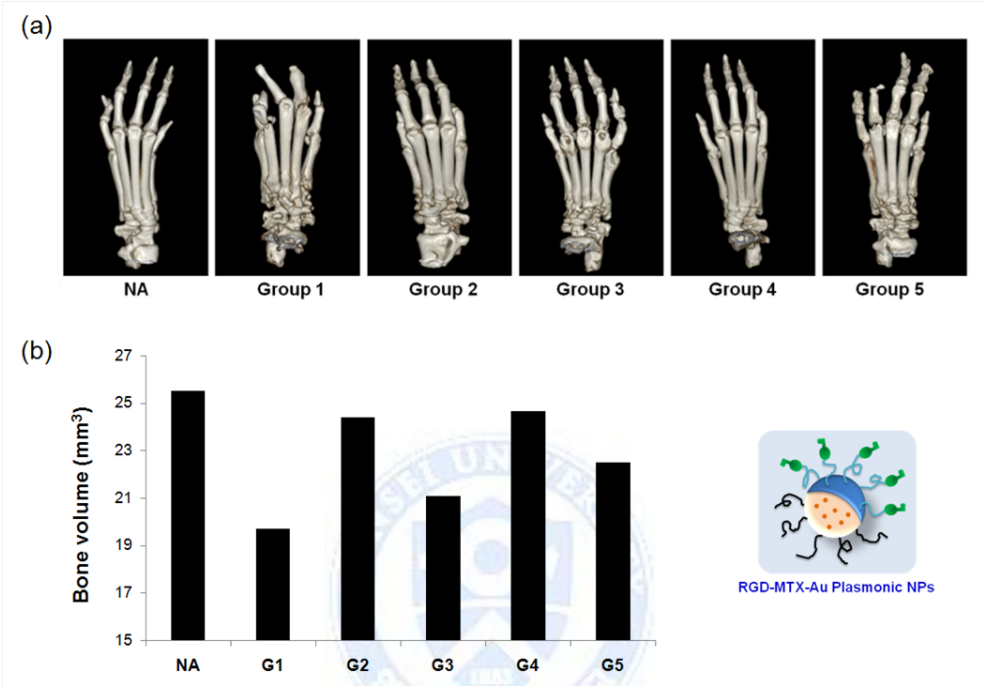

Figure 51. Micro-computed tomography (CT) scan of paws from the normal mouse (NA) and CIA mice after each treatment. (a) Three dimensional reconstruction of micro-CT imaging of the paws of CIA mice. (b) Bone volume of paws of CIA mice.

Next, clinical indices of MTX-Au/Fe/Au plasmonic NPs-treated mice were investigated. The CIA mice were divided into seven groups (n = 3 in each group) and treated as summarized in Table 6. When arthritis was fully developed (group mean clinical index of 8 - 10), the mice were injected with saline (G1), MTX solution (G2), or MTX-Au/Fe/Au plasmonic NPs (G3-G7). G2 received twice weekly intraperitoneal injections of 35 mg/kg MTX solution till sacrifice. G3 through G7 received a single intravenous tail vein injection of NP solution containing 0.15 mg/kg of MTX (150 μl, 1 mg/ml in PBS). G5, G6, and G7 were caged with the Nd-Fe-B magnet of 2.3 T, while G3 and G4 were caged without the magnet. G4 and G6 were irradiated with NIR light (1.3 W/cm^2) for 10 min at 1 day after injection. G7 was exposed to NIR light (1.3 W/cm^2) for 10 min on two occasions: at 1 and 7 days after injection. NIR irradiation increased the temperature of the inflamed paw to ~ 45 °C (Figure 48b).

Compared to saline-treated mice (G1), all other groups showed decreased clinical indices with some variations observed depending on the day. Photothermally treated mice (G4 and G6) generally exhibited lower clinical indices than mice treated with NPs and unexposed to NIR light (G3 and G5), regardless of magnetic field application. This implied that the MTX burst release upon NIR irradiation contributed to decreasing the clinical index more effectively compared to the slow MTX release without NIR irradiation. The photothermally treated mice (G4 and G6; 0.15 mg/kg MTX) showed therapeutic efficacy comparable to the MTX treated mice (G2; 35 mg/kg × 9 times = 315 mg/kg), with only 0.05% of the MTX dosage used in G2. Interestingly, a second exposure to NIR light at the 7th

day in the presence of external magnetic field (G7) achieved higher therapeutic effects (Figure 52a and b). Therefore, magnetic targeted chemo-photothermal treatment provides higher therapeutic efficacy compared with conventional or chemo-photothermal treatment.

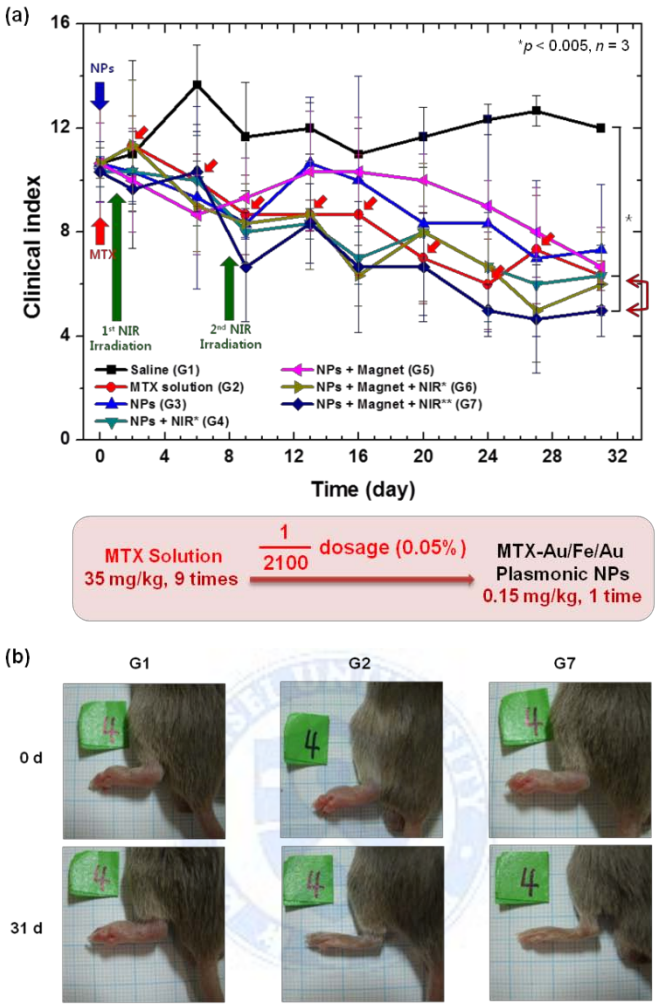

Figure 52. (a) Clinical index of the paws of CIA mice after treatment with saline (G1), MTX solution (35 mg/kg × 9 times; G2), or MTX-Au/Fe/Au plasmonic NPs (0.15 mg/kg of MTX; G3), as well as after treatment with MTX-Au/Fe/Au plasmonic NPs (0.15 mg/kg of MTX) followed by NIR irradiation (1.3 W/cm^2, 10 min; G4), followed by caging with a magnet (2.3 T, 31 days; G5), followed by NIR irradiation and a the magnet (1.3 W/cm^2, 10 min and 2.3 T, 31 days; G6), or

followed by two exposure to NIR irradiation and a magnet (1.3 W/cm^2 × 2 times, 10 min × 2 times and 2.3 T, 31 days; G7). Error bars represent the standard deviation (n = 3). *p < 0.005 compared to the saline treated mice (G1). (b) Photo of paws from the CIA mice before (0 d) and after treatment (31 d) with saline (G1), MTX solution (35 mg/kg × 9 times, G2), and MTX-Au/Fe/Au plasmonic NPs (0.15 mg/kg of MTX) with repeated NIR irradiation and under the magnet (1.3 W/cm^2 × 2 times, 10 min × 2 times and 2.3 T, 31 days, G7). The same mouse of each group (G1, G2, and G7) was observed during 31 days.

Finally, histological examinations of joints 28 days after intravenous injection of RGD-MTX-Au plasmonic NPs were performed (Figure 53a). The mice were anesthetized and sacrificed 28 days (or 32 days for the MTX-Au/Fe/Au plasmonic NPs experiment) after each treatment. Joints were removed for histopathological examination and fixed in 10% buffered formalin-saline at 4 °C for 1 week. The joints were decalcified in Calci -Clear Rapid solution (National Diagnostics, Atlanta, USA), and specimens were processed for paraffin embedding. Joint tissues were embedded in paraffin blocks and 5-μm-thick paraffin sections were mounted on a glass slide for hematoxylin and eosin (H&E) and safranin-O staining. The joint sections were scored for changes in synovial inflammation, and cartilage erosion, all on a scale of 0-4, which were evaluated as previously described [95]. Deparaffinized sections were incubated with specific antibodies directed against IL-Iβ, IL-6 (Santa Cruz Biotechnology, Santa Cruz, USA), or TNF-α (Hycult Biotechnology, Uden, Netherlands), followed by the appropriate peroxidase/DAB secondary antibodies (DAKO, Glostrup, Denmark). Expression of the different cytokines in the synovial tissue was scored semiquantitatively on a 4-point scale [96]. A score of 0 represented no expression, 1 mild expression, 2 moderate expression, and 3 abundant expression of a cytokine. All histologic analyses were preformed independently and blindly by two individual assessors, and the average of their scores was calculated.

Group 1 exhibited marked synovial inflammation and cartilage erosion, whereas the extent of synovial inflammation and cartilage erosion was reduced in groups 2 and 4 (Figure 53b). Pro-inflammatory cytokines, including IL-1β, IL-6,

and TNF-α, are centrally involved in the pathogenesis of RA and their expressions are closely related to the inflammatory activity of RA. Immunohistochemical staining showed increased TNF-α, IL-6, and IL-1β expression around the joint in group 1, whereas they were significantly decreased in groups 2 and 4 (Figure 53b). There were no significant differences between group 2 and group 4.

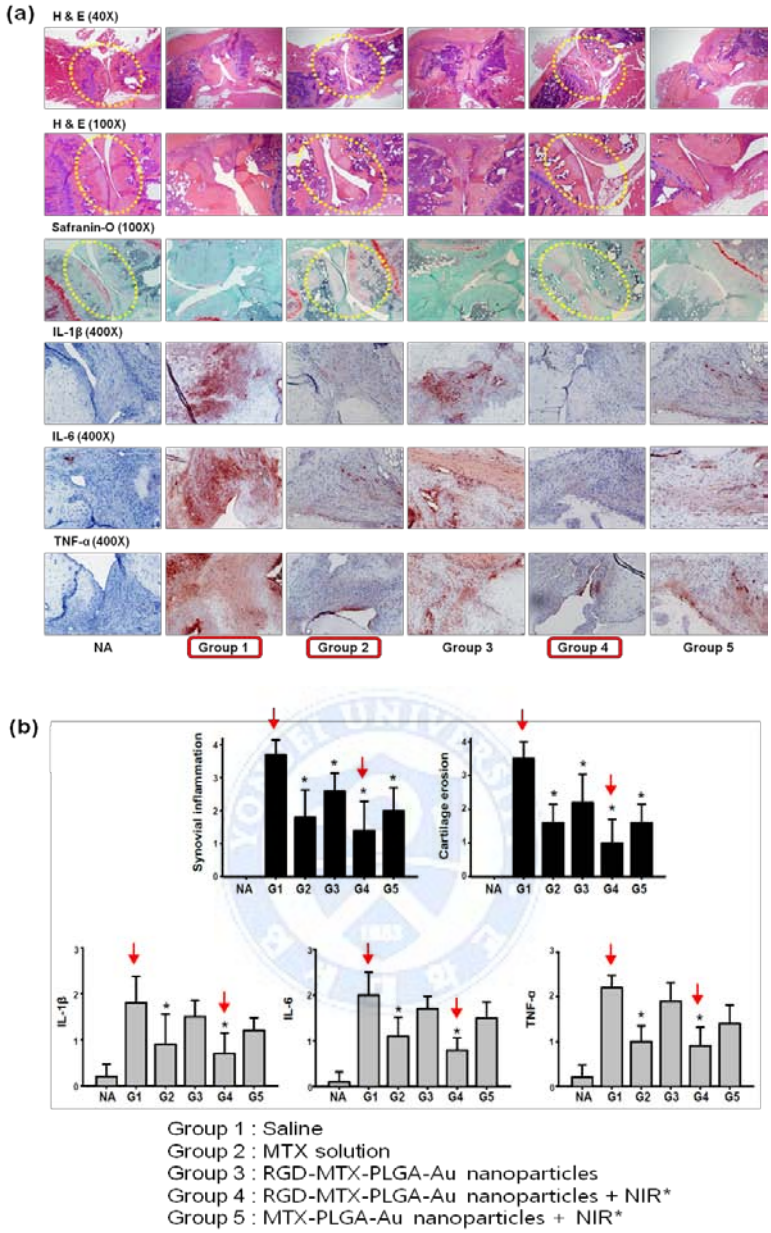

Figure 53. (a) Histology of joint tissues extracted from a normal mouse (NA) and CIA mice 28 days after each treatment. H&E (synovial inflammation, original magnification, × 40, × 100), safranin-O (cartilage erosion, original magnification, ×

100), and immunohistochemical staining for IL-1β, IL-6 and TNF-α (original magnification, × 400) stained representative joint sections from experiment. (b) Semi-quantitative analysis of histopathological evaluation (synovial inflammation and cartilage erosion) and immunohistochemical staining for IL-1β, IL-6 and TNF-α in CIA mice. The bars represent the standard deviation and asterisks (*) represent significance compared to untreated mice with $*p < 0.05$ ($n = 5$).

In the case of MTX-Au/Fe/Au plasmonic NPs, G1 showed inflammatory cell infiltration, bone erosion, and synovial proliferation, each of which was significantly decreased in G6 and G7. The results in G6 and G7 were comparable or superior to in the MTX treatment group (G2) (Figure 54a and b).

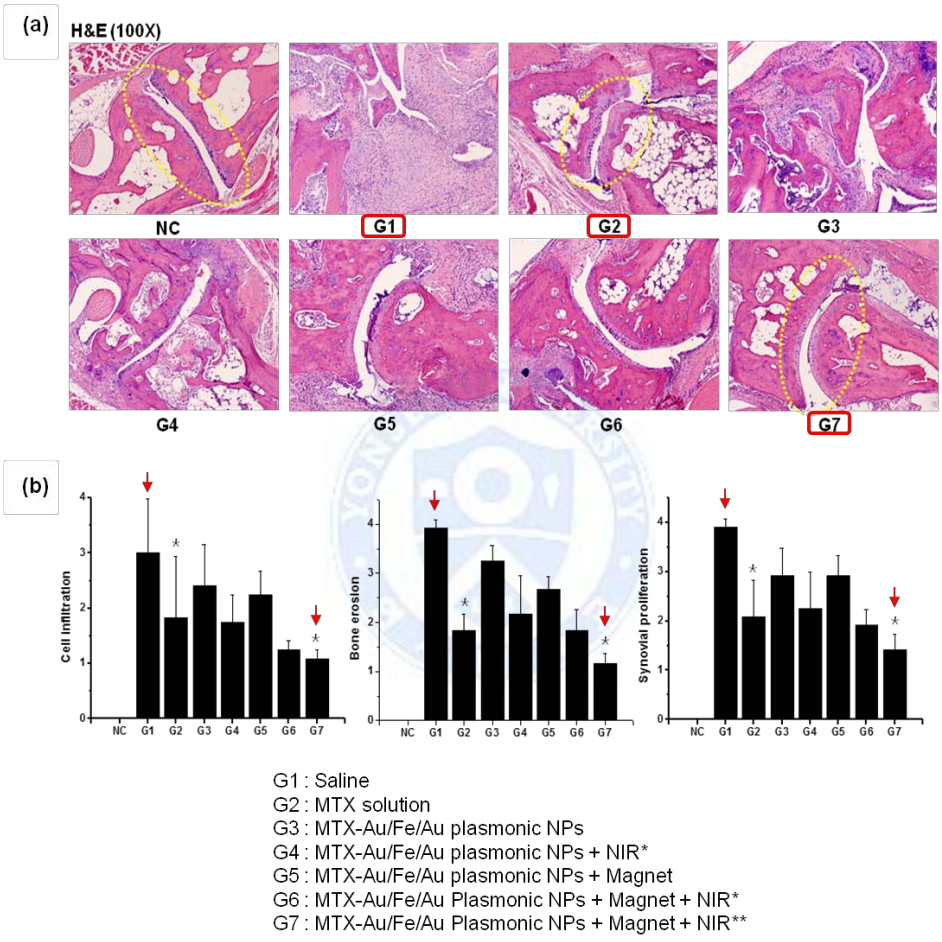

Figure 54. (a) Histology of joint tissues extracted from a normal mouse (NC) and from CIA mice 32 at days after each treatment. H&E-stained representative

joint sections from the experiment are shown (synovial inflammation, original magnification, 100×). (b) Semiquantitative analysis of histopathological evaluation (cell infiltration, bone erosion, and synovial proliferation) of CIA mice. Error bars represent the standard deviation (n = 3). *p < 0.05 compared to the saline treated mice (G1).

3.3.5. *In vivo toxicity*

In order to study the normal tissue toxicity caused by the RGD-MTX-Au plasmonic NPs, histological examinations of major organs (liver, spleen, kidney, lung, and heart) were investigated at 28 days post-injection (Figure 55a). No tissue damage was evident compared to the NPs-free control, implying that NPs accumulating in major organs did not induce *in vivo* toxicity.

Histological examinations of major organs were also performed at 32 days post-injection to investigate the influence of MTX-Au/Fe/Au plasmonic NPs on major organs (Figure 55b). Compared to the negative control, G7 showed no apparent tissue damage, implying that the NPs accumulated in major organs did not induce *in vivo* toxicity.

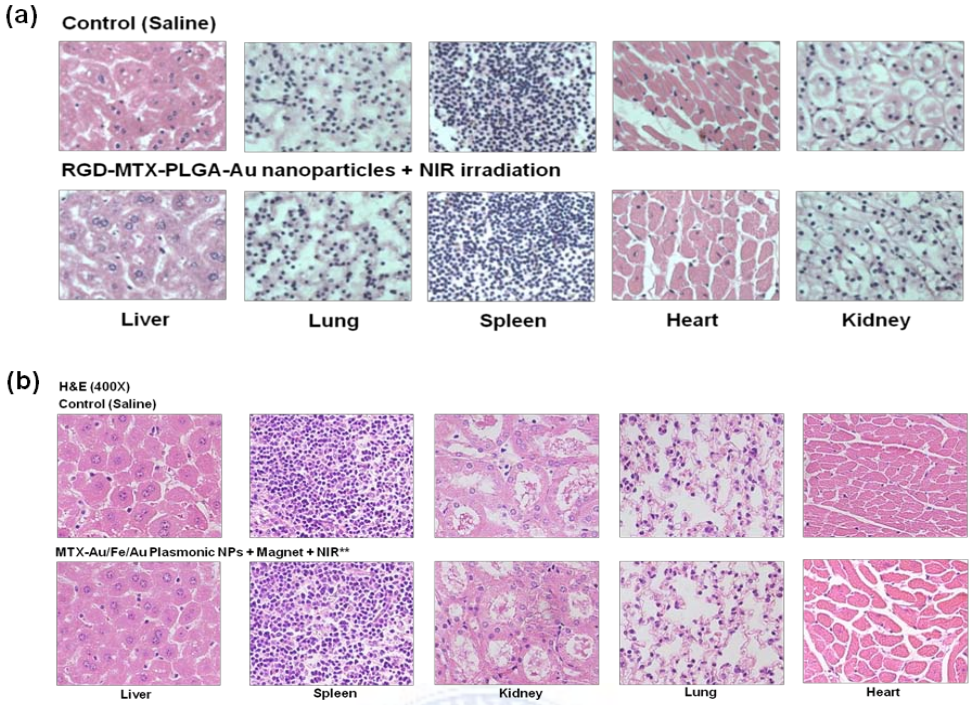

Figure 55. (a) Histological sections of major organs extracted 28 days after intravenous injection of saline (top) or RGD-MTX-PLGA-Au nanoparticles with NIR irradiation (bottom, group 4). Images were acquired at 400× magnification. (b) Histological sections of major organs extracted 32 days after intravenous injection of saline (top) or MTX-Au/Fe/Au plasmonic NPs (0.15 mg/kg of MTX) with repeated NIR irradiation and under the magnet (1.3 W/cm^2 × 2 times, 10 min × 2 times and 2.3 T, 31 days, G7) (bottom). H&E-stained images were acquired at 400× magnification.

A hematological analyses, including white blood count (WBC), platelets, aspartate aminotransferase (AST), alanine aminotransferase (ALT), blood urea nitrogen (BUN), and creatinine in blood were performed after MTX-Au/Fe/Au plasmonic NPs treatment (Table 7). Compared to the negative control, G3, G5, and G6 showed no significant toxicity supporting that the MTX-Au/Fe/Au plasmonic NPs caused no toxicity.

Table 7. Hematological ananlyses as white blood count (WBC), platelets, aspartate aminotransferase (AST), alanine aminotransferase (ALT), blood urea nitrogen (BUN), and creatinine in blood (data are given as mean value; n = 3 per each group).

Parameters	Reference range	Negative control	MTX-Au/Fe/Au Plasmonic NPs (G3)	MTX-Au/Fe/Au Plasmonic NPs + Magnet (G5)	MTX-Au/Fe/Au Plasmonic NPs + Magnet + NIR (G6)
WBC (K/ul)	4,000 ~ 15,000	4,240	4,650	4,055	4,013
Platelets (10^3 K/ul)	600 ~ 1,000	606	812	904	792
AST (U/l)	54 ~ 298	81	86	121	123
ALT (U/l)	17 ~ 77	33	31	50	29
BUN (mg/dl)	8 ~ 33	25.3	18.3	16.0	19.1
Creatinine (mg/dl)	0.2 ~ 0.9	0.46	0.20	0.20	0.20

WBC : white blood count, AST : aspartate aminotransferase, ALT : alanine aminotransferase, BUN : blood urea nitrogen.

An important concern for nanoparticle-based treatments is whether the injected nanoparticles accumulate in organs or are cleared from the body. To investigate the biodistribution of RGD-MTX-PLGA-Au nanoparticles, the Au accumulated in major organs 1, 3, and 28 days after intravenous injection were measured using ICP-MS. Briefly, these tissues were dissolved in an *aqua regia* during overnight at 80 - 90 °C and re-heating at 120 – 130 °C was conducted for 12 h. The amount of ionized Au was analyzed by ICP-MS (PerkinElmer Nexion 300S).

Nanoparticles were efficiently taken up by the liver, lung, and spleen that are related with the reticuloendothelial system (RES), with less accumulation in the kidney or heart. However, most nanoparticles were cleared from the body after 28 days (Figure 56a). In the case of MTX-Au/Fe/Au plasmonic NPs, most NPs were cleared from the body after 28 days regardless of external magnetic field application (Figure 56b).

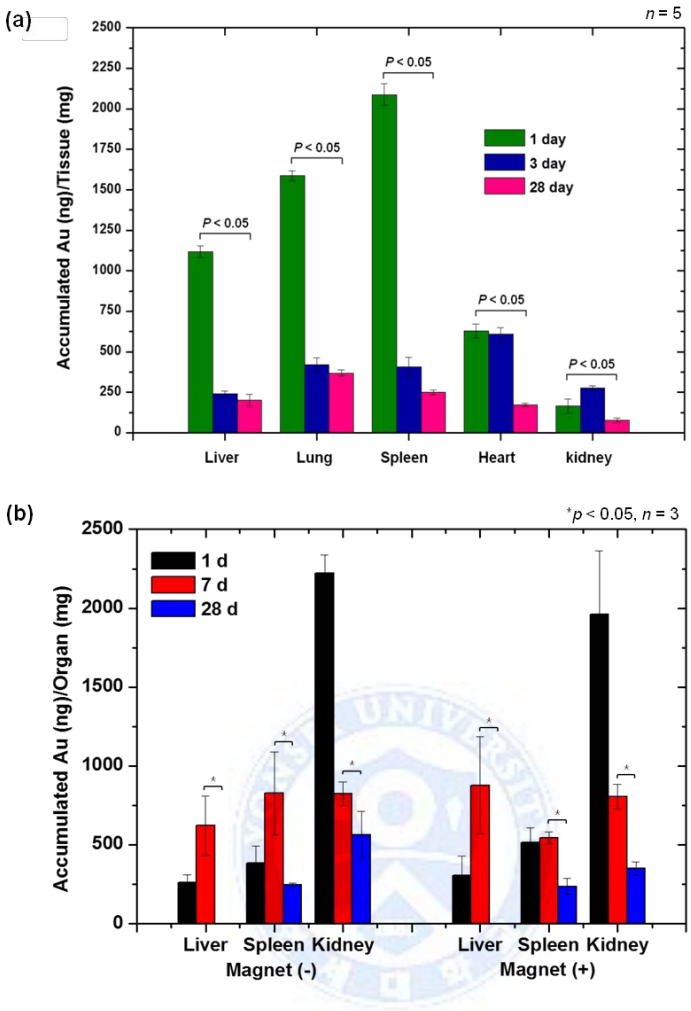

Figure 56. (a) Tissue distribution of RGD-MTX-Au plasmonic NPs in major organs at different times. The amount of Au was measured by ICP-MS (*t*-test, one-tailed, paired, liver, $p = 0.026$; lung, $p = 0.005$; spleen, $p = 0.031$; heart, $p = 0.002$; kidney, $p = 0.039$). Error bars represent standard deviation ($n = 5$). (b) Tissue distribution of NPs in major organs (liver, spleen, and kidney) at different times. The amount of Au was measured by ICP-MS. Error bars represent standard deviation ($*p < 0.05$, $n = 3$).

3.4. Summary

The therapeutic effects of RGD-MTX-Au plasmonic NPs and MTX-Au/Fe/Au plasmonic NPs in CIA mice were investigated. When the nanopartlces were injected intravenously into the CIA mice, *in vivo* NIR absorbance images revealed that the nanoparticles selectively accumulated in the inflamed region. Upon NIR irradiation (1.59 W/cm^2, 10 min), the temperature of the inflamed paw increased to 48 ^{o}C, leading to the burst release of MTX from the nanoparticles. Compared to conventional treatment with MTX, the RGD-MTX-Au plasmonic NPs-based treatment combined with NIR irradiation had greater therapeutic efficacy with a much smaller dosage of MTX in the nanoparticles. These results demonstrate that the targeted chemo-photothermal treatment using multifunctional nanoparticles is a useful and effective strategy for maximizing the therapeutic efficacy and minimizing dosage-related side effects in the treatment of RA.

In addition, the MTX-Au/Fe/Au plasmonic NPs were successfully fabricated and shown to be applicable for multimodal imaging and magnetic targeted chemo-photothermal treatment. Following intravenous injection of these NPs into CIA mice, *in vivo* NIR absorbance and MR images revealed NP accumulation in the inflamed paws, which was enhanced under the external magnetic field. NIR irradiation increased the temperature of the exposed area and accelerated the MTX release rate from the NPs, allowing the chemo-photothermal treatment. Furthermore, combination with consecutive NIR irradiation and external magnetic

field application resulted in higher therapeutic efficacy compared to conventional treatment, despite the use of a much smaller MTX dosage (0.05%) in the injected NPs.

Chapter 4.

Multi walled carbon nanotubes electrodes : application in discrimination of lipid region in *ex vivo* atherosclerosis using capacitance imaging

4.1. Introduction

4.1.1. Atherosclerosis

Atherosclerosis (AS) which is characterized by the accumulation of lipids in artery is the most common cause of stroke and myocardial infarction (heart attack) [97]. During AS progression, the lumen of the artery was narrowed due to the atherosclerotic plaque, resulting in the reduction of blood supply to organs, especially heart and brain. The atherosclerotic plaque begins with a fatty streak originated from the accumulation of foam cells. After then, a smooth muscle cell and T cell lead to the state of chronic inflammation and then thrombus was formed in the lumen accompanied with necrotic core. Eventually, the lumen was narrowed

and the blood flow to the organ was reduced (Figure 57) [98]. Foam cells, which are hallmark of initiation of AS, are formed from the lipoproteins-contained macrophages. The macrophage-derived foam cells, which are formed by oxidized low-density lipoprotein (oxLDL), are the crucial marker for early AS. So, the confirmation of foam cells formation is critical for evaluating AS. Observation of foam cell formation is usually conducted by conventional Oil Red O (ORO) staining method for lipid-laden macrophages in both *in vitro* and *ex vivo* [99].

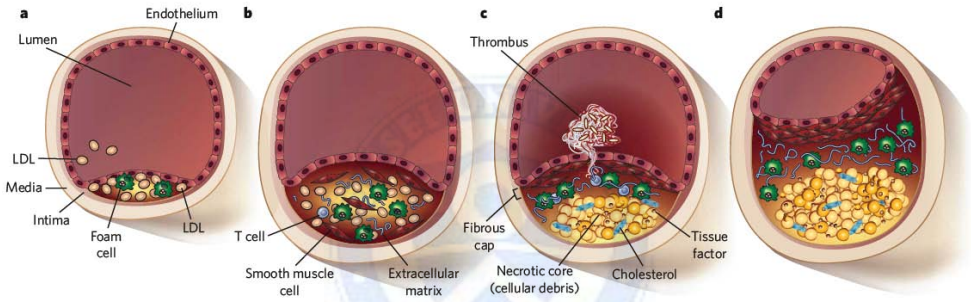

Figure 57. Progression of atherosclerosis [98].

The AS has been studies using animal models, such as mice, rabbits, and pigs. Mice deficient in apolipoprotein E (apoE$^{-/-}$) or the low-density lipoprotein (LDL) receptor have been used for studies of AS. The accumulation and aggregation of lipoprotein particles were observed in the intima of artery after feeding of high-fat diet as shown in Figure 58a and b. After then, monocytes

transmigrate into the intima and differentiate into macrophages. Foam cells formed from the lipoproteins-contained macrophages (Figure 58c and d). In other words, foam cells are ‘cholesterol-engorged macrophages’. The macrophage-derived foam cells, which are formed by oxidized low-density lipoprotein (oxLDL), is the crucial marker for AS. So, the assessment of foam cells formation is critical for evaluating AS. Observation of foam cell formation is usually conducted by Oil Red O (ORO) staining of lipid-laden macrophages in both *in vitro* and *ex vivo*. The lipids in foam cells affect to the necrotic core of the lesions after foam cells die. The lesions continue to grow and enter at the shoulder of the vessel (Figure 58e), eventually lead to AS.

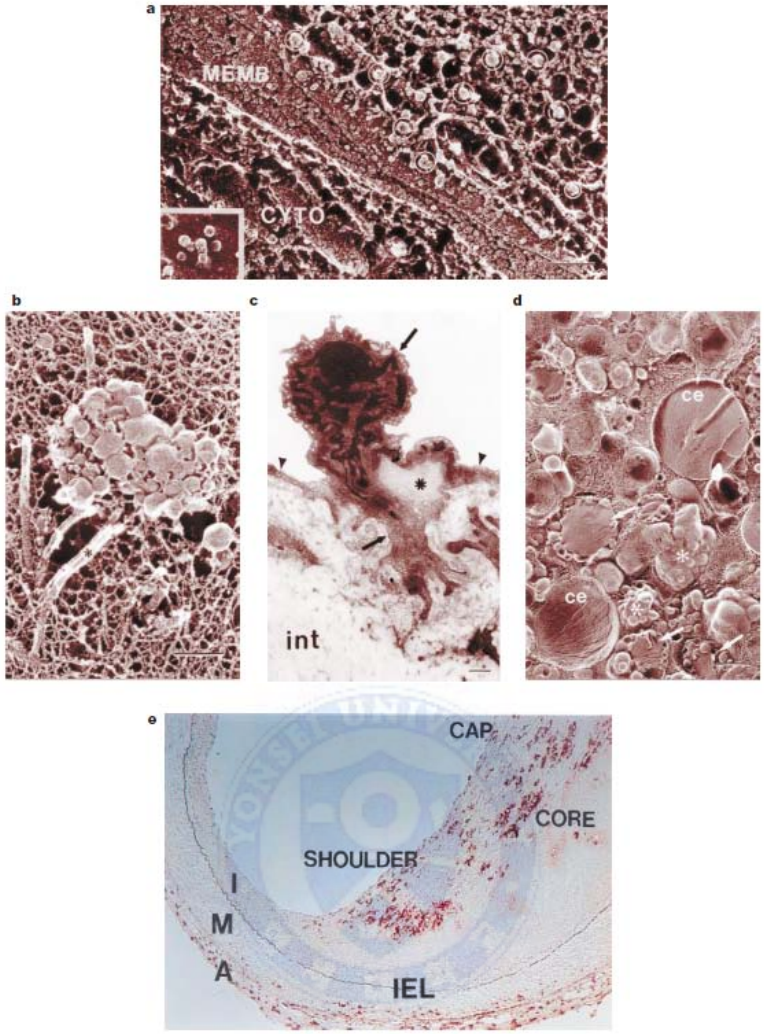

Figure 58. Initiation and progression of atherosclerotic plaques [97]. (a) The freeze-etch electron micrograph image of the accumulated 23-nm LDL particles (circle) in the matrix of a rabbit atrioventricular valves after incubation with LDL (inset). Scale bar: 0.1 μm. Abbreviations: MEMB, plasma membrane; CYTO, cytoplasma. (b) The freeze-etch electron micrograph image of the aggregated lipoprotein of rabbit intima after LDL treatment. Asterisk indicates matrix and collagen fibrils. Scale bar: 0.2 μm. (c) The electron micrograph image of a cross-section of the aorta

in apoE$^{-/-}$ mouse shows transmigration of monocyte into the intima (int). Asterisk indicates a cluster of lipid. Arrows and arrowheads indicate monocyte and endothelial cells, respectively. Scale bar: 0.5 μm. (d) The freeze-etch electron micrograph image of the cytoplasm of a macrophage in the intima of a rabbit fed a high-fat diet shows the formation of foam cell. Large lipid droplets with cholesterol esters (ce) were observed. Arrows and asterisk indicate lipid-filled compartments and aggregated LDL, respectively. Scale bar: 0.5 μm. (e) Light micrograph image of a section of an advanced human coronary atherosclerotic lesion. This sample was immunostained for the macrophage specific antigen EMB-11 (red). Abbreviations: A, adventitia; I, intima; IEL, internal elastic lamina; M, media.

Up to date, the diagnostic techniques for AS, such as angiography, computed tomography (CT), and intravascular ultrasound (IVUS) were mainly used in clinic. However, these techniques were expensive methods and needed experts to operate them, and some patients have side effects for the contrast agents used in angiography.

Some groups have reported the detection of lipid-rich atherosclerotic plaque in *ex vivo* using electrochemical impedance sensors. In these studies, impedance sensors, such as linear 4-point microelectrode which attached to balloon catheter, concentric bipolar microelectrodes, and flexible concentric bipolar microelectrodes with balloon catheter were fabricated [100-101]. Electrochemical impedance spectroscopy (EIS) which measures the alternating current (ac) impedance of tissue has shown that lipid-rich atherosclerotic plaque tissue has distinct electrochemical properties. Lipid-rich atherosclerotic plaque tissue has exhibited increase in frequency-dependent impedance compared to atherosclerotic plaque-free tissue in rabbits and human *ex vivo*. These studies have demonstrated that lipid-rich atherosclerotic plaque could be detected using EIS sensor in *ex vivo*. However, detection and visualization of lipid region in atherosclerotic plaque remain an unmet. In addition to detect the lipid, it is important to visualize the lipid region in high resolution for the early diagnosis of AS.

4.1.2. Principle of capacitance imaging

To overcome this issue, I have developed capacitance imaging technique for the detection and visualization of foam cells that are filled with lipids in atherosclerotic plaque *ex vivo*. In previous study, real-time monitoring of adipocyte differentiation using capacitance sensor have been reported [102]. Lipid droplets contained adipocytes (3T3-L1 cell) were differentiated after FFA (free fatty acid) treatment. Because lipid droplets in adipocytes have unique dielectric constant (ε), capacitance could be measured *via* the relationship: $C = \varepsilon A/d$, where A is the electrode area and d is the distance between the two electrodes (Figure 59a). I anticipate that it is also possible to detect the lipid filled foam cells in atherosclerotic plaque *ex vivo* by measuring capacitance (Figure 59b). Moreover, lipid filled foam cells could be visualized from the capacitance values.

Here, I report capacitance imaging technique for discrimination of lipid region in atherosclerotic plaque *ex vivo* using polypyrrole-coated multi walled carbon nanotubes multi electrodes array (PPy-MWNTs-MEA). Compared to TiN multi electrodes array (TiN-MEA), enhanced contact between electrodes and atherosclerotic plaque interface, low electrode impedance, and improved mechanical stability leads to the apparent discrimination of lipid region using PPy-MWNTs-MEA. I also demonstrate the feasibility of flexible multi electrodes array (F-MEA) for identification of lipid region.

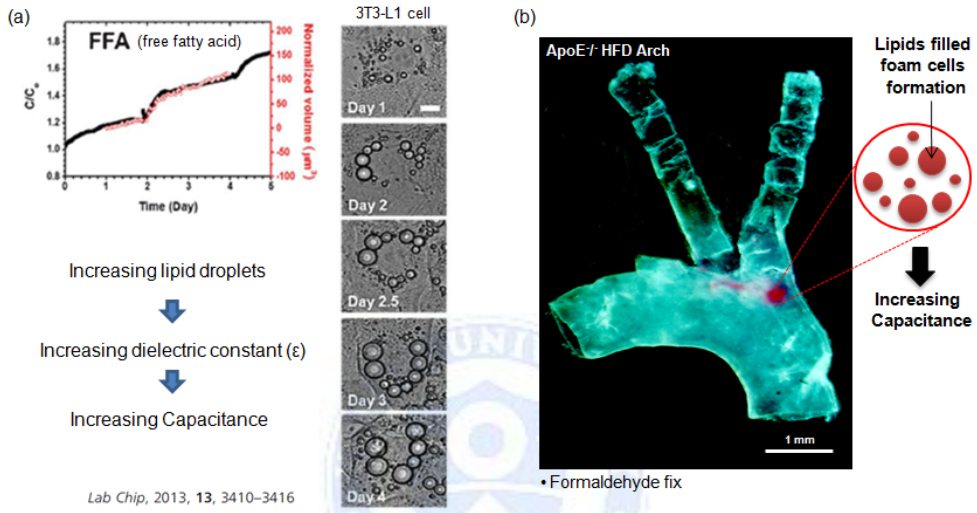

Figure 59. (a) Capacitance measurements for adipocytes, (b) Capacitance imaging of lipid region in atherosclerosis.

4.2. Experimental details

4.2.1. Fabrication of polypyrrole-coated MWNTs MEA

Fabrication of the MWNTs MEA consisted of 60 electrodes which have 30 μm in diameter with 100 μm distance between electrodes proceeded in three steps: formation of bottom electrode, passivation and catalyst patterning, and MWNTs growth. The positive photoresists were spin-coated on quartz substrate (Thickness : 0.5 mm) and the bottom electrode was fabricated by using conventional photolithography and lift-off. The Ti (5 nm) adhesion layer followed by Pt (100 nm) were deposited using sputter. After bottom electrode patterning, the passivation patterning were performed by photolithography followed by deposition of SiO_2 (200 nm) using e-beam evaporator and lift-off. Lastly, patterns for catalyst position were introduced on the bottom electrode. The SiO_2 (20 nm) and Cr (5 nm)/Co(5 nm) were successively deposited using e-beam evaporator. The Co (5 nm) was used as catalyst layer. Finally, the MWNTs were grown by the plasma-enhanced chemical vapor deposition (PECVD) at 650 °C for 30 min with C_2H_2 (60 sccm) as a carbon source. A hydrogen (160 sccm) was introduced in the chamber during MWNTs growth process and the pressure of the chamber was kept at 5.99 Torr with 70 W RF plasma.

TiN MEA (60MEA200/30iR-ITO) consisted of 60 electrodes (30 μm in diameter, including 1 reference electrode) with 200 μm distance between electrodes

was purchased from Multichannel systems (Germany, http://www.multichannelsystems.com).

To fabricate flexible MEA, thin films of single walled carbon nanotubes (SWNTs; PureTubes™, Nanointegris) were formed on membrane filter (VSWP04700, Millipore, 0.025 μm) using vacuum filtration followed by transfer to polyethylene terephthalate (PET) substrate. The membrane filter was removed by acetone. Then, the SWNTs patterns were made by using O_2 plasma (30 W, 20 s). A Cr (15 nm)/Au (100 nm) electrodes were patterned for the connection to LCR meter. The photoresist was used to passivate for SWNTs electrode while opening the sensing area. After then, pyrrole was elctro-deposited on the SWNTs electrode. The same structure of MEA consisted of 60 electrodes which have 30 μm in diameter with 100 μm distance between electrodes were constructed on the flexible PET substrate.

To electro-deposition of pyrrole on MWNs, pyrrole (99%, extra pure) was purchased from Acros Organics (New Jersey, USA). Pyrrole was electrodeposited onto MWNTs-MEA under the optimized conditions from an aqueous solution of 0.25 M pyrrole mixed with 0.1 M NaCl by using three-electrode system. The working electrode was MWNTs-MEA and the counter and reference electrodes were a Pt wire and an Ag/AgCl electrode (in a 3.5 M KCl solution), respectively. The Electro-deposition of pyrrole was performed using a potentiostat/galvanostat (Model 263 A, Princeton Applied Research, USA) at 0.75 V (vs. saturated calomel electrode (SCE)) for 1 min.

4.2.2. Animals and preparation of atherosclerosis *ex vivo* sample

Female apoE-/- mice (C57BL/6, 5 weeks old) were supplied by Orient Bio INC. (Central Lab Animal, Inc., Seoul, Korea). All animal experiments were performed in accordance with the Korean Food and Drug Administration (KFDA) guidelines. Protocols were reviewed and approved by the Institutional Animal Care and Use Committee (IACUC) of the Yonsei Laboratory Animal Research Center (YLARC). All mice were maintained in a specific pathogen-free facility at the YLARC. The mice were fed a high fat diet (HFD) supplemented with 2% cholesterol, 0.5% w/w cholate and 10% w/w lard oil for 4 weeks. At the ending of the HFD period, the mice were sacrified, and the aorta and heart tissues were dissected. These *ex vivo* samples were fixed using formaldehyde followed by stained with Oil Red O (Sigma-Aldrich Chemical Co., USA) solution.

4.2.3. Capacitance measurements

Capacitance, phase, and contact impedance were measured using an LCR meter (Agilent 4294A) with a data acquisition/switching unit (Agilent 34970A) connected to the LCR meter, respectively. Data were acquired under an ac voltage of 10 mV at a frequency sweep from 10 kHz to 100 kHz (or 500 Hz to 2900 Hz). During the measurements, a PDMS (polydimethylsiloxane) was mounted on the atherosclerotic plaque *ex vivo* sample to enhance contact between *ex vivo* sample and electrodes. All measurements were performed at ambient condition.

4.3. Results and discussion

4.3.1. Characterization of multi electrodes array (MEA)

Figure 60a shows a schematic diagram of the PPy-coated multi walled carbon nanotubes multi electrodes arrays (PPy-MWNTs-MEA). Standard photolithography and lift-off process were continuously used to fabricate Ti/Pt bottom electrodes, SiO_2 passivation layer, and Cr/Co pattern. Prior to the deposition of Cr/Co layer, 20 nm thickness of SiO_2 was deposited to Pt electrodes to prevent damage of Pt electrodes in high temperature (650 °C) during MWNTs growth process. To enhance the growth of MWNTs, plasma treatment was conducted during the synthesis process. The scanning electron microscope (SEM) image as shown in Figure 60b indicates that the MWNTs electrodes which 30 μm in diameter with 100 μm distance between electrodes were fabricated and the height of MWNTs was ~ 2 μm (inset). Then, pyrrole was electoro-deposited on MWNTs, leading to polypyrrole (PPy)-coated MWNTs. Because conducting polymer (e.g. PPy) has biocompatibility and electrochemical characteristics, it is widely used as a coating material for electrode of neural prosthetic device [103]. It is well known that MWNTs/conducing polymer composites have several advantages, such as low impedance of electrode, fast charge transfer, high capacitance, and enhanced mechanical stability [104]. Therefore, these

MWNTs/conducting polymer composited electrodes were used as neural prosthetic devices to improve neuronal recording.

Motivated by the properties of MWNTs/conducting polymer composited electrodes, I apply these electrodes to the capacitance imaging. The morphology of PPy-coated MWNTs electrodes is important to reduce contact resistance between electrodes and atherosclerotic plaque tissue. The SEM images of before (Figure 61a) and after (Figure 61b) electrodeposited pyrrole on MWNTs show that PPy was well coated on MWNTs. The SEM study suggests that PPy possibly acted as support fixture to improve mechanical strength of MWNTs, leading to enhance the stability of electrodes. The optical image shows that PPy-coated MWNTs (30 μm in diameter, black color) was fabricated on Pt electrodes (Figure 60c). We also used conventional TiN-MEA to compare the performance of capacitance imaging with PPy-MWNTs-MEA (Figure 60d).

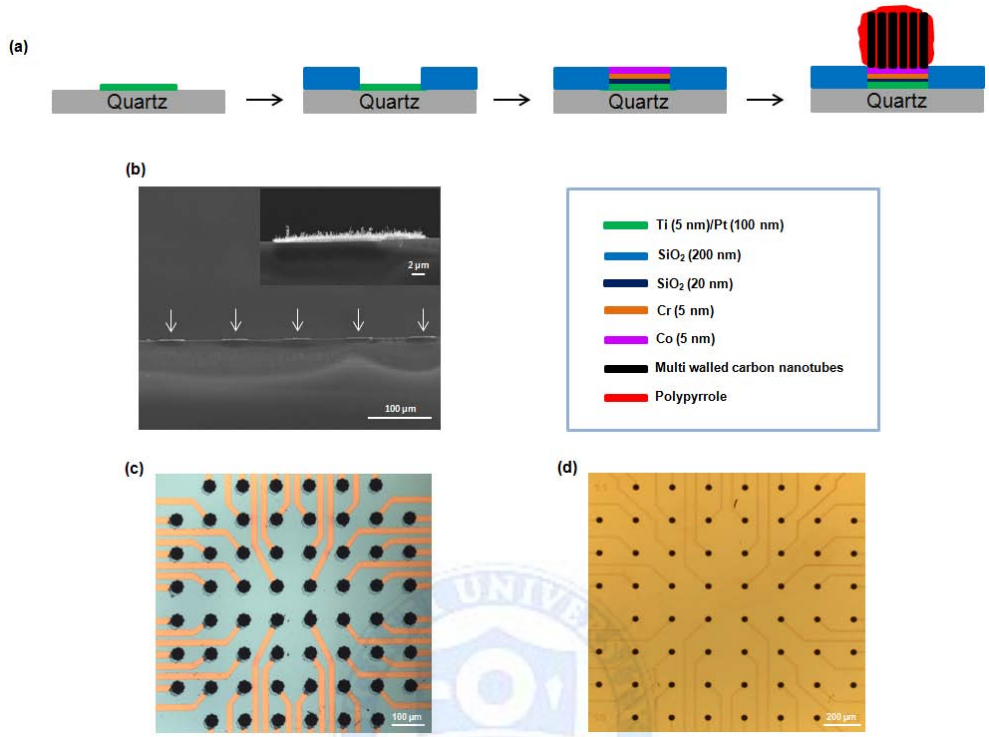

Figure 60. (a) Schematic diagram of fabrication of PPy-MWNTs-MEA. (b) SEM image of the cross-section of the PPy-MWNTs-MEA. White arrows indicate PPy-MWNTs grown on Pt electrode. The inset shows magnified cross-section image of the PPy-MWNTs grown on Pt electrode. Optical microscope (OM) images of the (c) PPy-MWNTs-MEA and (d) TiN-MEA.

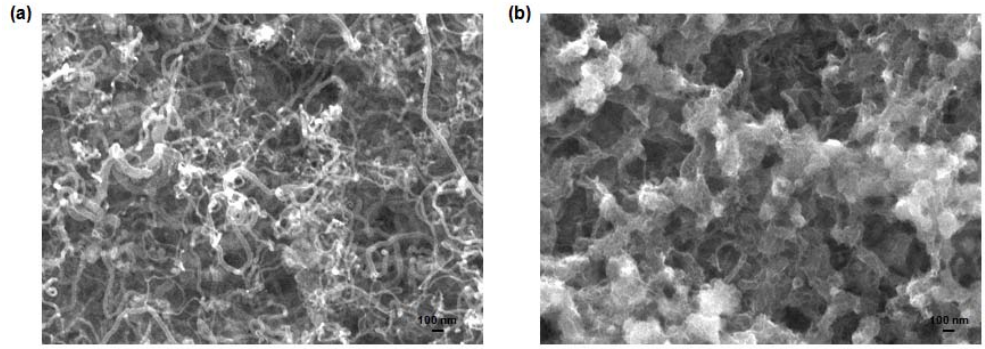

Figure 61. SEM images of before (a) and after (b) electrodeposited pyrrole on MWNTs.

4.3.2. *Ex vivo* contact impedance

An atherosclerotic plaque tissue was obtained from female apoE-/- mice with a high fat diet (ApoE-/- HFD) during 4 weeks. Dissected aorta ex vivo tissue (Figure 62) then stained with Oil Red O (ORO) to visualize lipid region. I have confirmed that the lipids contents were high in arch investigated by in vivo imaging system (IVIS) as well as ORO staining. This aorta arch was mounted on the two types of MEA; PPy-MWNTs-MEA and TiN-MEA and measured contact impedance under an ac voltage of 10 mV at a frequency of 100 kHz using LCR meter (Figure 63). Then, the contact impedance images were plotted on a 120 color scale with blue color denoting the lowest impedance (Figure 64a). I found that the use of PPy-MWNTs-MEA decreased the contact impedance by a factor of ~6 as compared to TiN-MEA as shown in Figure 64b. The reduction of contact

impedance is due to the high conductivity, high surface area, and increased mechanical stability of PPy-MWNTs-MEA. From this result, I anticipate that it is possible to visualize of lipid region in arch more apparently using PPy-MWNTs-MEA compared to TiN-MEA.

Figure 62. Photograph of the atherosclerotic plaque tissue dissected from the apoE$^{-/-}$ HFD mouse. The atherosclerotic plaque tissue was fixed by formaldehyde before ORO staining.

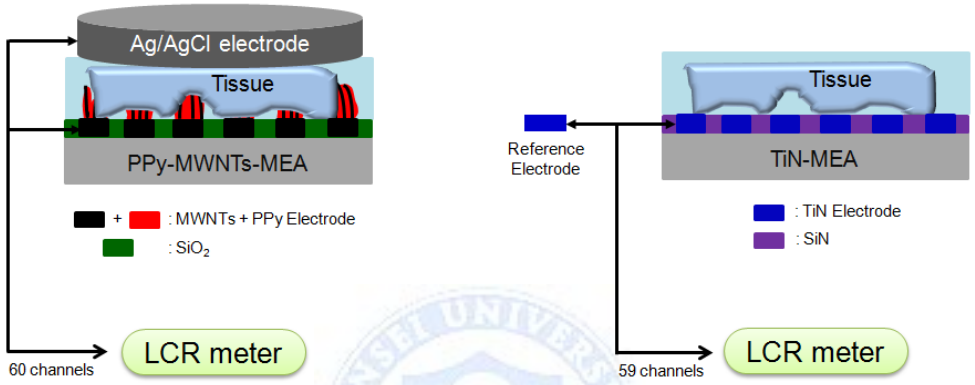

Figure 63. Schematic of the measurement system. The 60 electrodes of the PPy-MWNTs-MEA (or 59 electrodes of the TiN-MEA) were connected to the LCR meter. In PPy-MWNTs-MEA, an Ag/AgCl electrode was used as reference electrode.

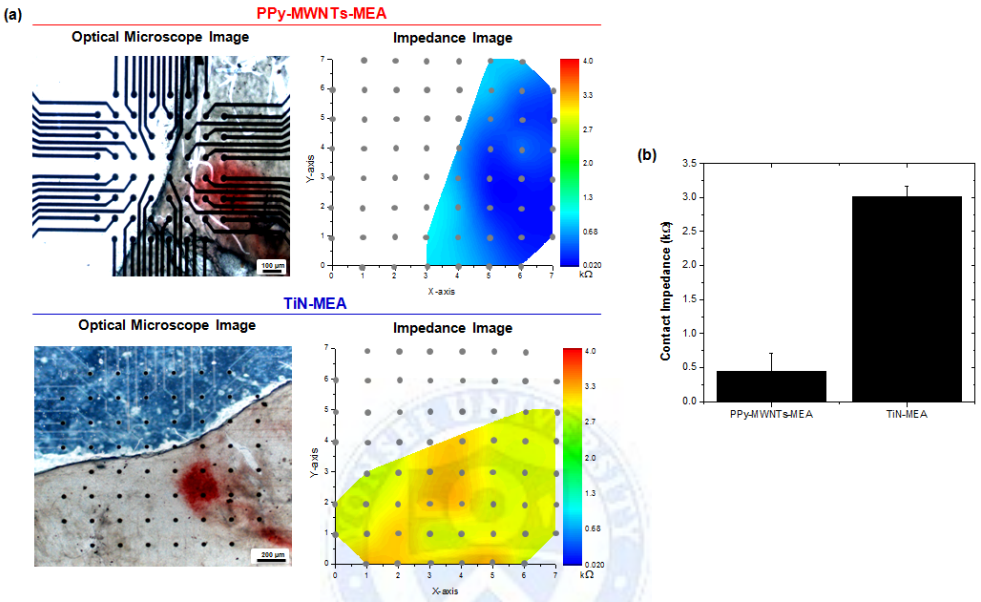

Figure 64. (a) The *ex vivo* contact impedance between electrodes (PPy-MWNTs-MEA or TiN-MEA) and atherosclerotic plaque tissue measured at 100 kHz. (b) The average *ex-vivo* contact impedance measured at 100 kHz for the two types of electrodes; PPy-MWNTs-MEA and TiN-MEA (n = 20 electrodes).

4.3.3. Discrimination of lipid region in atherosclerotic plaque tissue

Next, I investigated whether capacitance imaging technique can be used to discriminate lipid region from lipid-free region. For this, ORO stained arch was mounted on the two types of MEA as previously mentioned above. As I mentioned in introduction, the lipid region in arch obtained from $ApoE^{-/-}$ HFD has different dielectric constant (ε) compared with lipid-free region (Figure 59). Therefore, discrimination between lipid region and lipid-free region could be enabled by capacitance imaging technique.

The capacitance measurements at 10 kHz were plotted on a 120 color scale with red color denoting the highest capacitance. Comparison with the ORO-stained area in optical microscope (OM) images revealed that the red region with higher capacitance values which is measured by PPy-MWNTs-MEA corresponded to the lipid region. In TiN-MEA, however, the red color region indicating higher capacitance values was not seen at all, which means that TiN-MEA could not discriminate lipid region (Figure 65).

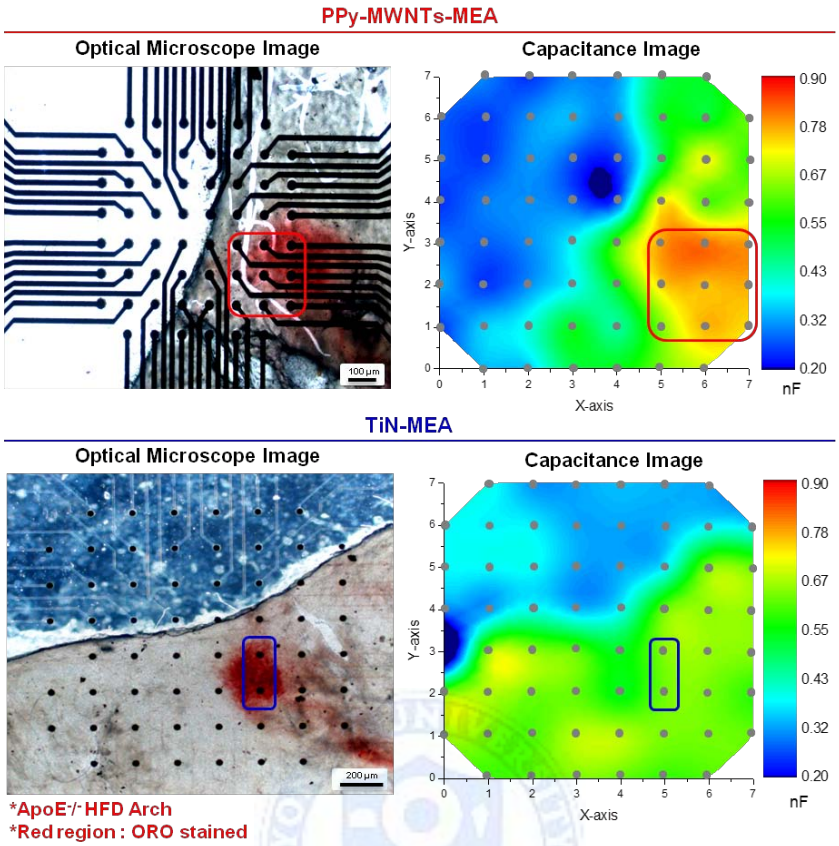

Figure 65. Optical microscope (OM) and capacitance images of the ORO-stained atherosclerotic plaque tissue. The ORO-stained atherosclerotic plaque tissue (red area in OM image, square box) was located on the PPy-MWNTs-MEA or TiN-MEA. For the capacitance imaging, an input AC voltage of 10 mV and frequency at 10 kHz were applied to the atherosclerotic plaque tissue. The color range was set between 0.20 and 0.90 nF with the red color denoting the highest capacitance and the gray circle denoting the electrode. The red region in the capacitance images measured by PPy-MWNTs-MEA corresponds to the ORO-stained area in OM images.

The frequency dependence of the capacitance and phase measured using PPy-MWNTs-MEA is shown in Figure 66 for the lipid region or lipid-free region in Figure 65. The lipid region represents an increase in capacitance over the entire frequency range (10 ~ 100 kHz), accompanied by a decrease in phase at the below 60 kHz, indicating lipid region has more capacitive property than lipid-free region. The trend of phase is comparable to previously studies reported by other groups [101]. These results indicated that PPy-MWNTs-MEA yields more apparent capacitance imaging of lipid region in arch than TiN-MEA, which is ascribe to improved contacts between the PPy-MWNTs and the arch.

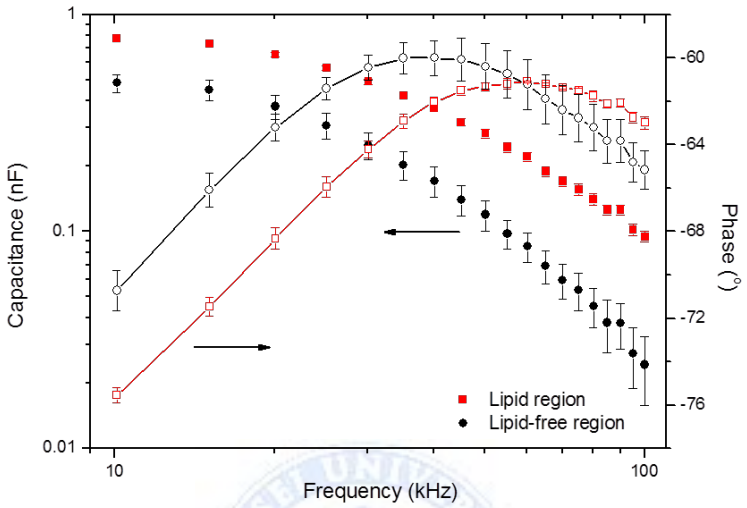

Figure 66. Frequency dependence of the capacitance (left Y-axis) and phase (right Y-axis) measured at lipid region (ORO-stained) or lipid-free region using the PPy-MWNTs-MEA. At the lipid region, the capacitance increased over the entire frequency range from 10 to 100 kHz compared to the lipid-free region, accompanied by a decrease in phase at a frequency below 60 kHz, indicating a more capacitive property than the lipid-free region (filled symbols : capacitance, opened symbols : phase, n = 3).

To investigate whether the lipid region of arch can be detected by flexible MEA, I also fabricated SWNTs-based flexible MEA (F-MEA). The SWNTs with percolating structures can provide a large effective surface area and mechanical flexible, enabling enhanced interfacing with atherosclerotic plaque tissue. The fabricated F-MEA has flexibility (Figure 67a) and percolating structures (Figure 67b). Capacitance imaging was performed by in two cases, a flat MEA (r = 0 cm) and a curved MEA (r = 1.5 cm), as shown in Figure 68a. Then, the ORO-stained arch was placed on F-MEA (Figure 67c). The capacitance measurements at 500 Hz were plotted on a 120 color scale with red color denoting the highest capacitance under the two conditions (r = 0 cm and r = 1.5 cm). In F-MEA, the capacitance values were lowered than PPy-MWNTs-MEA due to the semiconducting SWNTs of unsorted SWNTs (2/3 semiconducting, 1/3 metallic). Nevertheless, the lipid region could be detected by F-MEA even though the ability of distinguishing lipid region was slightly decreased in curved MEA (r = 1.5 cm).

The frequency dependence of the capacitance and phase measured using curved MEA (r = 1.5 cm) shows similar results as mentioned above (i.e. lipid region has more capacitive property than lipid-free region) (Figure 68b). Therefore, I could demonstrate the feasibility of F-MEA for identification of lipid in atherosclerotic plaque tissue. Further study of optimized conditions in F-MEA is needed.

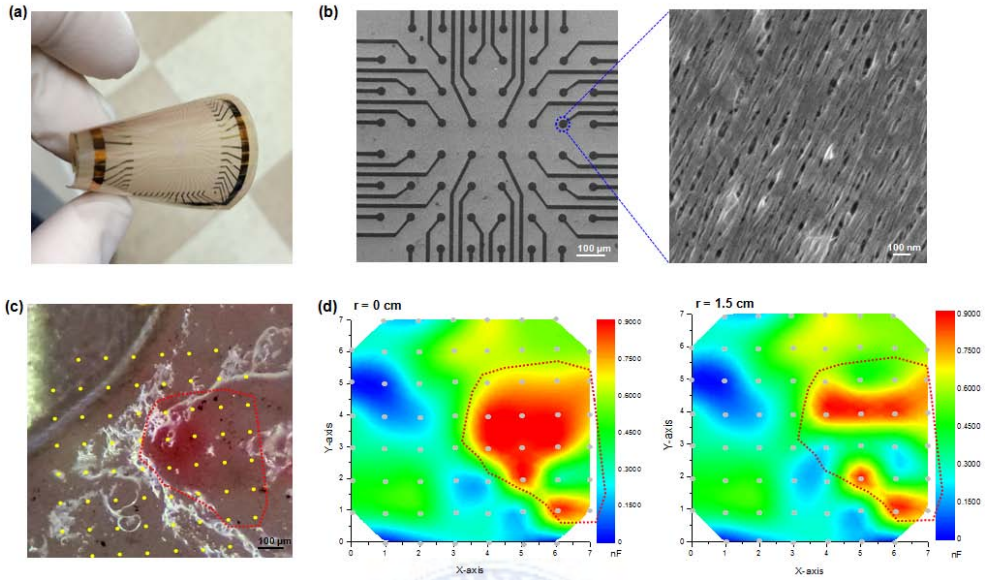

Figure 67. (a) The photograph of SWNTs-based electrodes on flexible substrate (F-MEA). (b) SEM image of SWNTs electrodes. Enlarged SWNTs electrode image was also indicated (blue dot circle). (c) The OM image of ORO-stained atherosclerotic plaque tissue (red area in OM image, red dot line) which was mounted on F-MEA. (d) Capacitance imaging of the lipid in atherosclerotic plaque tissue was obtained using F-MEA (r = 0 cm or r = 1.5 cm) under an input AC voltage of 10 mV and frequency at 500 Hz. The color range was set between 0 and 0.90 nF with the red color denoting the highest capacitance and the gray circle denoting the electrode.

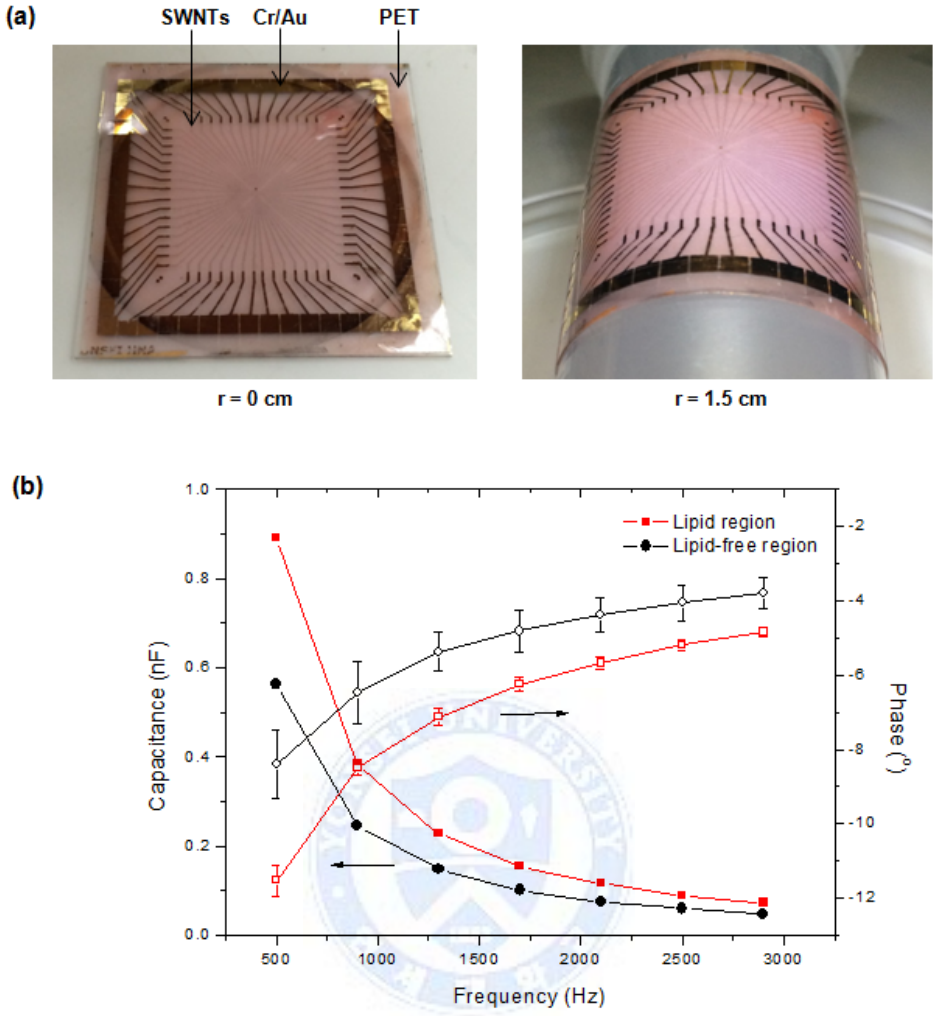

Figure 68. (a) The photograph of F-MEA (r = 0 cm or r = 1.5 cm), (b) Frequency dependence of the capacitance (left Y-axis) and phase (right Y-axis) measured at lipid region (ORO-stained) or lipid-free region using the F-MEA (r = 1.5 cm). At the lipid region, the capacitance increased over the entire frequency range from 500 to 2900 Hz compared to the lipid-free region, accompanied by a decrease in phase at a frequency, demonstrating a more capacitive property than the lipid-free region (filled symbols : capacitance, opened symbols : phase, n = 3).

4.4. Summary

I have developed a capacitance imaging technique using PPy-MWNTs-MEA or F-MEA. The lipid in atherosclerotic plaque tissue, which is derived from an apolipoprotein-E receptor-deficient ($apoE^{-/-}$) mouse, exhibit higher capacitance than the lipid-free region, allowing the capacitance imaging of lipid region in atherosclerosis. Compared to TiN-MEA, PPy-MWNTs-MEA yields more distinct and high resolution capacitance imaging of lipid region in atherosclerotic plaque tissue, which is ascribe to improved contacts between the PPy-MWNTs and the atherosclerotic plaque tissue. I also demonstrate that flexible electrodes can detect lipid region under curved condition, which is applicable to stent-based atherosclerosis sensing in clinic.

References

1. Sanvicens, N.; Marco, M. P., Multifunctional nanoparticles - properties and prospects for their use in human medicine. *Trends Biotechnol* **2008,** *26* (8), 425-433.

2. Xia, Y. N.; Halas, N. J., Shape-controlled synthesis and surface plasmonic properties of metallic nanostructures. *Mrs Bull* **2005,** *30* (5), 338-344.

3. Weissleder, R., A clearer vision for in vivo imaging. *Nat Biotechnol* **2001,** *19* (4), 316-317.

4. Yasun, E.; Kang, H. Z.; Erdal, H.; Cansiz, S.; Ocsoy, I.; Huang, Y. F.; Tan, W. H., Cancer cell sensing and therapy using affinity tag-conjugated gold nanorods. *Interface Focus* **2013,** *3* (3), 20130006.

5. Qian, X. M.; Peng, X. H.; Ansari, D. O.; Yin-Goen, Q.; Chen, G. Z.; Shin, D. M.; Yang, L.; Young, A. N.; Wang, M. D.; Nie, S. M., In vivo tumor targeting and spectroscopic detection with surface-enhanced Raman nanoparticle tags. *Nat Biotechnol* **2008,** *26* (1), 83-90.

6. Gobin, A. M.; Lee, M. H.; Halas, N. J.; James, W. D.; Drezek, R. A.; West, J. L., Near-infrared resonant nanoshells for combined optical imaging and photothermal cancer therapy. *Nano Lett* **2007,** *7* (7), 1929-1934.

7. Krishnan, K. M.; Pakhomov, A. B.; Bao, Y.; Blomqvist, P.; Chun, Y.; Gonzales, M.; Griffin, K.; Ji, X.; Roberts, B. K., Nanomagnetism and spin electronics: materials, microstructure and novel properties. *J Mater Sci* **2006,** *41* (3), 793-815.

8. Clement, O.; Siauve, N.; Cuenod, C. A.; Frija, G., Liver imaging with ferumoxides (Feridex): fundamentals, controversies, and practical

aspects. *Top Magn Reson Imaging* **1998,** *9* (3), 167-82.

9. Lee, J. H.; Jang, J. T.; Choi, J. S.; Moon, S. H.; Noh, S. H.; Kim, J. W.; Kim, J. G.; Kim, I. S.; Park, K. I.; Cheon, J., Exchange-coupled magnetic nanoparticles for efficient heat induction. *Nat Nanotechnol* **2011,** *6* (7), 418-422.

10. Namiki, Y.; Namiki, T.; Yoshida, H.; Ishii, Y.; Tsubota, A.; Koido, S.; Nariai, K.; Mitsunaga, M.; Yanagisawa, S.; Kashiwagi, H.; Mabashi, Y.; Yumoto, Y.; Hoshina, S.; Fujise, K.; Tada, N., A novel magnetic crystal-lipid nanostructure for magnetically guided in vivo gene delivery. *Nat Nanotechnol* **2009,** *4* (9), 598-606.

11. Alivisatos, A. P.; Gu, W. W.; Larabell, C., Quantum dots as cellular probes. *Annual Review of Biomedical Engineering* **2005,** *7*, 55-76.

12. Hong, G. S.; Robinson, J. T.; Zhang, Y. J.; Diao, S.; Antaris, A. L.; Wang, Q. B.; Dai, H. J., In Vivo Fluorescence Imaging with Ag2S Quantum Dots in the Second Near-Infrared Region. *Angew Chem Int Edit* **2012,** *51* (39), 9818-9821.

13. Wang, F.; Han, Y.; Lim, C. S.; Lu, Y. H.; Wang, J.; Xu, J.; Chen, H. Y.; Zhang, C.; Hong, M. H.; Liu, X. G., Simultaneous phase and size control of upconversion nanocrystals through lanthanide doping. *Nature* **2010,** *463* (7284), 1061-1065.

14. Auzel, F., Upconversion and anti-stokes processes with f and d ions in solids. *Chem Rev* **2004,** *104* (1), 139-173.

15. Wang, F.; Liu, X. G., Upconversion multicolor fine-tuning: Visible to near-infrared emission from lanthanide-doped NaYF4 nanoparticles. *J Am Chem Soc* **2008,** *130* (17), 5642-5643.

16. Idris, N. M.; Gnanasammandhan, M. K.; Zhang, J.; Ho, P. C.; Mahendran, R.; Zhang, Y., In vivo photodynamic therapy using

upconversion nanoparticles as remote-controlled nanotransducers. *Nat Med* **2012,** *18* (10), 1580-1585.

17. Piao, Y.; Burns, A.; Kim, J.; Wiesner, U.; Hyeon, T., Designed Fabrication of Silica-Based Nanostructured Particle Systems for Nanomedicine Applications. *Adv Funct Mater* **2008,** *18* (23), 3745-3758.

18. Epple, M.; Ganesan, K.; Heumann, R.; Klesing, J.; Kovtun, A.; Neumann, S.; Sokolova, V., Application of calcium phosphate nanoparticles in biomedicine. *J Mater Chem* **2010,** *20* (1), 18-23.

19. Maggiorella, L.; Barouch, G.; Devaux, C.; Pottier, A.; Deutsch, E.; Bourhis, J.; Borghi, E.; Levy, L., Nanoscale radiotherapy with hafnium oxide nanoparticles. *Future Oncol* **2012,** *8* (9), 1167-1181.

20. Barth, B. M.; Sharma, R.; Altinoglu, E. I.; Morgan, T. T.; Shanmugavelandy, S. S.; Kaiser, J. M.; McGovern, C.; Matters, G. L.; Smith, J. P.; Kester, M.; Adair, J. H., Bioconjugation of Calcium Phosphosilicate Composite Nanoparticles for Selective Targeting of Human Breast and Pancreatic Cancers In Vivo. *Acs Nano* **2010,** *4* (3), 1279-1287.

21. Liong, M.; Lu, J.; Kovochich, M.; Xia, T.; Ruehm, S. G.; Nel, A. E.; Tamanoi, F.; Zink, J. I., Multifunctional inorganic nanoparticles for imaging, targeting, and drug delivery. *Acs Nano* **2008,** *2* (5), 889-896.

22. Larson, D. R.; Ow, H.; Vishwasrao, H. D.; Heikal, A. A.; Wiesner, U.; Webb, W. W., Silica nanoparticle architecture determines radiative properties of encapsulated fluorophores. *Chem Mater* **2008,** *20* (8), 2677-2684.

23. Liang, F.; Chen, B., A Review on Biomedical Applications of Single-Walled Carbon Nanotubes. *Curr Med Chem* **2010,** *17* (1), 10-24.

24. Soppimath, K. S.; Aminabhavi, T. M.; Kulkarni, A. R.; Rudzinski, W. E., Biodegradable polymeric nanoparticles as drug delivery devices. *J*

Control Release **2001,** *70* (1-2), 1-20.

25. Cheng, J.; Teply, B. A.; Sherifi, I.; Sung, J.; Luther, G.; Gu, F. X.; Levy-Nissenbaum, E.; Radovic-Moreno, A. F.; Langer, R.; Farokhzad, O. C., Formulation of functionalized PLGA-PEG nanoparticles for in vivo targeted drug delivery. *Biomaterials* **2007,** *28* (5), 869-876.

26. De Geest, B. G.; Sanders, N. N.; Sukhorukov, G. B.; Demeester, J.; De Smedt, S. C., Release mechanisms for polyelectrolyte capsules. *Chem Soc Rev* **2007,** *36* (4), 636-649.

27. Schmaljohann, D., Thermo- and pH-responsive polymers in drug delivery. *Adv Drug Deliver Rev* **2006,** *58* (15), 1655-1670.

28. Bao, G.; Mitragotri, S.; Tong, S., Multifunctional Nanoparticles for Drug Delivery and Molecular Imaging. *Annu Rev Biomed Eng* **2013,** *15*, 253-282.

29. Alivisatos, P., The use of nanocrystals in biological detection. *Nat Biotechnol* **2004,** *22* (1), 47-52.

30. Popovtzer, R.; Agrawal, A.; Kotov, N. A.; Popovtzer, A.; Balter, J.; Carey, T. E.; Kopelman, R., Targeted Gold Nanoparticles Enable Molecular CT Imaging of Cancer. *Nano Lett* **2008,** *8* (12), 4593-4596.

31. Huang, X. H.; El-Sayed, I. H.; Qian, W.; El-Sayed, M. A., Cancer cell imaging and photothermal therapy in the near-infrared region by using gold nanorods. *J Am Chem Soc* **2006,** *128* (6), 2115-2120.

32. Hirsch, L. R.; Stafford, R. J.; Bankson, J. A.; Sershen, S. R.; Rivera, B.; Price, R. E.; Hazle, J. D.; Halas, N. J.; West, J. L., Nanoshell-mediated near-infrared thermal therapy of tumors under magnetic resonance guidance. *P Natl Acad Sci USA* **2003,** *100* (23), 13549-13554.

33. de Dios, A. S.; Diaz-Garcia, M. E., Multifunctional nanoparticles: Analytical prospects. *Anal Chim Acta* **2010,** *666* (1-2), 1-22.

34. Qu, L. H.; Peng, Z. A.; Peng, X. G., Alternative routes toward high quality CdSe nanocrystals. *Nano Lett* **2001,** *1* (6), 333-337.
35. Sun, S. H.; Zeng, H.; Robinson, D. B.; Raoux, S.; Rice, P. M.; Wang, S. X.; Li, G. X., Monodisperse MFe2O4 (M = Fe, Co, Mn) nanoparticles. *J Am Chem Soc* **2004,** *126* (1), 273-279.
36. Park, J.; An, K. J.; Hwang, Y. S.; Park, J. G.; Noh, H. J.; Kim, J. Y.; Park, J. H.; Hwang, N. M.; Hyeon, T., Ultra-large-scale syntheses of monodisperse nanocrystals. *Nat Mater* **2004,** *3* (12), 891-895.
37. Kircher, M. F.; de la Zerda, A.; Jokerst, J. V.; Zavaleta, C. L.; Kempen, P. J.; Mittra, E.; Pitter, K.; Huang, R. M.; Campos, C.; Habte, F.; Sinclair, R.; Brennan, C. W.; Mellinghoff, I. K.; Holland, E. C.; Gambhir, S. S., A brain tumor molecular imaging strategy using a new triple-modality MRI-photoacoustic-Raman nanoparticle. *Nat Med* **2012,** *18* (5), 829-834.
38. Medarova, Z.; Pham, W.; Farrar, C.; Petkova, V.; Moore, A., In vivo imaging of siRNA delivery and silencing in tumors. *Nat Med* **2007,** *13* (3), 372-377.
39. Yellen, B. B.; Forbes, Z. G.; Halverson, D. S.; Fridman, G.; Barbee, K. A.; Chorny, M.; Levy, R.; Friedman, G., Targeted drug delivery to magnetic implants for therapeutic applications. *J Magn Magn Mater* **2005,** *293* (1), 647-654.
40. Shapiro, B., Towards dynamic control of magnetic fields to focus magnetic carriers to targets deep inside the body. *J Magn Magn Mater* **2009,** *321* (10), 1594-1599.
41. Widder, K. J.; Senyel, A. E.; Scarpelli, G. D., Magnetic microspheres: a model system of site specific drug delivery in vivo. *Proc Soc Exp Biol Med* **1978,** *158* (2), 141-6.
42. Widder, K. J.; Morris, R. M.; Poore, G. A.; Howard, D. P.; Senyei,

A. E., Selective targeting of magnetic albumin microspheres containing low-dose doxorubicin: total remission in Yoshida sarcoma-bearing rats. *Eur J Cancer Clin Oncol* **1983,** *19* (1), 135-9.

43. Nobuto, H.; Sugita, T.; Kubo, T.; Shimose, S.; Yasunaga, Y.; Murakami, T.; Ochi, M., Evaluation of systemic chemotherapy with magnetic liposomal doxorubicin and a dipole external electromagnet. *Int J Cancer* **2004,** *109* (4), 627-635.

44. Chorny, M.; Fishbein, I.; Yellen, B. B.; Alferiev, I. S.; Bakay, M.; Ganta, S.; Adamo, R.; Amiji, M.; Friedman, G.; Levy, R. J., Targeting stents with local delivery of paclitaxel-loaded magnetic nanoparticles using uniform fields. *P Natl Acad Sci USA* **2010,** *107* (18), 8346-8351.

45. Hofmann, A.; Wenzel, D.; Becher, U. M.; Freitag, D. F.; Klein, A. M.; Eberbeck, D.; Schulte, M.; Zimmermann, K.; Bergemann, C.; Gleich, B.; Roell, W.; Weyh, T.; Trahms, L.; Nickenig, G.; Fleischmann, B. K.; Pfeifer, A., Combined targeting of lentiviral vectors and positioning of transduced cells by magnetic nanoparticles. *P Natl Acad Sci USA* **2009,** *106* (1), 44-49.

46. Kong, G.; Braun, R. D.; Dewhirst, M. W., Characterization of the effect of hyperthermia on nanoparticle extravasation from tumor vasculature. *Cancer Res* **2001,** *61* (7), 3027-3032.

47. Hu, S. H.; Chen, S. Y.; Liu, D. M.; Hsiao, C. S., Core/single-crystal-shell nanospheres for controlled drug release via a magnetically triggered rupturing mechanism. *Adv Mater* **2008,** *20* (14), 2690-2695.

48. Thomas, C. R.; Ferris, D. P.; Lee, J. H.; Choi, E.; Cho, M. H.; Kim, E. S.; Stoddart, J. F.; Shin, J. S.; Cheon, J.; Zink, J. I., Noninvasive Remote-Controlled Release of Drug Molecules in Vitro Using Magnetic Actuation of Mechanized Nanoparticles. *J Am Chem Soc* **2010,** *132* (31), 10623-10625.

49. Derfus, A. M.; von Maltzahn, G.; Harris, T. J.; Duza, T.; Vecchio, K.

S.; Ruoslahti, E.; Bhatia, S. N., Remotely triggered release from magnetic nanoparticles. *Adv Mater* **2007,** *19* (22), 3932-3936.

50. Lu, W.; Zhang, G.; Zhang, R.; Flores, L. G., 2nd; Huang, Q.; Gelovani, J. G.; Li, C., Tumor site-specific silencing of NF-kappaB p65 by targeted hollow gold nanosphere-mediated photothermal transfection. *Cancer Res* **2010,** *70* (8), 3177-88.

51. Eustis, S.; El-Sayed, M. A., Why gold nanoparticles are more precious than pretty gold: Noble metal surface plasmon resonance and its enhancement of the radiative and nonradiative properties of nanocrystals of different shapes. *Chem Soc Rev* **2006,** *35* (3), 209-217.

52. Zhang, Z. J.; Wang, J.; Chen, C. H., Near-Infrared Light-Mediated Nanoplatforms for Cancer Thermo-Chemotherapy and Optical Imaging. *Adv Mater* **2013,** *25* (28), 3869-3880.

53. Park, H.; Yang, J.; Lee, J.; Haam, S.; Choi, I. H.; Yoo, K. H., Multifunctional Nanoparticles for Combined Doxorubicin and Photothermal Treatments. *Acs Nano* **2009,** *3* (10), 2919-2926.

54. Lee, S. M.; Park, H.; Yoo, K. H., Synergistic Cancer Therapeutic Effects of Locally Delivered Drug and Heat Using Multifunctional Nanoparticles. *Adv Mater* **2010,** *22* (36), 4049-4053.

55. Lee, S. M.; Park, H.; Choi, J. W.; Park, Y. N.; Yun, C. O.; Yoo, K. H., Multifunctional Nanoparticles for Targeted Chemophotothermal Treatment of Cancer Cells. *Angew Chem Int Edit* **2011,** *50* (33), 7581-7586.

56. Lee, S. M.; Kim, H. J.; Ha, Y. J.; Park, Y. N.; Lee, S. K.; Park, Y. B.; Yoo, K. H., Targeted Chemo-Photothermal Treatments of Rheumatoid Arthritis Using Gold Half-Shell Multifunctional Nanoparticles. *Acs Nano* **2013,** *7* (1), 50-57.

57. Lee, S. M.; Kim, H. J.; Kim, S. Y.; Kwon, M. K.; Kim, S.; Cho, A.;

Yun, M.; Shin, J. S.; Yoo, K. H., Drug-loaded gold plasmonic nanoparticles for treatment of multidrug resistance in cancer. *Biomaterials* **2014,** *35* (7), 2272-2282.

58. Kim, H. J.; Lee, S. M.; Park, K. H.; Mun, C. H.; Park, Y. B.; Yoo, K. H., Drug-loaded gold/iron/gold plasmonic nanoparticles for magnetic targeted chemo-photothermal treatment of rheumatoid arthritis. *Biomaterials* **2015,** *61*, 95-102.

59. Nikoobakht, B.; El-Sayed, M. A., Preparation and growth mechanism of gold nanorods (NRs) using seed-mediated growth method. *Chem Mater* **2003,** *15* (10), 1957-1962.

60. Barreto, J. A.; O'Malley, W.; Kubeil, M.; Graham, B.; Stephan, H.; Spiccia, L., Nanomaterials: Applications in Cancer Imaging and Therapy. *Adv Mater* **2011,** *23* (12), H18-H40.

61. Levick, J. R., Permeability of Rheumatoid and Normal Human Synovium to Specific Plasma-Proteins. *Arthritis Rheum* **1981,** *24* (12), 1550-1560.

62. Fojo, A.; Cornwell, M.; Cardarelli, C.; Clark, D. P.; Richert, N.; Shen, D. W.; Ueda, K.; Willingham, M.; Gottesman, M. M.; Pastan, I., Molecular-Biology of Drug-Resistance. *Breast Cancer Res Tr* **1987,** *9* (1), 5-16.

63. Gottesman, M. M.; Fojo, T.; Bates, S. E., Multidrug resistance in cancer: Role of ATP-dependent transporters. *Nat Rev Cancer* **2002,** *2* (1), 48-58.

64. Shi, Z.; Tiwari, A. K.; Patel, A. S.; Fu, L. W.; Chen, Z. S., Roles of Sildenafil in Enhancing Drug Sensitivity in Cancer. *Cancer Res* **2011,** *71* (11), 3735-3738.

65. Lowe, S. W.; Ruley, H. E.; Jacks, T.; Housman, D. E., P53-

Dependent Apoptosis Modulates the Cytotoxicity of Anticancer Agents. *Cell* **1993,** *74* (6), 957-967.

66. Chin, K. V.; Tanaka, S.; Darlington, G.; Pastan, I.; Gottesman, M. M., Heat-Shock and Arsenite Increase Expression of the Multidrug Resistance (Mdr1) Gene in Human Renal-Carcinoma Cells. *J Biol Chem* **1990,** *265* (1), 221-226.

67. Giacomini, K. M.; Huang, S. M.; Tweedie, D. J.; Benet, L. Z.; Brouwer, K. L. R.; Chu, X. Y.; Dahlin, A.; Evers, R.; Fischer, V.; Hillgren, K. M.; Hoffmaster, K. A.; Ishikawa, T.; Keppler, D.; Kim, R. B.; Lee, C. A.; Niemi, M.; Polli, J. W.; Sugiyama, Y.; Swaan, P. W.; Ware, J. A.; Wright, S. H.; Yee, S. W.; Zamek-Gliszczynski, M. J.; Zhang, L.; Transporter, I., Membrane transporters in drug development. *Nat Rev Drug Discov* **2010,** *9* (3), 215-236.

68. Hever-Szabo, A.; Pirity, M.; Szathmari, M.; Venetianer, A., P-glycoprotein is overexpressed and functional in severely heat-shocked hepatoma cells. *Anticancer Res* **1998,** *18* (4C), 3045-3048.

69. Ramachandra, M.; Ambudkar, S. V.; Chen, D.; Hrycyna, C. A.; Dey, S.; Gottesman, M. M.; Pastan, I., Human P-glycoprotein exhibits reduced affinity for substrates during a catalytic transition state. *Biochemistry-Us* **1998,** *37* (14), 5010-5019.

70. Hu, C. M. J.; Zhang, L. F., Nanoparticle-based combination therapy toward overcoming drug resistance in cancer. *Biochem Pharmacol* **2012,** *83* (8), 1104-1111.

71. Fletcher, J. I.; Haber, M.; Henderson, M. J.; Norris, M. D., ABC transporters in cancer: more than just drug efflux pumps. *Nat Rev Cancer* **2010,** *10* (2), 147-156.

72. Wartenberg, M.; Gronczynska, S.; Bekhite, M. M.; Saric, T.;

Niedermeier, W.; Hescheler, J.; Sauer, H., Regulation of the multidrug resistance transporter P-glycoprotein in multicellular prostate tumor spheroids by hyperthermia and reactive oxygen species. *Int J Cancer* **2005,** *113* (2), 229-240.

73. Garrigues, A.; Escargueil, A. E.; Orlowski, S., The multidrug transporter, P-glycoprotein, actively mediates cholesterol redistribution in the cell membrane. *P Natl Acad Sci USA* **2002,** *99* (16), 10347-10352.

74. Chang, C. S.; Huang, W. T.; Yang, S. S.; Yeh, H. Z.; Kao, C. H.; Chen, G. H., Effect of P-glycoprotein and multidrug resistance associated protein gene expression on Tc-99m MIBI imaging in hepatocellular carcinoma. *Nucl Med Biol* **2003,** *30* (2), 111-117.

75. Raptopoulou, A.; Sidiropoulos, P.; Katsouraki, M.; Boumpas, D. T., Anti-citrulline antibodies in the diagnosis and prognosis of rheumatoid arthritis: Evolving concepts. *Crit Rev Cl Lab Sci* **2007,** *44* (4), 339-363.

76. Firestein, G. S., Evolving concepts of rheumatoid arthritis. *Nature* **2003,** *423* (6937), 356-361.

77. Schubert, W., Rheumatoid-Arthritis - Evolving Concepts of Pathogenesis and Treatment. *Ann Intern Med* **1984,** *101* (6), 810-824.

78. Pincus, T.; Callahan, L. F.; Sale, W. G.; Brooks, A. L.; Payne, L. E.; Vaughn, W. K., Severe Functional Declines, Work Disability, and Increased Mortality in 75 Rheumatoid-Arthritis Patients Studied over 9 Years. *Arthritis Rheum* **1984,** *27* (8), 864-872.

79. Redlich, K.; Hayer, S.; Ricci, R.; David, J. P.; Tohidast-Akrad, M.; Kollias, G.; Steiner, G.; Smolen, J. S.; Wagner, E. F.; Schett, G., Osteoclasts are essential for TNF-alpha-mediated joint destruction. *J Clin Invest* **2002,** *110* (10), 1419-1427.

80. Kong, Y. Y.; Feige, U.; Sarosi, I.; Bolon, B.; Tafuri, A.; Morony, S.;

Capparelli, C.; Li, J.; Elliott, R.; McCabe, S.; Wong, T.; Campagnuolo, G.; Moran, E.; Bogoch, E. R.; Van, G.; Nguyen, L. T.; Ohashi, P. S.; Lacey, D. L.; Fish, E.; Boyle, W. J.; Penninger, J. M., Activated T cells regulate bone loss and joint destruction in adjuvant arthritis through osteoprotegerin ligand. *Nature* **1999,** *402* (6759), 304-309.

81. Ziolkowska, M.; Kurowska, M.; Radzikowska, A.; Luszczykiewicz, G.; Wiland, P.; Dziewczopolski, W.; Filipowicz-Sosnowska, A.; Pazdur, J.; Szechinski, J.; Kowalczewski, J.; Rell-Bakalarska, M.; Maslinski, W., High levels of osteoprotegerin and soluble receptor activator of nuclear factor kappa B ligand in serum of rheumatoid arthritis patients and their normalization after anti-tumor necrosis factor alpha treatment. *Arthritis Rheum* **2002,** *46* (7), 1744-1753.

82. Pettit, A. R.; Ji, H.; von Stechow, D.; Muller, R.; Goldring, S. R.; Choi, Y. W.; Benoist, C.; Gravallese, E. M., TRANCE/RANKL knockout mice are protected from bone erosion in a serum transfer model of arthritis. *Am J Pathol* **2001,** *159* (5), 1689-1699.

83. Schett, G.; Tohidast-Akrad, M.; Smolen, J. S.; Schmid, B. J.; Steiner, C. W.; Bitzan, P.; Zenz, P.; Redlich, K.; Xu, Q. B.; Steiner, G., Activation, differential localization, and regulation of the stress-activated protein kinases, extracellular signal-regulated kinase, c-Jun N-terminal kinase, and p38 mitogen-activated protein kinase, in synovial tissue and cells in rheumatoid arthritis. *Arthritis Rheum* **2000,** *43* (11), 2501-2512.

84. Badger, A. M.; Bradbeer, J. N.; Votta, B.; Lee, J. C.; Adams, J. L.; Griswold, D. E., Pharmacological profile of SB 203580, a selective inhibitor of cytokine suppressive binding protein/p38 kinase, in animal models of arthritis, bone resorption, endotoxin shock and immune function. *J Pharmacol Exp Ther* **1996,** *279* (3), 1453-1461.

85. Saag, K. G.; Teng, G. G.; Patkar, N. M.; Anuntiyo, J.; Finney, C.; Curtis, J. R.; Paulus, H. E.; Mudano, A.; Pisu, M.; Elkins-Melton, M.; Outman, R.; Allison, J. J.; Almazor, M. S.; Bridges, S. L.; Chatham, W. W.; Hochberg, M.; Maclean, C.; Mikuls, T.; Moreland, L. W.; O'Dell, J.; Turkiewicz, A. M.; Furst, D. E., American College of Rheumatology 2008 recommendations for the use of nonbiologic and biologic disease-modifying antirheumatic drugs in rheumatoid arthritis. *Arthrit Rheum-Arthr* **2008,** *59* (6), 762-784.

86. Schnabel, A.; Gross, W. L., Low-Dose Methotrexate in Rheumatic Diseases - Efficacy, Side-Effects, and Risk-Factors for Side-Effects. *Semin Arthritis Rheu* **1994,** *23* (5), 310-327.

87. van Ede, A. E.; Laan, R. F. J. M.; Blom, H. J.; De Abreu, R. A.; van de Putte, L. B. A., Methotrexate in rheumatoid arthritis: An update with focus on mechanisms involved in toxicity. *Semin Arthritis Rheu* **1998,** *27* (5), 277-292.

88. Yokota, K.; Ishibashi, T.; Hirano, M.; Yoshida, Y.; Kamikawa, T.; Adachi, D.; Akiba, H.; Takeishi, M.; Akiyama, Y.; Mimura, T., Simvastatin inhibits production of interleukin-6 and interleukin-8 and cell proliferation promoted bv tumor necrosis factor-alpha or induces apoptosis in fibroblast-like synoviocytes from patients with rheumatoid arthritis. *J Rheumatol* **2006,** *33* (3), 463-71.

89. Litinsky, I.; Golan, I.; Yaron, M.; Yaron, I.; Caspi, D.; Elkayam, O., Simvastatin Induces Apoptosis of Fibroblast-Like Synoviocytes *The Open Rheu J* **2009,** *3*, 35-40.

90. Brand, D. D.; Latham, K. A.; Rosloniec, E. F., Collagen-induced arthritis. *Nat Protoc* **2007,** *2* (5), 1269-1275.

91. Hynes, R. O., A reevaluation of integrins as regulators of

angiogenesis. *Nat Med* **2002,** *8* (9), 918-921.

92. Hong, Y.; Lee, E.; Choi, J.; Oh, S. J.; Haam, S.; Huh, Y. M.; Yoon, D. S.; Suh, J. S.; Yang, J., Gold Nanorod-Mediated Photothermal Modulation for Localized Ablation of Cancer Cells. *J Nanomater* **2012**, *2012*, 825060.

93. Ke, H. T.; Wang, J. R.; Tong, S.; Jin, Y. S.; Wang, S. M.; Qu, E. Z.; Bao, G.; Dai, Z. F., Gold Nanoshelled Liquid Perfluorocarbon Magnetic Nanocapsules: a Nanotheranostic Platform for Bimodal Ultrasound/Magnetic Resonance Imaging Guided Photothermal Tumor Ablation. *Theranostics* **2014,** *4* (1), 12-23.

94. Zolnik, B. S.; Leary, P. E.; Burgess, D. J., Elevated temperature accelerated release testing of PLGA microspheres. *J Control Release* **2006,** *112* (3), 293-300.

95. Camps, M.; Ruckle, T.; Ji, H.; Ardissone, V.; Rintelen, F.; Shaw, J.; Ferrandi, C.; Chabert, C.; Gillieron, C.; Francon, B.; Martin, T.; Gretener, D.; Perrin, D.; Leroy, D.; Vitte, P. A.; Hirsch, E.; Wymann, M. P.; Cirillo, R.; Schwarz, M. K.; Rommel, C., Blockade of PI3K gamma suppresses joint inflammation and damage in mouse models of rheumatoid arthritis. *Nat Med* **2005,** *11* (9), 936-943.

96. Lee, S. W.; Kim, J. H.; Park, Y. B.; Lee, S. K., Bortezomib attenuates murine collagen-induced arthritis. *Annals of the rheumatic diseases* **2009,** *68* (11), 1761-7.

97. Lusis, A. J., Atherosclerosis. *Nature* **2000,** *407* (6801), 233-241.

98. Rader, D. J.; Daugherty, A., Translating molecular discoveries into new therapies for atherosclerosis. *Nature* **2008,** *451* (7181), 904-913.

99. Xu, S. W.; Huang, Y.; Xie, Y.; Lan, T. A.; Le, K.; Chen, J. W.; Chen, S. R.; Gao, S.; Xu, X. Z.; Shen, X. Y.; Huang, H. Q.; Liu, P. Q., Evaluation

of foam cell formation in cultured macrophages: an improved method with Oil Red O staining and DiI-oxLDL uptake. *Cytotechnology* **2010,** *62* (5), 473-481.

100. Yu, F.; Dai, X. H.; Beebe, T.; Hsiai, T., Electrochemical impedance spectroscopy to characterize inflammatory atherosclerotic plaques. *Biosens Bioelectron* **2011,** *30* (1), 165-173.

101. Cao, H.; Yu, F.; Zhao, Y.; Scianmarello, N.; Lee, J.; Dai, W. D.; Jen, N.; Beebe, T.; Li, R. S.; Ebrahimi, R.; Chang, D. S.; Mody, F. V.; Pacella, J.; Tai, Y. C.; Hsiai, T., Stretchable electrochemical impedance sensors for intravascular detection of lipid-rich lesions in New Zealand White rabbits. *Biosens Bioelectron* **2014,** *54*, 610-616.

102. Lee, R.; Jung, I.; Park, M.; Ha, H.; Yoo, K. H., Real-time monitoring of adipocyte differentiation using a capacitance sensor array. *Lab Chip* **2013,** *13* (17), 3410-3416.

103. Keefer, E. W.; Botterman, B. R.; Romero, M. I.; Rossi, A. F.; Gross, G. W., Carbon nanotube coating improves neuronal recordings. *Nat Nanotechnol* **2008,** *3* (7), 434-439.

104. Lu, Y.; Li, T.; Zhao, X. Q.; Li, M.; Cao, Y. L.; Yang, H. X.; Duan, Y. W. Y., Electrodeposited polypyrrole/carbon nanotubes composite films electrodes for neural interfaces. *Biomaterials* **2010,** *31* (19), 5169-5181.

ABSTRACT in Korean

약물이 담지된 금 플라스모닉 나노입자를 이용한 다-약물 내성암과 류마티스 관절염 치료

약물이 담지된 polylactic-*co*-glycolic acid (PLGA) 고분자에 반구 형태의 금 박막 및 철 박막을 입혀, *in vitro* 및 *in vivo* 에서 다-약물 내성 암과 류마티스 관절염을 치료할 수 있는 금 플라스모닉 나노입자를 제작하였다. 약물이 담지된 금 플라스모닉 나노입자는 고유한 특징을 보이는데, 나노입자의 반쪽 부분에서는 약물이 방출되고, 나노입자의 나머지 반쪽 부분은 금 박막 또는 철 박막으로 구성되어 있어 근적외선 및 자기공명 영상에 사용될 수 있고, 근적외선 레이져를 조사 하였을 때,

금 박막에서 발생하는 열을 이용해 고분자 안에 담지되어 있는 약물의 방출을 증가시킬 수 있다. 또한, 금 박막은 표면 처리가 쉽기 때문에 다양한 항체 및 표적지향물질을 결합시킬 수 있다.

본 연구에서는 먼저 다-약물 내성 암을 치료하고자 했는데, 일반적으로 다-약물 내성 암은 P-glycoprotein 과 같은 배출 단백질 (efflux protein)이 과 발현 되어 있기 때문에 세포 안으로 들어온 약물을 빠르게 세포 밖으로 배출하게 된다. 따라서 다-약물 내성 암을 효과적으로 치료하기 위해서는 배출 단백질의 기능을 억제시키는 것이 가장 중요하다. 항암제인 독소루비신 (Doxorubicin, DOX)를 담지하고, 독소루비신에 내성이 있는 결장 종양세포 (DLD-1/DOX)와 선택적으로 반응하는 항체 (Human TRAIL R1/TNFRSF10A Antibody, Anti-DR4)가 금 박막에 결합되어 있는 나노입자의 광열 효과 (Photothermal Effect)를 이용해 다-약물 내성 암을 효과적으로 치료하였다.

현재까지 나노입자를 이용한 치료는 주로 암을 목표로 연구가 많이 진행되었는데, 만성 염증성 관절염인 류마티스 관절염에서도 약물이 담지된 금 플라스모닉 나노입자의 치료효과가 있는지 연구하였다. 류마티스 관절염 치료제인 메토트렉세이트 (Methotrexate, MTX)를 담지하고, 염증 표적지향물질인 arginine-glycine-aspartic acid (RGD) 펩타이드 (peptides)가 금 박막에 결합되어 있는 나노입자를 이용해 류마티스 관절염 역시 효과적으로 치료되는 것을 확인하였다. 또한, 금 박막 사이

에 철 박막을 입힌 후, 네오듐 (Nd) 자석을 이용하여 관절염 부위에 나노입자가 오래 머무르도록 함으로서, 좀더 효과적인 광열 및 화학적 치료효과 뿐 만 아니라, 자기공명영상 (MRI, Magnetic resonance image)을 얻을 수 있었다.

핵심어 : 약물이 담지된 금 플라스모닉 나노입자, 약물이 담지된 금/철/금 플라스모닉 나노입자, 화학적-광열 치료, 광열로 조절되는 약물 전달, 다-약물 내성암, 류마티스 관절염

Publication lists

12. **Hyung Joon Kim**, Sun-Mi Lee, Kyu-Hyung Park, Chin Hee Mun, Yong-Beom Park, and Kyung-Hwa Yoo, "Drug-loaded gold/iron/gold plasmonic nanoparticles for magnetic targeted chemo-photothermal treatment of rheumatoid arthritis", ***Biomaterials***, 61, 95-102 (2015).

11. Sun-Mi Lee[#], **Hyung Joon Kim**[#], Sook Young Kim, Min-Kyung Kwon, Sol Kim, Arthur Cho, Mijin Yun, Jeon-Soo Shin, and Kyung-Hwa Yoo, "Drug-loaded gold plasmonic nanoparticles for treatment of multidrug resistance in cancer", ***Biomaterials***, 35, 2272-2282 (2014). **([#]: equally contribution)**

10. Sam Jin Kim, Sung Wook Hyun, **Hyung Joon Kim**, and Chul Sung Kim, "Thermal Variation of MgZn Nanoferrites for Magnetic Hyperthermia", ***J. Korean Phys. Soc.***, 65, 553-556 (2014).

9. Sun-Mi Lee, **Hyung Joon Kim**, You-Jung Ha, Young Nyun Park, Soo-Kon Lee, Yong-Beom Park, and Kyung-Hwa Yoo, "Targeted Chemo-Photothermal Treatments of Rheumatoid Arthritis Using Gold Half-shell Multifunctional Nanoparticles", ***ACS Nano***, 7, 50-57 (2013).

8. Jeseung Oh, Gu Yoo, Young Wook Chang, **Hyung Joon Kim**, Joachim Jose, Eosu Kim, Jae-Chul Pyun, and Kyung-Hwa Yoo, "A carbon nanotube metal semiconductor field effect transistor-based biosensor for detection of amyloid-beta in human serum", ***Biosens Bioelectron***, 50, 345-350 (2013).

7. Minseon Kim, **Hyung Joon Kim**, Eunjoo Hahn, Kyung-Hwa Yoo, and Chul Sung Kim, "Effect Hyperthermia in $CoFe_2O_4$@$MnFe_2O_4$ Nanoparticles Studied by using Field-induced Mössbauer Spectroscopy", ***J. Korean Phys. Soc.***, 63, 2175-2178 (2013).

6. **Hyung Joon Kim**, Sungsic Hwang, Jeseung Oh, Young Wook Chang, Eun-Kyung Lim, Seungjoo Haam, Chul Sung Kim, and Kyung-Hwa Yoo, "Magnetic nanoparticle-based separation of metallic and semiconducting carbon nanotubes", ***Nanotechnology***, 22, 045703 (2011).

5. **Hyung Joon Kim**, Eun-Kyung Lim, Seungjoo Haam, and Kyung-Hwa Yoo, "Large Scale Separation of Metallic and Semiconducting Single-Walled Carbon Nanotubes using Magnetic Nanoparticles; Application to Carbon Nanotubes based Biosensor", ***Eur. Cell. Mater.***, 20 (Suppl. 3), 295 (2010).

4. Jeseung Oh, Young Wook Chang, **Hyung Joon Kim**, Seunghwan Yoo, Dong Jun Kim, Seongil Im, Young June Park, Donghyun Kim, and Kyung-Hwa Yoo, "Carbon Nanotube-Based Dual-Mode Biosensor for Electrical and Surface Plasmon Resonance Measurements", ***Nano Lett.***, 10, 2755-2760 (2010).

3. Woochul Kim, Chan Hyuk Rhee, **Hyung Joon Kim**, Seung Je Moon, and Chul Sung Kim, "Strong crystalline field at the Fe site and spin rotation in olivine $LiNi_{0.99}{}^{57}Fe_{0.01}PO_4$ material by Mössbauer spectroscopy", ***Appl. Phys. Lett.***, 96, 242505 (2010).

2. Woochul Kim, Il Jin Park, **Hyung Joon Kim**, Wooyoung Lee, Sam Jin Kim, and Chul Sung Kim, "Room-Temperature Ferromagnetic Property in MnTe Semiconductor Thin Film Grown by Molecular Beam Epitaxy", ***IEEE Trans. on Mag.,*** 45, 2424-2427 (2009).

1. Sung Wook Hyun, **Hyung Joon Kim**, Chu Sik Park, Kyoung-Soo Kang, and Chul Sung Kim, "Synthesis and Size Dependent Properties of Magnesium Ferrites", ***IEEE Trans. on Mag.,*** 45, 2551-2553 (2009).